UNIVERSIDAD NACIONAL AUTÓNOMA DE MÉXICO

MAESTRÍA EN CIENCIAS (FÍSICA)

NO CLASICALIDAD EN PARES DE FOTONES GENERADOS EN ÁTOMOS FRÍOS

T E S I S

que para optar por el grado de

MAESTRO EN CIENCIAS (FÍSICA)

PRESENTA:
IRVIN FERMÍN ÁNGELES AGUILLÓN

Tutor Principal:

DR. DANIEL SAHAGÚN SÁNCHEZ

INSTITUTO DE FÍSICA

México, CDMX Marzo de 2021

ACKNOWLEDGMENTS

To my beloved family who always supports me and has been always there for me, especially in difficult and treacherous times. To my Mother Lilia and my father Fermín, both of which have always been an example for me of hard work, dedication, and love. I can't thank them enough, but I hope this work makes them proud of me. To my sister Avril, who listens to every piece of advice that I give her. Your road has just started, enjoy it. To all my other beloved family members. I could write a book twice as long as this work only by naming and thanking each and every one of you. Thank you for everything.

To my great love and life partner, Susana. Thank you for all your support, for all your love, and for the happiness that we've shared together. Thank you for arriving at my life and for letting me part of yours. We will always be the invincible team 23, together (*Sound of dog).

To my great friends, boardgame buddies, and partners-in-crime, Fernando and Carlos, written by appearance order. You had been a great support for me all these years and I'm glad I still keep two good friends like you.

To my supervisor, Dr. Daniel Sahagún. I've always will thank you for your support in difficult times and I sincerely appreciate your guidance and help through all this work. I want to thank also to Dr. Rocío Jáuregui and Dr. Ricardo Gutiérrez Jáuregui for the

useful and enlightening meetings that help this work. Also, I greatly thank the always illustrative and constructive meetings with Dr. Isaac Pérez and Dr. Alessandro Cerè.

To my lab partners Nieves, Luis, Adrián, Diego, Jorge which whom I have shared countless hours. This work literally could never be possible without the work and contributions each and every one of you had made in the lab.

Finally, I want to thank the National Council for Science and Technology (CONACyT) for the funding of this work through the National Laboratories Program grants 280181, 293471, and 299057. Also I want to thank the Basic Science SEP-CONACyT program, grant no.285387, DGAPA - UNAM PAPIIT grant no. IN108018 and IN106821 and PIIF, IF-UNAM for their funding support.

Abstract

In this thesis, I study the temporal coherence of photon pairs generated by a process of four-wave mixing in a cold rubidium atomic cloud. The second-order cross-correlation and autocorrelation functions of the system were measured. Both were used to measure the Cauchy coefficient R resulting in a factor of 10^5, indicating a strong violation of the Cauchy-Schwarz inequality and then showing non-classicality in the temporal coherence of the generated photon pairs. Using a model based on a solution of the Schrödinger equation for a consecutive decay, the experimental data were fitted, obtaining measurements of the coherence time τ_0, the bandwidth of the idler photon Γ and the spectral brightness $\mathcal{B}$ of the source.

Resumen

En esta tesis estudio la coherencia temporal de los pares de fotones generados por un proceso de mezclado de cuatro ondas en una nube de átomos fríos de Rubidio. En él se midieron la correlación cruzada de segundo orden y la función de autocorrelación del sistema. Ambas fueron usadas para medir en coeficiente de Cauchy R resultando en un factor de 10^5, indicando una fuerte violación de la desigualdad de Cauchy-Schwarz, lo cual implica la no clasicalidad en la coherencia temporal de los fotones generados. Usando un modelo basado en una solución de la ecuación de Schrödinger para un decaimiento consecutivo, se ajustaron los datos experimentales, midiendo el tiempo de coherencia τ_0, el ancho de banda Γ del fotón acompañante y el brillo espectral $\mathcal{B}$ de la fuente.

Contents

Page

List of Figures

Figure **Page**

Chapter 1

Introduction

The emergence of quantum mechanics more than 100 years ago was a revolutionary moment for science and for the way we see and describe the world. The early quantization of electromagnetic energy was proposed by Planck in 1901 [1] to explain the black-body radiation. Later, Einstein propose the photon in its description of the photoelectric effect [2]. From the very beginning, it was not clear how to transform from classical to quantum theories. One of the first steps towards a methodology to achieve that transition was done by Dirac in 1925 [3]. He created what is now known as canonical quantization. Since these discoveries, statistical tests have been developed to differentiate between quantum and classical light.

One of the most important steps towards the modern understanding of light was the experiment of Hanbury-Brown and Twiss in 1956 [4], which analyzed the coincidences between two detectors. The intensity correlations of light coming from a star helped to determine its size. This experiment, along with the development of the first lasers in the 60s [5], motivated the concept of second-order coherence [6]. This was later written in terms of quantum operators [7] and integrated into the modern analysis of photon sources that we have nowadays. Along with these studies, Roy Glauber developed a theory of photodetection [8] which has been the base of the majority of quantum optics experiments.

The first experimental demostrations of single photon sources were performed in the early 70s. One of these was the spontaneous parametric down-conversion (SPDC) in non-linear crystals [9]. Another source developed at that time was the photon pair generation by four-wave mixing (FWM) in atomic media [10]. A decay photon pair generated in a calcium source using FWM was used to demonstrate for the first time a violation of the Bell inequalities [11]. Since their appearence, the generation of single photons has been an useful tool for quantum optics. With them, we can perform a wide variety of experiments: from fundamental tests of quantum principles to applications in quantum information [12].

1.1 Complete quantum systems

A complete quantum system is defined as the fundamental block of a quantum network. It consists of a node, where the information is processed, stored or replicated and messengers that communicate nodes between them. Figure 1.1 presents a scheme of a quantum repeater: a simple quantum network that compensates the losses in a transmission line between two points.

One of the possible experimental realizations of a complete quantum systems is an atomic ensemble taking the roll of a node and photons acting as messengers of information [13]. In this case the communication of both elements is given by the interaction between light and atoms. The photons need to have the suitable frequency and bandwidth to be able to interact with an atomic ensemble, and also need to be enough for an efficient process. Both SPDC and FWM sources can provide us with photons with the correct frequency and bandwidth to interact with atoms. Both kinds of sources can even generate photons in the telecom band (1260-1625 nm), which can make possible to send these photons through the optical fibers currently used [14, 15].

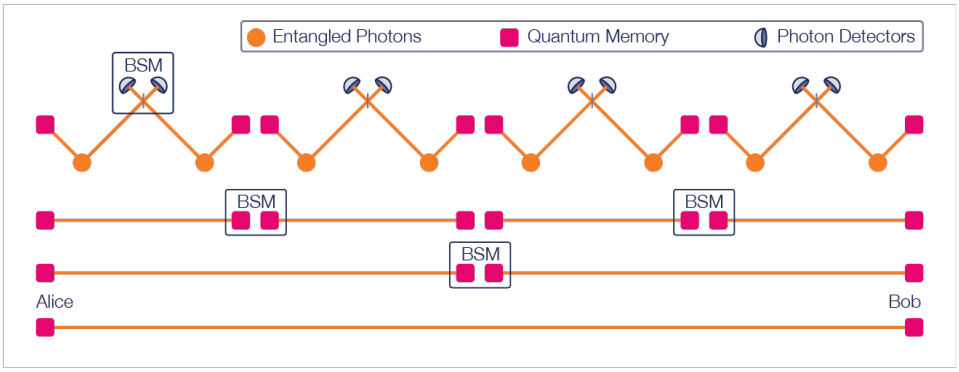

Figure 1.1: Scheme of a quantum repeater. The distance between two observers Alice and Bob is divided into smaller blocks. In those blocks there are two sources of entangled photons, where one of each one of them is sent into two quantum memories. The others are sent into a Bell-state measurement (BSM). When the BSM is performed it is found that the photons in the memories will have correlations too. By performing consecutively BSM between neighboring blocks, the photons stored at Alice and Bob memories will be correlated. Figure from https://qt.eu/discover-quantum/underlying-principles/quantum-repeaters/

The SPDC process has been the most studied photon source over the years. It has some features that facilitate applications, like scalability [16] and the possibility of building robust systems [17]. There are also services of quantum security based on quantum key distribution [18] with SPDC sources being offered commercially [19]. These sources can be reduced in size and moved outside laboratory conditions in order to have daily-life applications. However, using atomic sources of light we can reach a higher degree of control of the photon parameters because it is possible to selectively prepare the atomic states using high-precision spectroscopy. Alkaline atoms facilitate this kind of experiments, since they have only one electron in their outer shell.

Atomic ensembles are a complement to SPDC technology because in addition to photon pair generation we can make quantum memories [20] and the possibility of repeaters with them [21]. Great progress has been made recently regarding this kind of systems: quantum memories at single-photon level [22], multiplexed memories [23], a memory

of a single atom [24], a deterministic photon source based on a quantum memory [25] and a quantum network of hundreds of kilometers that connect two room-temperature quantum memories [26].

Two of the most commonly used energy level systems for implementing FWM in atomic gases are the diamond and the double-Λ configurations, shown in Figure 1.2. In the diamond configuration, there is a ladder-type excitation from state $|0\rangle$ to $|2\rangle$ and a double cascade-decay from $|2\rangle$ to $|0\rangle$. The double-Λ system consists of an excitation from level $|0\rangle$ to $|2\rangle$ followed by a decay from $|2\rangle$ to level $|1\rangle$, then another excitation from $|1\rangle$ to $|3\rangle$ and finally a decay from $|3\rangle$ to $|0\rangle$. The decays of this process produce signal and idler photons, as indicated in Figure 1.2.

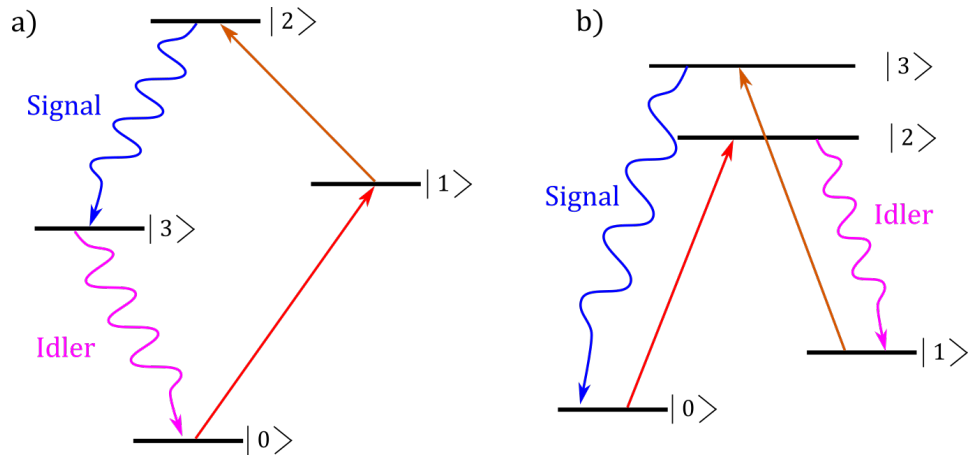

Figure 1.2: Typical energy level schemes for a FWM process. The straight lines represent the excitation of transitions while the curly lines are the generated signal and idler photons.

1.2 Description of this work

Laser cooling [27] is a well-known technique to trap atoms. Since its development in the 80s [28], it has been widely used for various lines of research: it is the initial step to

create Bose-Einstein condensates [29], to study the fundamentals of quantum mechanics like quantum jumps [30] and a single-photon interacting with a single atom [31]. It is used also for applications, like metrology [32], atomic clocks [33] and the studies of quantum communications, like quantum memories [34], or quantum encryption [35].

In this work I describe our experimental apparatus built in the Cold Atoms and Quantum Optics Laboratory (LAFriOC, IF-UNAM) capable of generating photon pairs by a nonlinear FWM process in a diamond configuration using the atomic Rubidium isotope 87. The energy levels used are: $|0\rangle = 5S_{1/2}$, $|1\rangle = 5P_{3/2}$, $|2\rangle = 5D_{3/2}$ and $|3\rangle = 5P_{1/2}$ and the emitted photons have near-infrared wavelength: 762 nm for the signal and 795 nm for the idler, as described in Figure 1.2.

This Thesis is organized as follows: Chapter 2 contains the theoretical framework of FWM in the diamond scheme. It begins by studying the classical electromagnetic fields and their canonical quantization. Then the correlation functions between two random variables and their relevance to the coherence theory is discussed. The interaction Hamiltonian regarding a FWM process is considered to deduce the phase-matching conditions. This chapter concludes with a proposal to solve numerically the atomic system.

Chapter 3 contains a description of the experimental setup: our laser system and control, the optical pumping, our cooling system to create a magneto-optical trap (MOT), and our optical setup for single-photon detection. Chapter 4 has our main results: using a consecutive decay model we fit the experimental data for the cross-correlation function between the signal and idler photons and their autocorrelations. We measured an heralded coherence time for the cross-correlation and a thermal coherence time for the autocorrelation. We also measured a strong violation of the Cauchy-Schwarz inequality $R = (4.49 \pm 0.43) \times 10^5 > 1$, which means that the time coherence of our photon pairs is highly non-classical. Chapter 5 presents numerical calculations of the master equations

to calculate the cross-correlation function. Finally, Chapter 6 gives a summary of our results and an outlook for future experiments.

Chapter 2

Theory

Our experiment with cold atoms produces photon pairs. To describe them and design an adequate detection system we need to understand the quantization of the electromagnetic field. In this chapter we build a model to describe the quantized radiation field together with a description of the atomic interaction with light. To understand the statistics of the generated photons we also study the correlation functions between fields.

2.1 Classical electromagnetic fields

We consider the behaviour of the classical electric $\mathbf{E}(\mathbf{r},t)$ and magnetic $\mathbf{B}(\mathbf{r},t)$ fields in free space, without boundaries and sources, described by the Maxwell equations [36]

$$\begin{aligned} \vec{\nabla}\cdot\mathbf{E}=0, &\vec{\nabla}\times\mathbf{E}=-\frac{\partial\mathbf{B}}{\partial t},\\ \vec{\nabla}\cdot\mathbf{B}=0, &\vec{\nabla}\times\mathbf{B}=\epsilon_0\mu_0\frac{\partial\mathbf{E}}{\partial t}, \end{aligned} \tag{2.1}$$

manipulating these expressions and considering the following identity for any given operator $\mathcal{O}$: $\vec{\nabla}\times(\vec{\nabla}\times\mathcal{O})=\vec{\nabla}(\vec{\nabla}\cdot\mathcal{O})-\nabla^2\mathcal{O}$, we can obtain a homogeneous wave equation for each field

$$\begin{aligned} \nabla^2\mathbf{E}-\frac{1}{c^2}\frac{\partial^2\mathbf{E}}{\partial t^2}=0,\\ \nabla^2\mathbf{B}-\frac{1}{c^2}\frac{\partial^2\mathbf{B}}{\partial t^2}=0, \end{aligned} \tag{2.2}$$

where $c = 1/\sqrt{\epsilon_0\mu_0}$, c is the speed of light, ϵ_0 the permittivity of vacuum and μ_0 its permeability. This system of partial differential equations has various solutions. In Cartesian coordinates they can be written as

$$\begin{aligned} \mathbf{E}(\mathbf{r},t) &= \mathbf{E}_0 \exp\{i(\mathbf{k}\cdot\mathbf{r} - \omega t)\}, \\ \mathbf{B}(\mathbf{r},t) &= \mathbf{B}_0 \exp\{i(\mathbf{k}\cdot\mathbf{r} - \omega t)\}, \end{aligned} \tag{2.3}$$

where $\mathbf{k}$ is the propagation vector of the light, $\mathbf{r}$ is the position vector and ω its angular frequency. Vectors $\mathbf{E}_0$ and $\mathbf{B}_0$ are the amplitudes of the fields and their directions. It is well known that we can express both fields in general by using the vector potential $\mathbf{A}(r,t)$,

$$\mathbf{B}(\mathbf{r},t) = \vec{\nabla}\times\mathbf{A}(\mathbf{r},t)\ , \qquad \mathbf{E}(\mathbf{r},t) = -\frac{\partial\mathbf{A}(\mathbf{r},t)}{\partial t}. \tag{2.4}$$

Along with the divergence condition

$$\vec{\nabla}\cdot\mathbf{A}(\mathbf{r},t) = 0, \tag{2.5}$$

which is known as the Coulombs gauge, it is straightforward to show that this vector potential also satisfies

$$\nabla^2\mathbf{A} - \frac{1}{c^2}\frac{\partial^2\mathbf{A}}{\partial t^2} = 0, \tag{2.6}$$

which is another homogeneous wave equation.

2.1.1 Expansion of the plane wave

Making a Fourier decomposition of the potential vector $\mathbf{A}(\mathbf{r},t)$ in Cartesian coordinates and imposing periodical boundaries in a cube of side L, we obtain

$$\mathbf{A}(\mathbf{r},t) = \frac{1}{\epsilon_0^{1/2}L^{3/2}}\sum_k \mathbf{a}_k(t)e^{i\mathbf{k}\cdot\mathbf{r}}, \tag{2.7}$$

where $\mathbf{k}$ represents the direction of propagation and $\mathbf{a}_k$ are the coefficients of the Fourier series. If we substitute equation (2.7) into equation (2.6), and by applying the operator ∇^2 we get a factor $-k^2$ from the exponential, obtaining

$$\frac{1}{\epsilon_0^{1/2}} \sum_k \left(-k^2 - \frac{1}{c^2} \frac{\partial^2}{\partial t^2} \right) \mathbf{a}_k(t) e^{i\mathbf{k}\cdot\mathbf{r}} = 0, \tag{2.8}$$

for all $\mathbf{r}$ and all $\mathbf{k}$, so if we consider the dispersion relationship $c = \omega/k$ with $k = |\mathbf{k}|$ the result is

$$\left(\frac{\partial^2}{\partial t^2} + \omega_k^2 \right) \mathbf{a}_k = 0, \tag{2.9}$$

which is the equation of the harmonic oscillator for each term in the sum. The general solution of this equation is

$$\mathbf{a}_k = \mathbf{c}_k e^{-i\omega t} + \mathbf{c}_k{}^* e^{i\omega t}. \tag{2.10}$$

It is worth noting that we can separate the vectorial part of this quantity by $\mathbf{c}_k = \hat{\epsilon}_k c_k$, with $\hat{\epsilon}_k$ a unitary vector, and $c_k = \sqrt{\hbar\omega_k/2\epsilon_0 L^3}$. This unitary vector will correspond to the polarization directions of the light, because the condition of equation (2.5), could also be viewed as $\mathbf{k} \cdot \mathbf{a}_k(t) = 0$ and thus they correspond to the transversal components of the field. By substituting equation (2.10) in the Fourier decomposition of equation (2.7), we obtain

$$\begin{aligned} \mathbf{A}(\mathbf{r}, t) &= \frac{1}{\epsilon_0^{1/2} L^{3/2}} \sum_k \sum_s [c_{k,s} \hat{\epsilon}_{k,s} e^{-i\omega t} + c_{k,s}^* \hat{\epsilon}_{-k,s}^* e^{i\omega t}] e^{i\mathbf{k}\cdot\mathbf{r}}, \\ &= \frac{1}{\epsilon_0^{1/2} L^{3/2}} \sum_k \sum_s [c_{k,s} \hat{\epsilon}_{k,s} e^{i(\mathbf{k}\cdot\mathbf{r} - \omega t)} + c_{k,s}^* \hat{\epsilon}_{-k,s}^* e^{-i(\mathbf{k}\cdot\mathbf{r} - \omega t)})], \\ &= \frac{1}{\epsilon_0^{1/2} L^{3/2}} \sum_k \sum_s [u_{k,s} \hat{\epsilon}_{k,s} e^{i\mathbf{k}\cdot\mathbf{r}} + u_{k,s}^* \hat{\epsilon}_{-k,s}^* e^{-i\mathbf{k}\cdot\mathbf{r}}], \end{aligned} \tag{2.11}$$

where the sum over the index s represents the sum over each component of the polarization directions that we could have and $u_{k,s}(t) = c_{k,s} e^{-i\omega t}$. Using the definition of the

vector potential in equation (2.4) we can also express the electrical and magnetic fields in terms of these harmonic oscillators

$$\mathbf{E}(\mathbf{r},t) = \frac{i}{\epsilon_0^{1/2} L^{3/2}} \sum_k \sum_s \omega [u_{k,s}(t)\hat{\epsilon}_{k,s} e^{i\mathbf{k}\cdot\mathbf{r}} + u^*_{k,s}(t)\hat{\epsilon}^*_{k,s} e^{-i\mathbf{k}\cdot\mathbf{r}}], \tag{2.12}$$

$$\mathbf{B}(\mathbf{r},t) = \frac{i}{\epsilon_0^{1/2} L^{3/2}} \sum_k \sum_s [u_{k,s}(t)(\mathbf{k}\times\hat{\epsilon}_{k,s}) e^{i\mathbf{k}\cdot\mathbf{r}} + u^*_{k,s}(t)(\mathbf{k}\times\hat{\epsilon}^*_{k,s}) e^{-i\mathbf{k}\cdot\mathbf{r}}]. \tag{2.13}$$

Up to this point we have only considered classical fields. We now follow the steps needed for their quantization. For that matter, it will be useful to calculate the energy of the system [36]

$$H = \frac{1}{2}\int_{L^3} [\epsilon_0 E^2(\mathbf{r},t)] d^3r, \tag{2.14}$$

where L^3 is the integration volume. Solving this integral, gives

$$\begin{aligned} H &= \frac{1}{2}\int_{L^3} [\epsilon_0 |\mathbf{E}\cdot\mathbf{E}^*|] d^3r, \\ &= \frac{1}{2\epsilon_0 L^3} \sum_{k,k'} \sum_{s,s'} \int_{L^3} [\epsilon_0 \omega^2 u_{k,s}(t) u^*_{k',s'}(t) e^{i(\mathbf{k}-\mathbf{k'})\cdot\mathbf{r}}] d^3r, \\ &= \frac{1}{2L^3} \sum_{k,k'} \sum_{s,s'} \omega^2 u_{k,s}(t) u^*_{k',s'}(t) \int_{L^3} e^{i(\mathbf{k}-\mathbf{k'})\cdot\mathbf{r}} d^3r, \\ &= \frac{1}{2L^3} \sum_{k,k'} \sum_{s,s'} \omega^2 u_{k,s}(t) u^*_{k',s'}(t) L^3 \delta_{\mathbf{k},\mathbf{k}'}\delta_{s,s'}, \\ &= \frac{1}{2} \sum_k \sum_s \omega^2 |u_{k,s}(t)|^2. \end{aligned} \tag{2.15}$$

Now we introduce a pair of canonical variables $Q_{k,s}$ and $P_{k,s}$, defined as

$$\begin{aligned} Q_{k,s}(t) &= [u_{k,s}(t) + u^*_{k,s}(t)], \\ P_{k,s}(t) &= -i\omega[u_{k,s}(t) - u^*_{k,s}(t)], \end{aligned} \tag{2.16}$$

which are the real and imaginary part of $u_{k,s}(t) = (Q_{k,s}(t) + iP_{k,s}(t))$. If we recall the time dependence of $u_{k,s}(t) = c_{k,s}e^{-i\omega t}$, we can obtain the evolution of $Q_{k,s}(t)$ and $P_{k,s}(t)$

$$\begin{aligned}\frac{\partial}{\partial t}Q_{k,s}(t) &= P_{k,s}(t),\\ \frac{\partial}{\partial t}P_{k,s}(t) &= -\omega^2 Q_{k,s}(t),\end{aligned} \tag{2.17}$$

so we can finally express the energy H as a function of the canonical variables

$$H = \frac{1}{2}\sum_k \sum_s [P^2_{k,s}(t) + \omega^2 Q^2_{k,s}(t)]. \tag{2.18}$$

Once we write the energy, we can apply the usual steps for the canonical quantization.

2.2 Quantization of the electromagnetic field

This formalism indicates that we have to associate the dynamic variables of the classic theory p_i, q_i with operators in a Hilbert space $\hat{p}_i$, $\hat{q}_i$. Usually, we denote the difference between operators and dynamic variables with a "hat" symbol in the operators upper part. In addition to this, a postulate indicates that we have to impose the canonical commutation relationship between each pair of those operators $[\hat{p}, \hat{q}] = i\hbar$.

For the electromagnetic field, there are a pair of canonical variables $P_{k,s}(t)$ and $Q_{k,s}(t)$, as defined in equation (2.16), quantum mechanics postulates indicate that they follow the canonical commutation relations:

$$\begin{aligned}[\hat{Q}_{k,s}(t), \hat{P}_{k',s'}(t)] &= i\hbar\delta^3_{k,k'}\delta_{s,s'},\\ [\hat{Q}_{k,s}(t), \hat{Q}_{k',s'}(t)] &= 0,\\ [\hat{P}_{k,s}(t), \hat{P}_{k',s'}(t)] &= 0.\end{aligned} \tag{2.19}$$

Then, equation (2.18) can be now expressed as the Hamiltonian operator of the quantized radiation field

$$\hat{H} = \frac{1}{2}\sum_k \sum_s [\hat{P}^2_{k,s}(t) + \omega^2 \hat{Q}^2_{k,s}(t)], \tag{2.20}$$

where, if we define the well-known annihilation and creation operators

$$\hat{a}_{k,s} = \frac{1}{\sqrt{2}}(\hat{Q}_{k,s} + i\hat{P}_{k,s}), \qquad \hat{a}^{\dagger}_{k,s} = \frac{1}{\sqrt{2}}(\hat{Q}_{k,s} - i\hat{P}_{k,s}), \tag{2.21}$$

the subscripts k and s in equation (2.21) refer to each mode k, with polarization s. The Hamiltonian then simplifies into

$$\hat{H} = \sum_{k}\sum_{s} \hbar\omega_k \left(\hat{a}^{\dagger}_{k,s}\hat{a}_{k,s} + \frac{1}{2}\right), \tag{2.22}$$

where we use the commutation relation $[\hat{a}_{k,s}, \hat{a}^{\dagger}_{k,s}] = \delta_{kk'}\delta_{ss'}$ to invert the order of the operator $\hat{a}_{k,s}\hat{a}^{\dagger}_{k,s}$ and obtaining the factor $\frac{1}{2}$ in the simplifying process. After performing the canonical quantization, we can express the electric and magnetic fields in terms of the annihilation and creation operators

$$\hat{E}(\mathbf{r}, t) = \frac{i}{L^{3/2}} \sum_{k}\sum_{s} \left(\frac{\hbar\omega}{2\epsilon_0}\right)^{1/2} (\hat{a}_{k,s}(t)\hat{\epsilon}_{k,s}e^{i\mathbf{k}\cdot\mathbf{r}} + \hat{a}^{\dagger}_{k,s}(t)\hat{\epsilon}^{*}_{k,s}e^{-i\mathbf{k}\cdot\mathbf{r}}), \tag{2.23}$$

and

$$\hat{B}(\mathbf{r}, t) = \frac{i}{L^{3/2}} \sum_{k}\sum_{s} \left(\frac{\hbar}{2\omega\epsilon_0}\right)^{1/2} (\hat{a}_{k,s}(t)(\mathbf{k}\times\hat{\epsilon}_{k,s})e^{i\mathbf{k}\cdot\mathbf{r}} + \hat{a}^{\dagger}_{k,s}(t)(\mathbf{k}\times\hat{\epsilon}^{*}_{k,s})e^{-i\mathbf{k}\cdot\mathbf{r}}). \tag{2.24}$$

At this stage, let us recall some basic aspects of the quantum theory [37]. The state of the field is described by a vector $|\psi\rangle$ in a Hilbert space, commonly known as ket. The time evolution of this state is governed by the Schrödinger equation, and in general, there are three representations for this description: the Schrödinger picture, where the operators remain constant in time, and the state vectors evolve; the Heisenberg picture, where the kets remain constant, and the operators evolve in time; and the interaction picture where both operators and states evolve in time. Each physical observable has a Hermitian operator $\hat{O}$ associated with it, and when we measure that observable we obtain an eigenvalue O of that operator. The fact that those operators $\hat{O}$ have to be Hermitian is a necessary condition because the eigenvalues of such operators are real. In

general, when we make a measurement of the operator $\hat{O}$ as the system is in the state $|\psi\rangle$, the result can be written in terms of the Born rule

$$\langle \hat{O} \rangle = \sum_i O_i P_i, \tag{2.25}$$

where P_i is the probability of measuring the eigenvalue O_i, given by the projection of the state $|\psi\rangle$ into the eigenvector $|o_i\rangle$ of such operator: $P_i = |\langle o_i|\psi\rangle|^2$, assuming the eigenvector set $|o_i\rangle$ are orthogonal.

2.3 Quantum detection theory and correlation functions

Glauber first worked out the theory of photodetection based on quantum electrodynamics (QED) and then defined multi-order correlation functions similar to the classical coherence theory [8].

Recalling the expression for the electric field in equation (2.23), and consider only the positive oscillating part, where only the annihilation operator $\hat{a}_{k,s}$ is present. In the process of detecting photons, the detector absorbs a photon and transforms it into a photo-electron, that produces a photo-electrical current via the photoelectric effect. So in this process we will have the annihilation operator present due to the absorption of this photon. Suppose that we have an initial state $|i\rangle$ and after the detection we end in a final state $|f\rangle$ then the expectation value of the photodetection process is

$$\langle f|\hat{E}^{(+)}(\mathbf{r},t)|i\rangle, \tag{2.26}$$

where $\mathbf{r}$ is the position of the detector and t the time when the detection is registered. If we consider an ideal photodetector with frequency-independent absorption probability, the detection rate will be proportional to the sum of the squared matrix elements over all final states $|f\rangle$ [8]

$$\begin{aligned}\sum_f |\langle f|\hat{E}^{(+)}(\mathbf{r},t)|i\rangle|^2 &= \sum_f (\langle f|\hat{E}^{(+)}(\mathbf{r},t)|i\rangle)^\dagger \langle f|\hat{E}^{(+)}(\mathbf{r},t)|i\rangle, \\ &= \sum_f \langle i|\hat{E}^{(-)}(\mathbf{r},t)|f\rangle\langle f|\hat{E}^{(+)}(\mathbf{r},t)|i\rangle, \\ &= \langle i|\hat{E}^{(-)}(\mathbf{r},t)\hat{E}^{(+)}(\mathbf{r},t)|i\rangle,\end{aligned} \tag{2.27}$$

where we use that all the final states $|f\rangle$ form a complete basis and $(\hat{E}^{(+)}(\mathbf{r},t))^\dagger = \hat{E}^{(-)}(\mathbf{r},t)$ and $\hat{E}^{(-)}$ refers to the negative oscillating part of the electric field that is obtained by taking the Hermitian conjugate of equation (2.23). A completely similar procedure can be performed for the case where there are two different detectors in positions $\mathbf{r}_1$ and $\mathbf{r}_2$. In such case, the matrix element related to the photodetection process is

$$\langle f|\hat{E}^{(+)}(\mathbf{r}_1,t_1)\hat{E}^{(+)}(\mathbf{r}_2,t_2)|i\rangle, \tag{2.28}$$

and thus, the probability related to the matrix element is:

$$\langle i|\hat{E}^{(-)}(\mathbf{r}_2,t_2)\hat{E}^{(-)}(\mathbf{r}_1,t_1)\hat{E}^{(+)}(\mathbf{r}_1,t_1)\hat{E}^{(+)}(\mathbf{r}_2,t_2)|i\rangle. \tag{2.29}$$

Using these ideas, we can define a series of functions to measure the correlations of electric fields. In general, the correlation function of degree N is defined as

$$G^{(N)}(\mathbf{x}_1,\mathbf{x}_2,...\mathbf{x}_N) = \langle\psi|\hat{E}^{(-)}(\mathbf{x}_1)...\hat{E}^{(-)}(\mathbf{x}_N)\hat{E}^{(+)}(\mathbf{x}_N)...\hat{E}^{(+)}(\mathbf{x}_1)|\psi\rangle, \tag{2.30}$$

with $\mathbf{x}_i = \mathbf{r}_i, t_i$. Those correlation functions determine coherence properties of the fields. The first order correlation function $G^{(1)}$, which is the correlation of the field operator, measure the spatial coherence of optical fields and the visibility of their interference fringes. The second order $G^{(2)}$, correlation of intensity, determines the temporal coherence. In section (4.2.1) we present how we can measure experimentally the correlation functions.

2.4 Four-wave mixing

Four-wave mixing is a non-linear optical process involving four electromagnetic fields. In this process, the interaction of two or three fields with a medium generates one or two radiation fields. In general, the polarization $\mathbf{P}$ of a medium in the presence of an applied optical field $\mathbf{E}$ can be described as a series [38]

$$\mathbf{P} = \epsilon_0[\chi^{(1)}\mathbf{E} + \chi^{(2)} : \mathbf{EE} + \chi^{(3)} : \mathbf{EEE} + ...], \tag{2.31}$$

where the n-order non-linear susceptibilities $\chi^{(n)}$ are n-rank tensors respectively and the operation : means a summation over all the possible contributions of the susceptibility tensor $\chi^{(n)}$ in each direction of the fields $\mathbf{E}$. Our non-linear medium is an atomic cloud it is centrosymmetric, so the non-zero susceptibilities would be the odd terms. In a non-centrosymmetric medium, like the crystals used in SPDC, the non-zero terms are the even [38]. The susceptibility regarding FWM is $\chi^{(3)}$. The interaction Hamiltonian for a FWM process in the interaction picture is given by [38]

$$H_I = \frac{\epsilon_0}{4}\int_V d^3r \left(\chi^{(3)} : \mathbf{E}_1^{(+)}\mathbf{E}_2^{(+)}\mathbf{E}_3^{(-)}\mathbf{E}_4^{(-)} + \chi^{(3)} : \mathbf{E}_1^{(-)}\mathbf{E}_2^{(-)}\mathbf{E}_3^{(+)}\mathbf{E}_4^{(+)}\right). \tag{2.32}$$

In our case, we have to express each component of the fields involved in the FWM. As shown in Figure 2.1, we send two laser beams $p1$ and $p2$ with different frequencies ω_1 and ω_2 to the atomic medium, and generate two photons with frequencies ω_s and ω_i. Since the two initial fields $p1$ and $p2$ are lasers, we can model them as classical monochromatic propagating plane waves.

$$\begin{aligned}\mathbf{E}_{p1}^{+}(\mathbf{r},t) =& \vec{E}_{p1}e^{i[\mathbf{k}_{p1}\cdot\mathbf{r}-\omega_{p1}t]},\\ \mathbf{E}_{p2}^{+}(\mathbf{r},t) =& \vec{E}_{p2}e^{i[\mathbf{k}_{p2}\cdot\mathbf{r}-\omega_{p2}t]},\end{aligned} \tag{2.33}$$

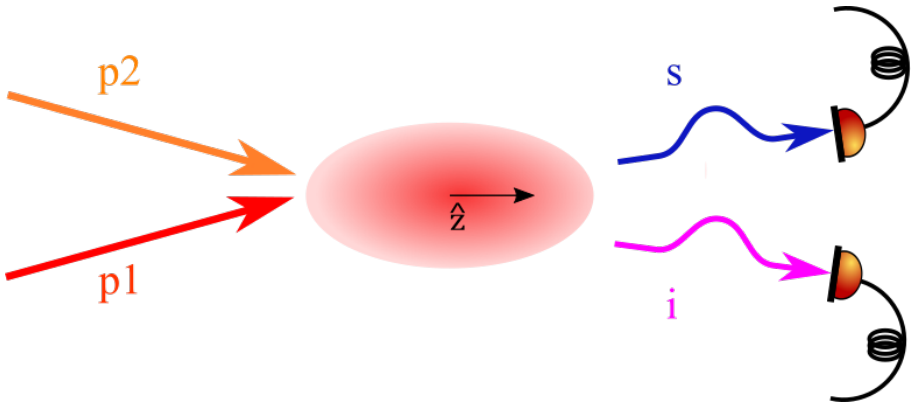

Figure 2.1: Schematics of a FWM process in an atomic cloud. Sending two frequencies $p1$ and $p2$ produce two other different frequencies s and i.

where E_{pi} is the amplitude of each pumping field $i = 1, 2$. The output fields are photons with frequencies ω_s and ω_i respectively, so we model them as quantized fields using equation (2.23):

$$\begin{aligned}\hat{E}_s^{(+)}(\mathbf{r},t) &= \frac{i}{L^{3/2}}\left(\frac{\hbar\omega_s}{2\epsilon_0}\right)^{1/2}\hat{a}_{k,s}(t)e^{i\mathbf{k}_s\cdot\mathbf{r}}\hat{\epsilon}_{k,s},\\ \hat{E}_i^{(+)}(\mathbf{r},t) &= \frac{i}{L^{3/2}}\left(\frac{\hbar\omega_i}{2\epsilon_0}\right)^{1/2}\hat{a}_{k,s}(t)e^{i\mathbf{k}_i\cdot\mathbf{r}}\hat{\epsilon}_{i,s},\end{aligned} \tag{2.34}$$

making a Fourier transform of the annihilation operators, we obtain

$$\begin{aligned}\hat{E}_s^{(+)}(\mathbf{r},\omega) &= \frac{i}{L^{3/2}}\int d\omega\frac{\hat{\epsilon}_{k,s}}{\sqrt{2\pi}}\left(\frac{\hbar\omega_s}{2\epsilon_0}\right)^{1/2}\hat{a}_{k,s}(\omega)e^{i(\mathbf{k}_s\cdot\mathbf{r}-\omega t)},\\ \hat{E}_i^{(+)}(\mathbf{r},\omega) &= \frac{i}{L^{3/2}}\int d\omega\frac{\hat{\epsilon}_{i,s}}{\sqrt{2\pi}}\left(\frac{\hbar\omega_i}{2\epsilon_0}\right)^{1/2}\hat{a}_{k,s}(\omega)e^{i(\mathbf{k}_i\cdot\mathbf{r}-\omega t)}.\end{aligned} \tag{2.35}$$

Substituting this into the equation (2.32) the interaction Hamiltonian becomes

$$\begin{aligned}H_I = \frac{\epsilon_0}{4}\int_V d^3r\,\Big(\chi^{(3)}E_{p1}e^{(i\mathbf{k}_{p1}\cdot\mathbf{r}-\omega_{p1}t)}\,E_{p2}e^{-i(\mathbf{k}_{p2}\cdot\mathbf{r}-\omega_{p2}t)}\left[\frac{i}{L^{3/2}}\int d\omega_s\frac{1}{\sqrt{2\pi}}\left(\frac{\hbar\omega_s}{2\epsilon_0}\right)^{1/2}\hat{a}^\dagger_{k,s}(\omega_s)e^{-i(\mathbf{k}_s\cdot\mathbf{r}-\omega_s t)}\right]\\ \times\left[\frac{i}{L^{3/2}}\int d\omega_i\frac{1}{\sqrt{2\pi}}\left(\frac{\hbar\omega_i}{2\epsilon_0}\right)^{1/2}\hat{a}^\dagger_{k,s}(\omega_i)e^{-i(\mathbf{k}_i\cdot\mathbf{r}-\omega_i t)}\right]+h.c.\Big),\end{aligned} \tag{2.36}$$

where the $h.c$ represents the Hermitian conjugate. Re-arranging and factorizing the exponential terms we have

$$H_I = \frac{\epsilon_0}{4}\int_V d^3r \left(\chi^{(3)} E_{p1} E_{p2} e^{i\Delta\mathbf{k}\cdot\mathbf{r}} \frac{\hbar}{4\pi\epsilon_0 L^3}\int d\omega_s \int d\omega_i \hat{a}^\dagger_{k,s}(\omega_s)\hat{a}^\dagger_{k,s}(\omega_i)e^{-i\Delta\omega t} + h.c.\right), \tag{2.37}$$

where: $\Delta\mathbf{k} = \mathbf{k}_{p1} + \mathbf{k}_{p2} - \mathbf{k}_s - \mathbf{k}_i$ and $\Delta\omega = \omega_{p1} + \omega_{p2} - \omega_s - \omega_i$. Performing the spatial integral in the direction z' parallel to the vector $\Delta\mathbf{k}$

$$\begin{aligned}
\int_V e^{i\Delta k z'} d^3r &= \int_{-L/2}^{L/2} L^2 e^{i\Delta k z} dz', \\
&= L^2 \frac{1}{i\Delta k} e^{i\Delta k z'}\Big|_{-L/2}^{L/2}, \\
&= \frac{L^2}{i\Delta k}(e^{i\Delta k L/2} - e^{-i\Delta k L/2}), \\
&= \frac{2L^2}{\Delta k}\sin(\Delta k L/2), \\
&= L\frac{\sin(\Delta k L/2)}{\Delta k L/2}, \\
&= L\,\mathrm{sinc}(\Delta k L/2),
\end{aligned} \tag{2.38}$$

thus equation (2.37) becomes

$$H_I = \frac{i\hbar L}{2\pi}\int d\omega_s \int d\omega_i \left(-i\frac{\sqrt{\omega_s\omega_i}}{2c}\chi^{(3)} E_{p1} E_{p2}\,\mathrm{sinc}\left(\frac{\Delta k L}{2}\right)\hat{a}^\dagger_{k,s}(\omega_s)\hat{a}^\dagger_{k,s}(\omega_i)e^{-i\Delta\omega t} + h.c.\right). \tag{2.39}$$

The position-dependent term can be written as

$$\mathrm{sinc}\left(\frac{\Delta\mathbf{k}\cdot L\hat{z}}{2}\right). \tag{2.40}$$

If $\Delta\mathbf{k} = 0$ this term becomes one, the H_I reach its maximum value meaning the maximum generation of photons. *The phase-matching condition* is

$$\mathbf{k}_{p1} + \mathbf{k}_{p2} = \mathbf{k}_s + \mathbf{k}_i. \tag{2.41}$$

The wavevector $\mathbf{k}$ is strongly related to the momentum of the wave, we can interpret the phase-matching condition as a conservation of momentum from the pumping waves and the signal and idler photons.

In a practical way, this relationship tells us that the sum of the pumping waves incident angles must be equal to the sum of the outgoing angles of the signal and idler photons. As we mention in section 3.4 the pumping fields are sent collinear in our experiments. Thus, the generated photons are expected to propagate in the same direction as the FWM laser beams.

Analogously, if we consider a time integral of equation (2.37), we can deduce the condition $\Delta\omega = 0$. It means that the sum of the frequencies of the pump beams must be equal to the frequencies of the emitted photons, i.e., $\omega_{p1} + \omega_{p2} = \omega_s + \omega_i$.

2.5 Dipole interaction between light and atoms

We seek to describe the interaction of atoms and light with quantum mechanics. This is done with the Jaynes-Cummings model [39]. The excitation transitions considered are dipolar, so we deduce an interaction term using the dipolar approximation.

2.5.1 Hamiltonian in the dipole approximation

We consider the most simple atom: a nucleus composed by a proton of mass m_p at a position $\mathbf{r}_p$ and an electron with m_e at $\mathbf{r}_e$ with a Coulombian interaction $V(|\mathbf{r}_p - \mathbf{r}_e|)$. This is a good approximation for an alkaline atoms. The total Hamiltonian is [37]

$$H_0 = H_p + H_e + V(|\mathbf{r}_p - \mathbf{r}_e|). \tag{2.42}$$

In terms of the center of mass position $\mathbf{R}$ and the relative coordinate $\mathbf{r} = \mathbf{r}_e - \mathbf{r}_p$ with $M = m_p + m_e$, we can express the positions $\mathbf{r}_p$ and $\mathbf{r}_e$ as

$$\mathbf{r}_p = \mathbf{R} - \frac{\mu}{m_p}\mathbf{r} \qquad , \qquad \mathbf{r}_e = \mathbf{R} + \frac{\mu}{m_e}\mathbf{r}, \tag{2.43}$$

where the reduced mass is defined as $\mu = m_p m_e/(m_p+m_e)$, while the momenta associated with those new coordinates is

$$\mathbf{P} = \mathbf{p}_p + \mathbf{p}_e \qquad \mathbf{p} = \frac{\mu}{m_e}\mathbf{p}_e - \frac{\mu}{m_p}\mathbf{p}_p. \tag{2.44}$$

So the corresponding Hamiltonian in those coordinates is

$$H_0 = \frac{\mathbf{p}_p^2}{2m_p} + \frac{\mathbf{p}_e^2}{2m_e} + V = \frac{\mathbf{P}^2}{2M} + \frac{\mathbf{p}^2}{2\mu} + V, \tag{2.45}$$

which corresponds to the sum of the kinetic energy and potential energy terms associated with the new coordinates. According to the minimal coupling [40], where we have the prescription to replace the canonical momentum $\mathbf{p}$ by $\mathbf{p} - e\mathbf{A}$ in the Hamiltonian, we have

$$H = \frac{1}{2m}[\mathbf{p} - e\mathbf{A}(\mathbf{r},t)]^2, \tag{2.46}$$

so, for each coordinate

$$\begin{aligned} H_R &= \frac{1}{2M}[\mathbf{P}^2 - e\mathbf{P}\cdot\mathbf{A}(\mathbf{R},t) - e\mathbf{A}(\mathbf{R},t)\cdot\mathbf{P} + e^2\mathbf{A}^2(\mathbf{R},t)], \\ H_r &= \frac{1}{2\mu}[\mathbf{p}^2 - e\mathbf{p}\cdot\mathbf{A}(\mathbf{r},t) - e\mathbf{A}(\mathbf{r},t)\cdot\mathbf{p} + e^2\mathbf{A}^2(\mathbf{r},t)]. \end{aligned} \tag{2.47}$$

Using the *Coulomb gauge* one can prove that $\mathbf{p}\cdot\mathbf{A} = \mathbf{A}\cdot\mathbf{p}$ so we can sum the two middle terms for each case

$$\begin{aligned} H &\simeq \frac{1}{2M}[\mathbf{P}^2 - 2e\mathbf{P}\cdot\mathbf{A}(\mathbf{R},t)] + \frac{1}{2\mu}[\mathbf{p}^2 - 2e\mathbf{p}\cdot\mathbf{A}(\mathbf{r},t)] + V, \\ &= \frac{\mathbf{P}^2}{2M} + \frac{\mathbf{p}^2}{2\mu} - \frac{e\mathbf{P}\cdot\mathbf{A}(\mathbf{R},t)}{M} - \frac{e\mathbf{p}\cdot\mathbf{A}(\mathbf{r},t)}{\mu} + V, \\ &= H_0 - \frac{e\mathbf{P}\cdot\mathbf{A}(\mathbf{R},t)}{M} - \frac{e\mathbf{p}\cdot\mathbf{A}(\mathbf{r},t)}{\mu}, \\ &= H_0 - \frac{e\mathbf{P}\cdot\mathbf{A}(\mathbf{R},t)}{M} - \frac{e\mathbf{p}\cdot\mathbf{A}(\mathbf{r},t)}{m_e} - \frac{e\mathbf{p}\cdot\mathbf{A}(\mathbf{r},t)}{m_p}, \end{aligned} \tag{2.48}$$

where we also neglected the terms proportional to A^2. If we assume the mass between particles $m_p >> m_e$ so we can approximate $M \sim m_p$. The only non-zero term is

$$H \simeq H_0 - \frac{e\mathbf{p}\cdot\mathbf{A}(\mathbf{r},t)}{m_e} \simeq H_0 - \frac{e\mathbf{p}\cdot\mathbf{A}(\mathbf{R},t)}{m_e}, \tag{2.49}$$

where the last equality its true by applying the *electric dipole approximation*, $\mathbf{A}(\mathbf{r},t) \simeq \mathbf{A}(\mathbf{R},t)$ which takes into account only the first term in the dipole expansion of the potential vector $\mathbf{A}(\mathbf{r},t)$. Physically this approximation means that because the Coulomb potential keeps the electron close, the external field irradiated to the atom would be the same for the electron and the nucleus. Now, using the canonical commutator relations between the operators $[\hat{\mathbf{r}},\hat{\mathbf{p}}] = i\hbar$ we can express $\hat{p}$ in the form:

$$\begin{aligned} \hat{\mathbf{p}} = \mathbb{1}\hat{\mathbf{p}} &= \frac{[\hat{\mathbf{r}},\hat{\mathbf{p}}]}{i\hbar}\hat{\mathbf{p}}, \\ &= \frac{1}{2i\hbar}[\hat{\mathbf{r}},\hat{\mathbf{p}}^2], \\ &= \frac{\mu}{i\hbar}\left[\hat{\mathbf{r}},\frac{\hat{\mathbf{p}^2}}{2\mu}\right], \end{aligned} \tag{2.50}$$

and since $\mathbf{r}$ commute with the operator $\mathbf{P}$ and also with $V(\mathbf{r})$

$$\mathbf{p} = \frac{\mu}{i\hbar}\left[\mathbf{r},\frac{\mathbf{p}^2}{2\mu} + \frac{\mathbf{P}^2}{2\mu} + V\right] = \frac{-\mu}{i\hbar}\left[\frac{\mathbf{p}^2}{2\mu} + \frac{\mathbf{P}^2}{2\mu} + V,\mathbf{r}\right] = \frac{i\mu}{\hbar}\left[H_0,\mathbf{r}\right], \tag{2.51}$$

so substituting this equality in equation (2.49)

$$H = H_0 - e\frac{i\mu}{\hbar m_e}\left[H_0, \mathbf{r}\right] \cdot \mathbf{A}(\mathbf{R}, t). \tag{2.52}$$

If we consider the eigenstate set $|\psi_i\rangle$ of the operator H_0 with energies E_i of each atomic level, forming a complete basis, we can calculate the matrix elements of the previous Hamiltonian

$$\begin{aligned}
H_{ij} &= \langle\psi_i|H|\psi_j\rangle = \langle\psi_i|H_0|\psi_j\rangle - \frac{i\mu e}{\hbar m_e}\langle\psi_i|\left[H_0, \mathbf{r}\right] \cdot \mathbf{A}(\mathbf{R}, t)|\psi_j\rangle, \\
&= E_i\delta_{ij} - \frac{i\mu e}{\hbar m_e}\langle\psi_i|(H_0\mathbf{r} - \mathbf{r}H_0)|\psi_j\rangle \cdot \mathbf{A}(\mathbf{R}, t), \\
&= E_i\delta_{ij} - \frac{i\mu e}{\hbar m_e}(\langle\psi_i|H_0\mathbf{r}|\psi_j\rangle - \langle\psi_i|\mathbf{r}H_0|\psi_j\rangle) \cdot \mathbf{A}(\mathbf{R}, t), \\
&= E_i\delta_{ij} - \frac{i\mu e}{\hbar m_e}(E_i\langle\psi_i|\mathbf{r}|\psi_j\rangle - E_j\langle\psi_i|\mathbf{r}|\psi_j\rangle) \cdot \mathbf{A}(\mathbf{R}, t), \\
&= E_i\delta_{ij} - \frac{i\mu e}{\hbar m_e}(E_i - E_j)\langle\psi_i|\mathbf{r}|\psi_j\rangle \cdot \mathbf{A}(\mathbf{R}, t), \\
&= E_i\delta_{ij} - \frac{i\mu e}{m_e}\omega_{ij}\langle\psi_i|\mathbf{r}|\psi_j\rangle \cdot \mathbf{A}(\mathbf{R}, t),
\end{aligned} \tag{2.53}$$

where we used $(E_i - E_j) = \hbar\omega_{ij}$. Recalling the relationship between the field $\mathbf{E}$ and the vector potential $\mathbf{A}$ in equation (2.4) and performing its Fourier transform

$$\begin{aligned}
\mathbf{E}(\mathbf{R}, t) &= -\frac{\partial\mathbf{A}}{\partial t} = -\frac{\partial}{\partial t}\int \tilde{\mathbf{A}}(\mathbf{R}, \omega)e^{i\omega t}d\omega, \\
&= \int_0^\infty [i\omega\tilde{\mathbf{A}}^{(+)}(\mathbf{R}, \omega)e^{-i\omega t} + i\omega\tilde{\mathbf{A}}^{(-)}(\mathbf{R}, \omega)e^{i\omega t}]d\omega,
\end{aligned} \tag{2.54}$$

and making a direct comparation with the Fourier transform of the field

$$\mathbf{E}(\mathbf{R}, t) = \int_0^\infty [\tilde{\mathbf{E}}^{(+)}(\mathbf{R}, \omega)e^{-i\omega t} + \tilde{\mathbf{E}}^{(-)}(\mathbf{R}, \omega)e^{i\omega t}]d\omega, \tag{2.55}$$

we can identify that

$$\tilde{\mathbf{E}}^{\pm} = \pm i\omega\tilde{A}^{\pm}, \tag{2.56}$$

so, returning to the Hamiltonian in equation (2.53) with this realtionship in mind

$$\begin{aligned} H_{ij} &= E_i\delta_{ij} - \frac{\mu e i\omega}{m_e}\langle\psi_i|\mathbf{r}|\psi_j\rangle \cdot \left(\int_0^\infty [\tilde{\mathbf{A}}^{(+)}e^{-i\omega t} + \tilde{\mathbf{A}}^{(-)}e^{i\omega t}]d\omega\right), \\ &= E_i\delta_{ij} + \frac{\mu e}{m_e}\langle\psi_i|\mathbf{r}|\psi_j\rangle \cdot \left(\int_0^\infty [(-i\omega)\tilde{\mathbf{A}}^{(+)}e^{-i\omega t} + (-i\omega)\tilde{\mathbf{A}}^{(-)}e^{i\omega t}]d\omega\right), \\ &= E_i\delta_{ij} + \frac{\mu e}{m_e}\langle\psi_i|\mathbf{r}|\psi_j\rangle \cdot \left(\int_0^\infty [\tilde{\mathbf{E}}^{(+)}e^{-i\omega t} + \tilde{\mathbf{E}}^{(-)}e^{i\omega t}]d\omega\right), \\ &= E_i\delta_{ij} + \frac{\mu}{m_e}\langle\psi_i|\mathbf{r}|\psi_j\rangle \cdot e\mathbf{E}(\mathbf{R},t). \end{aligned} \tag{2.57}$$

Finally, by making the aproximation that $\mu/m_e \simeq 1$, we get:

$$H_{ij} = E_i\delta_{ij} + e\mathbf{E}(\mathbf{R},t)\cdot\langle\psi_i|\mathbf{r}|\psi_j\rangle, \tag{2.58}$$

where the last term is the well-known interaction Hamiltonian between an atom and an electromagnetic field in the dipole approximation.

2.5.2 Jaynes-Cummings model

The Jaynes-Cummings model [39] is composed by two parts: the non-interacting system of the light and the atom, and their interacting part in the dipole approximation. We have already discussed the form of the Hamiltonian of a quantized field in equation (2.22). The dipole interaction part of the Hamiltonian follows from equation (2.58),

$$H_I = e\mathbf{E}(\mathbf{R},t)\cdot\langle\psi_i|\mathbf{r}|\psi_j\rangle. \tag{2.59}$$

If we consider the Hamiltonian part of the free atom and the set of j energy eigenstates $\{|\psi_j\rangle\}$ of the system, we could write it as a sum of projectors

$$H_{at} = \sum_i E_i|\psi_i\rangle\langle\psi_i|. \tag{2.60}$$

Gathering all these components together we can write the Jaynes-Cummings interaction Hamiltonian of a two level atom

$$H = H_{at} + H_{rad} + H_I = E_0|b\rangle + E_1|e\rangle + \sum_k \hbar\omega_k \left(\hat{a}^\dagger_{k,s}\hat{a}_{k,s} + \frac{1}{2}\right) + e\mathbf{E}\cdot\mathbf{r}, \tag{2.61}$$

with kets $|b\rangle$ and $|e\rangle$ for the ground and excited states respectively. The set $\{|e\rangle, |b\rangle\}$ is a complete basis, so we can express the operator $\mathbf{r}$ as

$$\begin{aligned}\mathbf{r} = \hat{\mathbb{1}}\,\mathbf{r}\,\hat{\mathbb{1}} &= \sum_i |i\rangle\langle i|\,\mathbf{r}\,\sum_j |j\rangle\langle j|,\\ &= (|e\rangle\langle e| + |b\rangle\langle b|)\,\mathbf{r}\,(|e\rangle\langle e| + |b\rangle\langle b|),\\ &= |e\rangle\langle e|\mathbf{r}|e\rangle\langle e| + |b\rangle\langle b|\mathbf{r}|e\rangle\langle e| + |e\rangle\langle e|\mathbf{r}|b\rangle\langle b| + |b\rangle\langle b|\mathbf{r}|b\rangle\langle b|,\end{aligned} \tag{2.62}$$

where the first and the last terms are zero because atoms do not have permanent dipolar moments and thus $\langle b|\mathbf{r}|b\rangle = \langle e|\mathbf{r}|e\rangle = 0$. Then

$$\begin{aligned}\mathbf{r} &= |b\rangle\langle b|\mathbf{r}|e\rangle\langle e| + |e\rangle\langle e|\mathbf{r}|b\rangle\langle b|,\\ &= \mathbf{r}_{be}|b\rangle\langle e| + \mathbf{r}_{eb}|e\rangle\langle b|,\\ &= \mathbf{r}_{be}\hat{\sigma}_{eb} + \mathbf{r}_{eb}\hat{\sigma}_{be},\\ &= \mathbf{r}_{be}\hat{\sigma}^- + \mathbf{r}_{eb}\hat{\sigma}^+,\end{aligned} \tag{2.63}$$

where $\sigma^- = \sigma_{eb} = |b\rangle\langle e|$, $\sigma^+ = \sigma_{be} = |e\rangle\langle b|$ are the atomic ladder operators and $\mathbf{r}_{be}, \mathbf{r}_{eb}$, the dipole matrix element corresponding to the transition from the state $|e\rangle$ to the state $|b\rangle$ and from $|b\rangle$ to the state $|e\rangle$, respectively.

2.5.3 Rotating-wave approximation

Using the Jaynes-Cummings model in the interaction picture, the time evolution of the atomic operators σ have two temporal dependencies: an oscillation proportional to the sum of frequencies and another proportional to the difference. In the rotating-wave approximation, we neglect the sum terms by the following argument:

The interaction Hamiltonian of a two level atom and a single mode of a quantized field in the dipole approximation is:

$$H_I = e\mathbf{r}\cdot\mathbf{E}, \tag{2.64}$$

substituting equations (2.63) and (2.23),

$$\begin{aligned} H_I &= e(\mathbf{r}_{be}\hat{\sigma}^- + \mathbf{r}_{eb}\hat{\sigma}^+)\cdot\mathbf{E}_0(\hat{a}^\dagger + \hat{a}), \\ &= e\{(\mathbf{r}_{be}\cdot\mathbf{E}_0)\hat{\sigma}^-\hat{a}^\dagger + (\mathbf{r}_{be}\cdot\mathbf{E}_0)\hat{\sigma}^-\hat{a} + (\mathbf{r}_{eb}\cdot\mathbf{E}_0)\hat{\sigma}^+\hat{a}^\dagger + (\mathbf{r}_{eb}\cdot\mathbf{E}_0)\hat{\sigma}^+\hat{a}\}, \end{aligned} \tag{2.65}$$

where we have four terms. Considering the creation and annihilation operators in the interaction picture

$$\hat{a}(t) = \hat{a}(0)e^{-i\omega_r t}, \qquad \hat{a}^\dagger(t) = \hat{a}^\dagger(0)e^{i\omega_r t}, \qquad \hat{\sigma}^\pm(t) = \hat{\sigma}^\pm(0)e^{\pm i\omega_a t}, \tag{2.66}$$

where ω_r is the frequency of the radiation fields and ω_a the frequency of the energetic difference between the atomic level e and b. Checking the time dependence of the terms in the interaction Hamiltonian

$$\begin{aligned} H_I = \{&(\mathbf{r}_{be}\cdot\mathbf{E}_0)\hat{\sigma}^-\hat{a}^\dagger e^{it(\omega_r-\omega_a)} + (\mathbf{r}_{be}\cdot\mathbf{E}_0)\hat{\sigma}^-\hat{a}e^{-it(\omega_r+\omega_a)} \\ &+ (\mathbf{r}_{eb}\cdot\mathbf{E}_0)\hat{\sigma}^+\hat{a}^\dagger e^{it(\omega_r+\omega_a)} + (\mathbf{r}_{eb}\cdot\mathbf{E}_0)\hat{\sigma}^+\hat{a}e^{-it(\omega_r-\omega_a)}\}, \end{aligned} \tag{2.67}$$

where the first and last terms have an oscillation proportional to the difference of frequency between ω_a and ω_r, while the second and third terms oscillate proportionally to the sum of those frequencies. Those second and third terms are known as the *rapidly oscillating terms* and are neglected because if we do a time average they will reduce to zero. So we only keep the terms with an oscillation proportional to the frequency difference

$$H_I = \{(\mathbf{r}_{be}\cdot\mathbf{E}_0)\hat{\sigma}^-\hat{a}^\dagger e^{it(\omega_r-\omega_a)} + (\mathbf{r}_{eb}\cdot\mathbf{E}_0)\hat{\sigma}^+\hat{a}e^{-it(\omega_r-\omega_a)}\}. \tag{2.68}$$

This is called the *rotating-wave approximation* and is valid for *low* intensities and near-resonance frequencies ($\omega_a \sim \omega_r$).

2.5.4 Density matrix

The density matrix or density operator of a quantum system is defined in general as

$$\rho = \sum_j p_j |\psi_j\rangle\langle\psi_j|, \tag{2.69}$$

where p_j are non-negative coefficients and $\{|\psi_j\rangle\}$ is the basis set of that system. The time evolution of the density matrix is calculated by applying the Schrödinger equation

$$\begin{aligned}
\frac{\partial\rho}{\partial t} &= \frac{\partial}{\partial t}\left(\sum_j p_j|\psi_j\rangle\langle\psi_j|\right), \\
&= \sum_j p_j\left(\frac{\partial|\psi_j\rangle}{\partial t}\langle\psi_j| + |\psi_j\rangle\frac{\partial\langle\psi_j|}{\partial t}\right), \\
&= \frac{1}{i\hbar}\sum_j p_j\left(H|\psi_j\rangle\langle\psi_j| - |\psi_j\rangle\langle\psi_j|H\right), \\
&= \frac{1}{i\hbar}H\left(\sum_j p_j|\psi_j\rangle\langle\psi_j|\right) - \left(\sum_j p_j|\psi_j\rangle\langle\psi_j|\right)H, \\
&= \frac{1}{i\hbar}H\rho - \rho H, \\
&= \frac{1}{i\hbar}[H,\rho].
\end{aligned} \tag{2.70}$$

The density operator is useful to calculate expectation values of operators $\mathcal{O}$ since

$$\begin{aligned}
\langle\mathcal{O}\rangle = \sum_i\langle\psi_i|\mathcal{O}|\psi_i\rangle = \sum_i\sum_j\langle\psi_i|\mathcal{O}|\psi_j\rangle\langle\psi_j|\psi_i\rangle = \sum_i\sum_j\langle\psi_j|\psi_i\rangle\langle\psi_i|\mathcal{O}|\psi_j\rangle, \\
= Tr(\sum_i|\psi_i\rangle\langle\psi_i|\mathcal{O}) = Tr(\rho\mathcal{O}).
\end{aligned} \tag{2.71}$$

The density matrix has encoded all the information about a quantum system. It is useful for describing mixed states, that cannot be described by a single ket. In our case, it is handy for describing a system of more than two levels. So, by finding the evolution of the density matrix, we could calculate the time evolution of operators in the system and their expected values.

2.5.5 Spontaneous decay and the Lindblad equation

The next ingredient we need to add to our model is the spontaneous emission phenomenon. It cannot be described in closed quantum systems. We need to incorporate dissipation into our model.

We could model the decay by considering that our two level atom is a damped harmonic oscilator surrounded by a reservoir of many modes of a radiation field. By analyzing this system we can deduce the *master equation* [41]

$$\dot{\rho} = \frac{1}{i\hbar}[H, \rho] + \sum_{ij} \frac{\gamma_{ij}}{2}(2A_{ji}\rho A_{ij} - A_{ji}A_{ij}\rho + \rho A_{ji}A_{ij}), \tag{2.72}$$

where H is the Hamiltonian of the system, A_{ij} the ladder operators. For a two level atom the master equation is [41]:

$$\begin{aligned} \dot{\rho} &= \frac{-i}{2}\omega_A[\sigma_z, \rho] + \frac{\gamma}{2}(2\sigma_-\rho\sigma_+ - \sigma_-\sigma_+\rho + \rho\sigma_-\sigma_+), \\ &= \frac{-i}{2}\omega_A[\sigma_z, \rho] + \hat{L}(\rho), \end{aligned} \tag{2.73}$$

where γ is the decay rate of the excited level and $\hat{L}$ is the Lindblad operator term. This model includes the *Born-Markov approximation* in its deduction. This approximation reads that the evolution of the density matrix depends only on its present states and not on its past history, as discussed in [41].

If we add the Lindblad term to the Jaynes-cummings model, we have the complete description of the two-level atom interacting with an electromagnetic field with spontaneous decay.

The models discussed in this section can be extended to atoms with more levels: for the atomic part in the Hamiltonian, we have to list all the relevant levels, and in the interaction section, we have to consider a dipolar term for each dipole transition allowed between those levels, and we add a Lindblad term for each spontaneous decay. In the

following section we will use this model to describe a four-level atoms dynamics where our FWM process occurs.

2.6 Four-level atom

Now that we have built the master equation for a two-level atom we continue to consider our system with four levels. For the FWM process we send two pump beams in our experimental system that couple the base state $|0\rangle$ to the intermediate level $|1\rangle$ and then to level $|2\rangle$, as described in Figure 2.2. Of all the possible decay paths that the atoms can take, we focus on atoms decaying to level $|3\rangle$ and then to the state $|0\rangle$ by emitting a photon pair.

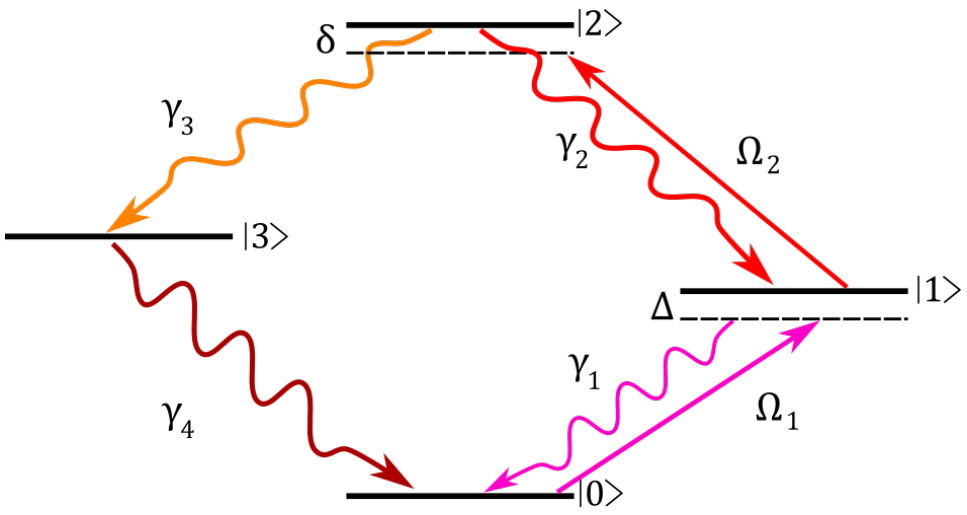

Figure 2.2: Schematics diagram of a four-level atom in a diamond configuration. The pumping beams are represented with straight lines and the meandering curves show the possible decays. Ω_1, Ω_2 stand for the Rabi frequencies of each laser, Δ and δ their detuning and γ_i the correspondent decay rate of each level.

According to the Jaynes-Cunnings model and all the details we discussed in section 2.5.2, we can write the Hamiltonian for our four-level system as:

$$H = H_{at} + H_{rad} + H_I, \tag{2.74}$$

where the free atomic Hamiltonian is the sum of the projectors of each level multiplied by their energies $E_i = \hbar\omega_i$,

$$H_{at} = \sum_i \hbar\omega_i |i\rangle\langle i| = \sum_i \hbar\omega_i \sigma_{ii}, \tag{2.75}$$

where i runs from 0 to 3 and $\sigma_{ij} = |i\rangle\langle j|$. The radiation part is given by

$$H_{rad} = \sum_k \hbar\omega_k \left(\hat{a}_k^\dagger \hat{a}_k + \frac{1}{2}\right), \tag{2.76}$$

and finally the interaction Hamiltonian

$$H_I = e\mathbf{r}\cdot\mathbf{E}_{p1} + e\mathbf{r}\cdot\mathbf{E}_{p2}, \tag{2.77}$$

is the sum of the dipole term for each pump laser. We can model each laser in a semiclassical way, just like equation (2.33). So

$$e\mathbf{r}\cdot\mathbf{E}_1 + e\mathbf{r}\cdot\mathbf{E}_2 = \Omega_{01}(\sigma_{01}e^{-i\omega_{p1}t} + \sigma_{10}e^{i\omega_{p1}t}) + \Omega_{12}(\sigma_{12}e^{-i\omega_{p2}t} + \sigma_{21}e^{i\omega_{p2}t}), \tag{2.78}$$

where we use the definition

$$\Omega_{ij} = \frac{\mathbf{d}_{ij}\cdot\mathbf{E}_{pi}}{\hbar}, \tag{2.79}$$

and $\mathbf{d} = e\mathbf{r}$. Here, we have to make an important note regarding the polarization of the pumping light. Due to the vectorial character of this dot product, the Rabi frequency Ω_{ij} depends on the direction of the electrical field that interacts with the dipole $\mathbf{d}_{ij}$. In other words, the polarization of the beam. In the section 2.7 the selection of the quantization axis of our system is discussed.

So far our four-level Hamiltonian is

$$H = \sum_i \hbar\omega_i\sigma_{ii} + \sum_k \hbar\omega_k\left(\hat{a}_k^\dagger\hat{a}_k + \frac{1}{2}\right) + \Omega_{01}(\sigma_{01}e^{-i\omega_{p1}t} + \sigma_{10}e^{i\omega_{p1}t}) \\ +\Omega_{12}(\sigma_{12}e^{-i\omega_{p2}t} + \sigma_{21}e^{i\omega_{p2}t}). \tag{2.80}$$

To eliminate the explicit time-dependence in the exponential terms, we make a unitary transformation U to the so-called *Rotating frame*,

$$U = \sum_{j=1}^{3} e^{-i\omega_j t}|j\rangle\langle j|. \tag{2.81}$$

Here the oscillating terms of the Hamiltonian are transformed into differences of frequency, in the form

$$H = \hbar\Delta\sigma_{11} + \hbar\delta\sigma_{22} + \sum_k \hbar\omega_k\left(\hat{a}_k^\dagger\hat{a}_k + \frac{1}{2}\right) + \Omega_{01}(\sigma_{01} + \sigma_{10}) + \Omega_{12}(\sigma_{12} + \sigma_{21}), \tag{2.82}$$

where $\Delta = \omega_{01} - \omega_{p1}$ and $\delta = \omega_{12} - \omega_{p2}$ are the differences between transition and beam frequencies. The master equation for our system is, according to equation (2.72)

$$\dot{\rho} = \frac{1}{i\hbar}[H, \rho] + \hat{L}_1(\rho) + \hat{L}_2(\rho) + \hat{L}_3(\rho) + \hat{L}_4(\rho), \tag{2.83}$$

which includes a Lindblad term for each decay. Calculating the matrix elements of this master equation $\langle j|\dot{\rho}|i\rangle$, where $i, j = 0, 1, 2, 3$ we have a system of 16 differential equations. This linear system can be numerically solved to obtain the evolution of each term of the density matrix.

2.6.1 Numerical Solution

In this subsection a basic structure is described of how to solve numerically the master equation (2.83) of a four-level atom. Since we have a four-level atomic system, the density matrix has $4 \times 4 = 16$ complex terms. However, we can use some properties

of the density matrix to simplify this problem. Consider the hermiticity of the density matrix

$$\rho^\dagger = \rho. \tag{2.84}$$

In other words $\rho_{ij} = \rho^*_{ji}$, which means that the non-diagonal elements are not independent among each other and that the diagonal terms ρ_{ii} are real. Also,

$$\sum_j \rho_{jj} = 1, \tag{2.85}$$

reduces the system of equations and, we can rearrange it into a matrix form $\dot{\mathbf{V}} = \mathcal{M}\mathbf{V}$.

Appendix A includes the matrix $\mathcal{M}$ explicitly, along with the code to solve numerically the system of equations for our case. Solving it gives us the temporal evolution of the density matrix. A natural question arises here: how can we associate the experimental data and these results? The key, at least for the second-order cross-correlation function, is the following.

Let us consider the $G^{(2)}_{SI}$ cross-correlation function, as defined in equation (2.29), where we focus on detecting the signal $\hat{E}_s$ at the time t and idler photons $\hat{E}_i$ at the time $t + \Delta t$ that are produced by the FWM process where both are quantized fields with the form given by equation (2.35). Thus we obtain:

$$\begin{aligned}
G^{(2)}_{SI}(t, t+\Delta t) &= \langle i| \left(\frac{-i}{L^{3/2}} \sum_k \left(\frac{\hbar\omega}{2\epsilon_0}\right) \hat{a}^\dagger_k(t) \boldsymbol{\epsilon}_k e^{-i\boldsymbol{k}\cdot\boldsymbol{r}}\right) \left(\frac{-i}{L^{3/2}} \sum_k \left(\frac{\hbar\omega}{2\epsilon_0}\right) \hat{a}^\dagger_k(t+\Delta t) \boldsymbol{\epsilon}_k e^{-i\boldsymbol{k}\cdot\boldsymbol{r}}\right) \\
&\quad \left(\frac{i}{L^{3/2}} \sum_k \left(\frac{\hbar\omega}{2\epsilon_0}\right) \hat{a}_k(t+\Delta t) \boldsymbol{\epsilon}_k e^{-i\boldsymbol{k}\cdot\boldsymbol{r}}\right) \left(\frac{i}{L^{3/2}} \sum_k \left(\frac{\hbar\omega}{2\epsilon_0}\right) \hat{a}_k(t) \boldsymbol{\epsilon}_k e^{-i\boldsymbol{k}\cdot\boldsymbol{r}}\right) |j\rangle, \\
&= \langle i| \left(\frac{-i}{L^{3/2}} \left(\frac{\hbar\omega}{2\epsilon_0}\right) \hat{a}^\dagger_s(t) \boldsymbol{\epsilon}_s e^{-i\boldsymbol{k}\cdot\boldsymbol{r}}\right) \left(\frac{-i}{L^{3/2}} \left(\frac{\hbar\omega}{2\epsilon_0}\right) \hat{a}^\dagger_i(t+\Delta t) \boldsymbol{\epsilon}_i e^{-i\boldsymbol{k}\cdot\boldsymbol{r}}\right) \\
&\quad \left(\frac{i}{L^{3/2}} \sum_k \left(\frac{\hbar\omega}{2\epsilon_0}\right) \hat{a}_i(t+\Delta t) \boldsymbol{\epsilon}_i e^{i\boldsymbol{k}\cdot\boldsymbol{r}}\right) \left(\frac{i}{L^{3/2}} \left(\frac{\hbar\omega}{2\epsilon_0}\right) \hat{a}_s(t) \boldsymbol{\epsilon}_s e^{i\boldsymbol{k}\cdot\boldsymbol{r}}\right) |j\rangle, \\
&\propto \langle i| \hat{a}^\dagger_s(t) \hat{a}^\dagger_i(t+\Delta t) \hat{a}_i(t+\Delta t) \hat{a}_s(t) |j\rangle,
\end{aligned} \tag{2.86}$$

where from step one to step two we remove the sum of modes because we experimentally filter all the frequencies and detect only the signal and idler photons. Finally we conclude that the correlation function $G^{(2)}_{SI}$ is proportional to the expectation value of the annihilator and creation operators. This correlation function is also proportional to the atomic operators [42]

$$G^{(2)}_{SI}(t, t+\Delta t) = f(\mathbf{r})^2 \langle \hat{\sigma}_{32}(t)\hat{\sigma}_{03}(t+\Delta t)\hat{\sigma}_{30}(t+\Delta t)\hat{\sigma}_{23}(t)\rangle, \tag{2.87}$$

where $f(\mathbf{r})$ is a geometrical factor. The atomic operators $\hat{\sigma}_{32}$ and $\hat{\sigma}_{03}$ correspond to the radiation operators $\hat{a}_s$ and $\hat{a}_i$, respectively. The important part of the last equation lies into the proportionality between both expectation values. By normalizing equations (2.86) and (2.87) we may focus only in the temporal behavior. Taking the expectation value proportional to $G^{(2)}_{SI}$ in terms of the atomic operators

$$\begin{aligned} G^{(2)}_{SI}(t, t+\Delta t) &\propto \langle \hat{\sigma}_{32}(t)\hat{\sigma}_{03}(t+\Delta t)\hat{\sigma}_{30}(t+\Delta t)\hat{\sigma}_{23}(t)\rangle, \\ &= Tr[\hat{\sigma}_{32}(t)\hat{\sigma}_{03}(t+\Delta t)\hat{\sigma}_{30}(t+\Delta t)\hat{\sigma}_{23}(t)\rho(t_0)], \\ &= Tr[\hat{\sigma}_{03}(t+\Delta t)\hat{\sigma}_{30}(t+\Delta t)\hat{\sigma}_{23}(t)\rho(t_0)\hat{\sigma}_{32}(t)], \end{aligned} \tag{2.88}$$

and then, using the evolution operator $\hat{U}$ that follows $\hat{A}(t) = \hat{U}^{-1}(t, t_0)\hat{A}(t_0)\hat{U}(t, t_0)$ for any given operator $\hat{A}$, the right side of equation (2.88) is

$$\begin{aligned} &Tr[\hat{U}(t+\Delta t, t_0)\hat{\sigma}_{03}(t_0)\hat{U}^{-1}(t+\Delta t, t_0)\hat{U}(t+\Delta t, t_0)\hat{\sigma}_{30}(t_0)\hat{U}^{-1}(t+\Delta t, t_0) \\ &\qquad \hat{U}^{-1}(t, t_0)\hat{\sigma}_{23}(t_0)\hat{U}(t, t_0)\rho(t_0)\hat{U}^{-1}(t, t_0)\hat{\sigma}_{32}(t_0)\hat{U}(t, t_0)], \\ = &Tr[\hat{U}(t+\Delta t, t_0)\hat{\sigma}_{03}(t_0)\hat{\sigma}_{30}(t_0)\hat{U}^{-1}(t+\Delta t, t_0)\hat{U}^{-1}(t, t_0)\hat{\sigma}_{23}(t_0)\hat{U}(t, t_0)\rho(t_0) \\ &\qquad \hat{U}^{-1}(t, t_0)\hat{\sigma}_{32}(t_0)\hat{U}(t, t_0)], \end{aligned} \tag{2.89}$$

where

$$\hat{\sigma}_{23}(t_0)\hat{U}(t, t_0)\rho(t_0)\hat{U}^{-1}(t, t_0)\hat{\sigma}_{32}(t_0) = \hat{\sigma}_{23}(t_0)\rho(t)\hat{\sigma}_{32}(t_0) = |3\rangle\langle 2|\rho(t)|2\rangle\langle 3| = \rho_{22}(t)|3\rangle\langle 3|. \tag{2.90}$$

So, substituting in equation (2.89)

$$\begin{aligned}
&\rho_{22}(t)Tr[\hat{U}(t+\Delta t,t_0)\hat{\sigma}_{03}(t_0)\hat{\sigma}_{30}(t_0)\hat{U}^{-1}(t+\Delta t,t_0)\hat{U}^{-1}(t,t_0)|3\rangle\langle 3|\hat{U}(t,t_0)],\\
&=\rho_{22}(t)Tr[\hat{U}(t+\Delta t,t_0)|3\rangle\langle 3|\hat{U}^{-1}(t+\Delta t,t_0)\hat{U}^{-1}(t,t_0)|3\rangle\langle 3|\hat{U}(t,t_0)],\\
&=\rho_{22}(t)Tr[\hat{U}(t,t_0)\hat{U}(t+\Delta t,t_0)|3\rangle\langle 3|\hat{U}^{-1}(t+\Delta t,t_0)\hat{U}^{-1}(t,t_0)|3\rangle\langle 3|],\\
&=\rho_{22}(t)Tr[\hat{U}(t+\Delta t,t)|3\rangle\langle 3|\hat{U}^{-1}(t+\Delta t,t)|3\rangle\langle 3|],\\
&=\rho_{22}(t)\rho'_{33}(t+\Delta t),
\end{aligned} \tag{2.91}$$

where we consider the condition of $\rho'_{33}(t+\Delta t)=1$ when $\Delta t=0$ meaning that all the population of atoms at time $\Delta t=0$ is in the state $|3\rangle$. So, summarizing everything we have

$$G^{(2)}_{SI}(t,t+\Delta t)\propto\rho_{22}(t)\rho'_{33}(t+\Delta t), \tag{2.92}$$

where the terms ρ_{22} and ρ'_{33} are the population of the levels $|2\rangle$ and $|3\rangle$ respectively. With this result, we have a direct connection between the cross-correlation function and terms of the density matrix that is very useful to compare the numerical simulation with the experimental data. The numerical simulation results, along with a comparison with our experimental data are given in section 5.

2.7 Introducing the experimental conditions

Recalling the equation (2.79) of the Rabi frequency of an atomic transition from a level $|g\rangle$ to a level $|e\rangle$ and, considering spherical coordinates in terms of the Cartesian basis

$$\begin{aligned}
\hat{e}_{\pm}&=\mp\frac{1}{\sqrt{2}}(\hat{x}\pm i\hat{y}),\\
\hat{e}_0&=\hat{z},
\end{aligned} \tag{2.93}$$

so we can describe any given vector $\hat{A}$ as

$$\hat{A} = \sum_{q=-1}^{1} A_q \hat{e}_q. \tag{2.94}$$

where q is an index that runs from -1 to 1. In this basis the electric field $\hat{E}$ is

$$\begin{aligned} E_z &= E_0, \\ E_x &= -\frac{1}{\sqrt{2}}(E_{+1} - E_{-1}), \\ E_y &= \frac{i}{\sqrt{2}}(E_{+1} + E_{-1}). \end{aligned} \tag{2.95}$$

For our experiment, we chose $\hat{y}$ as the quantization axis and the propagation of our beam is in the $\hat{z}$ direction, as illustrated by the diagram in Figure 2.3. We select this direction because the coils generate a magnetic gradient two times stronger in the $\hat{y}$ direction, representing a preferential direction. It is worth noting that this is just a convention used for simplicity in the calculations; if we select any other direction to be our quantization axis, the calculations would be totally equivalent. Given this selection, the index q in equation (2.94) represent π polarization for $q = 0$ and $\sigma^{\pm}$ polarization for $q = \pm 1$

We choose that the pump $p1$ has linear polarization in the $\hat{x}$ direction and $p2$ is also linear, in the $\hat{y}$ direction. Given the convention of Figure 2.3, the Rabi frequency can be expressed as

$$\Omega_{ij} = \frac{eE_0}{\hbar}\langle i|\hat{r}\cdot\hat{e}|j\rangle = \frac{eE_0}{\hbar}\langle i|\sum_{q=-1}^{1}\hat{e}_q r_q|j\rangle. \tag{2.96}$$

We have to consider that each state $|i\rangle$ and $|j\rangle$ has its corresponding quantum numbers: n, L, s, J, F, m. It is well known that one can separate the geometrical part of angular momentum using the Wigner-Eckart theorem, resulting in

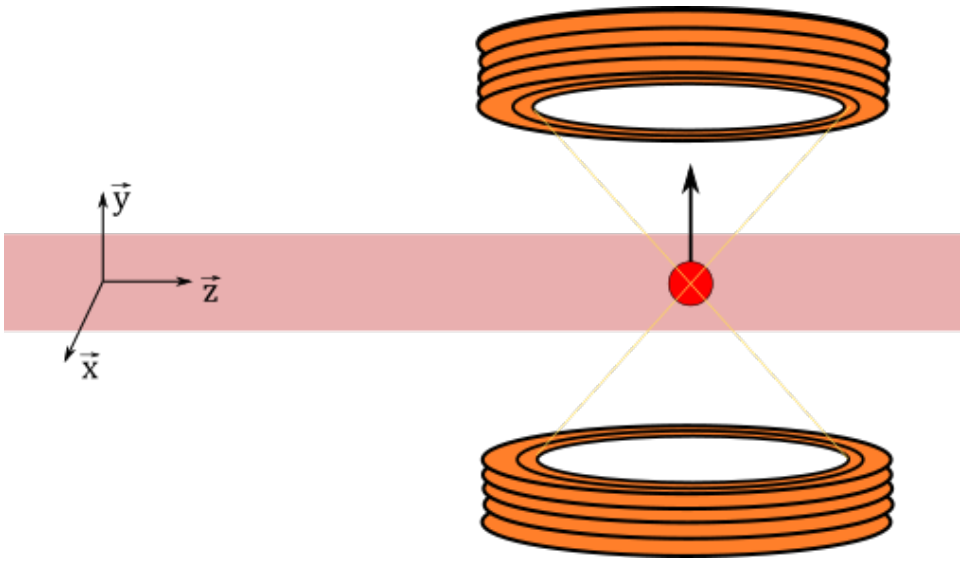

Figure 2.3: Schematics of the quantization axis in our experimental setup. The figure shows that the pump beams are propagating in the $\hat{z}$ direction and we define the quantization axis in the same direction of the magnetic gradient, $\hat{y}$ direction. The figure is not to scale.

$$\Omega_{e,g} = \frac{eE_0}{\hbar}(-1)^{F-m}\sum_{q=-1}^{1}\begin{pmatrix} F & 1 & F' \\ -m & q & m' \end{pmatrix}(-1)^{J+I+F'+1}\sqrt{(2F+1)(2F'+1)} \times \begin{Bmatrix} J & I & F \\ F' & 1 & J' \end{Bmatrix}\langle n', j'||\hat{r}||n, j\rangle, \tag{2.97}$$

where the expectaion value $\langle n', j'||\hat{r}||n, j\rangle$ only depends on the radial parts of the wave functions, also known as the radial dipole matrix element. This is a well known value that we can consult in the literature [43], it has been measured experimentally and calculated for Rubidium transitions. The other terms in equation (2.97) have a geometrical dependence that can be calculated using the 3-j and 6-j Wigner symbols, where we need the quantum numbers of the initial and final state, denoted by F, m and F', m' respectively. The q of each pumping beam can be determined by their polarization direction. The $p1$ beam has linear polarization in the $\hat{x}$ direction, we have to consider $q = -1, 1$

and for $p2$ light polatization linear in the $\hat{y}$ direction means that we only have to consider the term $q = 0$.

Figure 2.4 presents a schematics of the relevant hyperfine levels for our FWM process. Those are the levels employed for the calculations of the Rabi frequencies in Appendix B. Each of them has a number of Zeeman sublevels following the rule $m = -F, -F + 1, ..., 0, F - 1, F$.

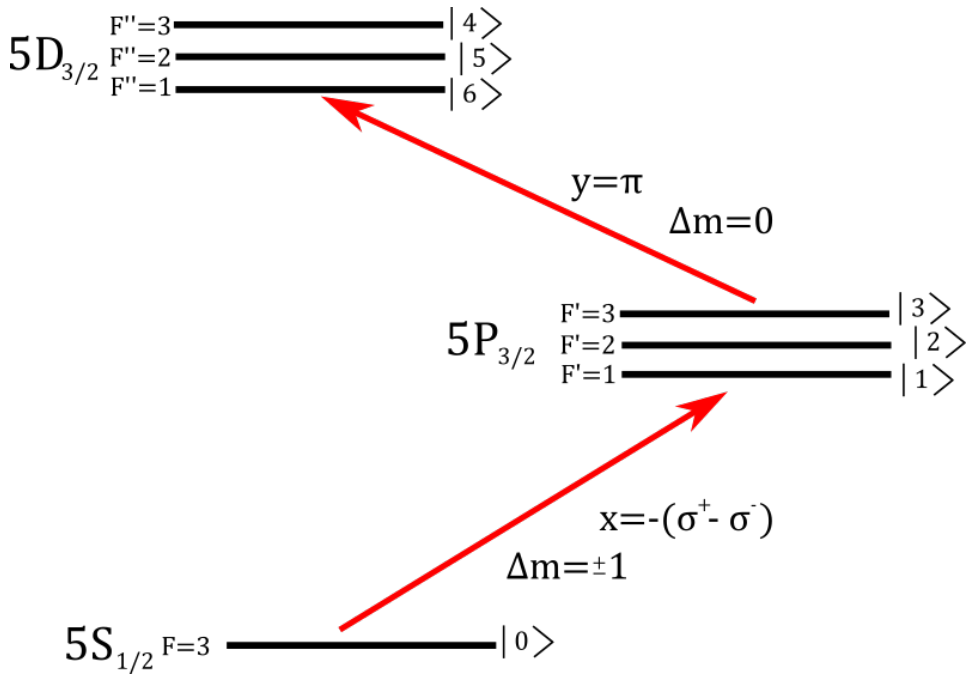

Figure 2.4: Relevant hyperfine levels for the pumping in the FWM process. We indicate the polarization of each beam in Cartesian and spherical coordinates, along with the change of the magnetic quantum number Δm that each beam produce.

When we calculate the total Rabi frequency of each pumping beam, we should consider all the possible combinations of excited levels. From the ground state $5S_{1/2}$ to the intermediate state $5P_{3/2}$ and then to the excited state $5D_{3/2}$. Then we add each case to the corresponding Rabi frequency. Tables in Appendix B displays our results for the geometrical part of equation (2.97).

Chapter 3

Experimental setup

Our experimental setup generates near-infrared photon pairs with a FWM process in cold Rubidium atoms. We use cold atoms because the reduction in thermal noise can help us to demonstrate quantum information principles and protocols. This chapter gives a description of each part of the experimental setup as well as how our measurements are performed.

3.1 Laser system

To achieve the atomic excitations requiered for magneto-optical trapping and to induce a four-wave mixing process, we need to generate laser light with the correct frequency and bandwidth. For the MOT, we also need to amplify it to a suitable power of around 200 mW. Finally, we need to distribute the light of each laser to the required part of the experiment. First we describe the properties of the light needed for laser cooling and then for the FWM.

3.1.1 Frequencies for laser cooling

For our purpose the advantages of using cold instead of room temperature or hot atoms are that we can achieve higher spectral brightness (a parameter discussed later in section 4.2.2) and increase the signal to noise ratio.

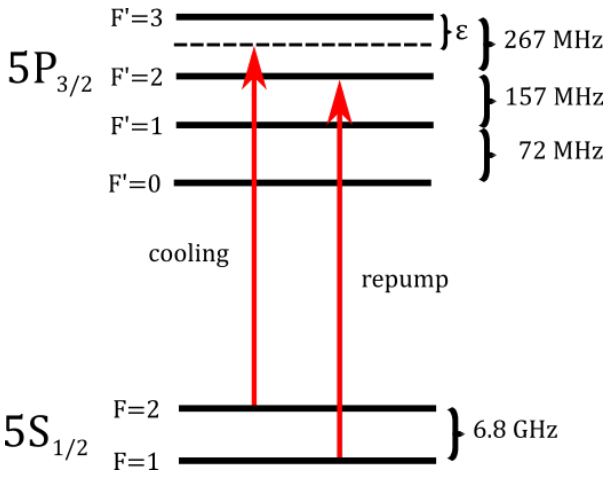

Figure 3.1: Hyperfine levels of the D_2 transition of Rubidium 87. To close the cycle transiton $5S_{1/2}F = 2 \rightarrow 5P_{3/2}F' = 3$ we need to add a repump beam for the $5S_{1/2}F = 1 \rightarrow 5P_{3/2}F' = 2$.

For laser cooling we need a closed cycle, where our atoms remain absorbing the cooling beam and emitting spontaneously. Each absorption and emission will reduce their speed because the cooling beam is red-detuned dozens of MHz [27]. We achieve this by using the D_2 line transition $5S_{1/2}F = 2 \rightarrow 5P_{3/2}F' = 3$, indicated in Figure 3.1. From selection rules of dipolar transitions we know that the excited atoms in the level $5P_{3/2}F' = 3$ could only decay to the $F = 2$, giving us a cyclic transition. However we have a leakage of atoms populating the $5S_{1/2}, F = 1$ state via non-resonant excitation of the $5S_{1/2}, F = 2 \rightarrow 5P_{3/2}, F' = 2$ transition. To eliminate this leak and return the atoms to the cooling cycle, we incorporate a *repump* laser resonant to the $5S_{1/2}F = 1 \rightarrow 5P_{3/2}F' = 2$ transition.

3.1.2 Frequencies required for FWM

Figure 3.2 indicates the energy levels for the FWM process. We need light to excite the $5S_{1/2}, F = 2 \rightarrow 5P_{3/2}, F' = 3$ transition, the $5P_{3/2}, F = 3 \rightarrow 5D_{3/2}, F'' = 3$ transition

and a seed beam, resonant the $5S_{1/2}, F = 2 \rightarrow 5P_{1/2}, F' = 2$ transition. They are indicated in Figure 3.2 with straight lines.

The $p1$ beam needs to be tenths of MHz away from the resonant transition $5S_{1/2}F = 2 \rightarrow 5P_{3/2}F' = 3$ because we do not want to populate the state $5P_{3/2}$. We call this detuning Δ. The $p2$ beam should compensate Δ and also have the freedom to be tuned a few MHz around the $5D_{3/2}, F'' = 3$ level, indicated with δ. We show both detunings in Figure 3.2. The seed beam will be resonant with the transition $5S_{1/2}F = 2 \rightarrow 5P_{1/2}F' = 2$. The power needed in each case are: the $p1$ beam needs from 100 to 100 μW. The $p2$ beam, from 3 to 8 mW. The *seed* beam power needs 5 mW.

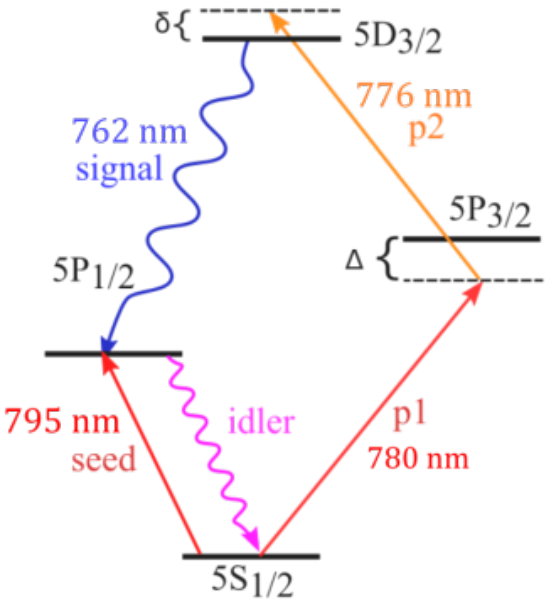

Figure 3.2: Schematics of the four wave mixing process in atomic Rubidium 87 implemented in our experiments. The straight lines represent the pumping beams, while the meandering curves depict signal and idler photons. Δ is the diference between the frequency of the transition $5S_{1/2}F = 2 \rightarrow 5P_{3/2}F' = 3$ and $p1$, while δ is the diference between transition $5P_{3/2}F' = 3 \rightarrow 5D_{3/2}F'' = 3$ and $p2$.

3.2 Laser light generation and stabilization

The atom that we use is the isotope 87 of Rubidium which has well-known D transitions [43] useful for laser cooling. One of the main advantages of using Rubidium is that the cooling transitions are in the near-infrared spectrum, making them accesible with extended cavity diode lasers.

We use extended cavity diode lasers (ECDL) to generate light for our experiments. These are highly reliable and low-cost lasers, available in the near-infrared region of the electromagnetic spectrum. They have a bandwidth of less than 250 kHz, enough for the light to interact with rubidium atoms. We use high-resolution spectroscopy to lock each laser to the cooling, repump, $p1$, $p2$ and seed transitions, respectively.

Our main optical reference is the *master laser*, Figure 3.3. This is a single-mode laser using the Cateye configuration (MOGLabs model CEL002), with around 150 kHz bandwidth. We lock the laser to the C13 crossover using a saturated Doppler-free absorption spectroscopy setup, that is -211.8 MHz away from the $5S_{1/2}F = 2 \rightarrow 5P_{3/2}F' = 3$ transition [44]. It can produce approximately 60 mW of experimentally useful light, divided as follows (see Figure 3.3):

- The first step of the two-photon spectroscopy of the pump laser $p2$
- The input of a tapered amplifier
- Optical pumping $p1$

The *repump* laser is a home-made, ECDL in Littrow configuration [45]. We use a polarization spectroscopy array to lock it to the $5S_{1/2}, F = 1 \rightarrow 5P_{3/2}, F' = 2$ transition [46]. After the spectroscopy, we have around 30 mW of experimentally-useful light, which is enough for saturating the atom number in the trap.

The *seed* laser with light of 795 nm has a polarization spectroscopy array to lock its frequency to the $5S_{1/2}, F = 2 \rightarrow 5P_{1/2}, F' = 2$. This light its not present during experiments. However it is very useful for alignment purposes, indicated in section 3.4.

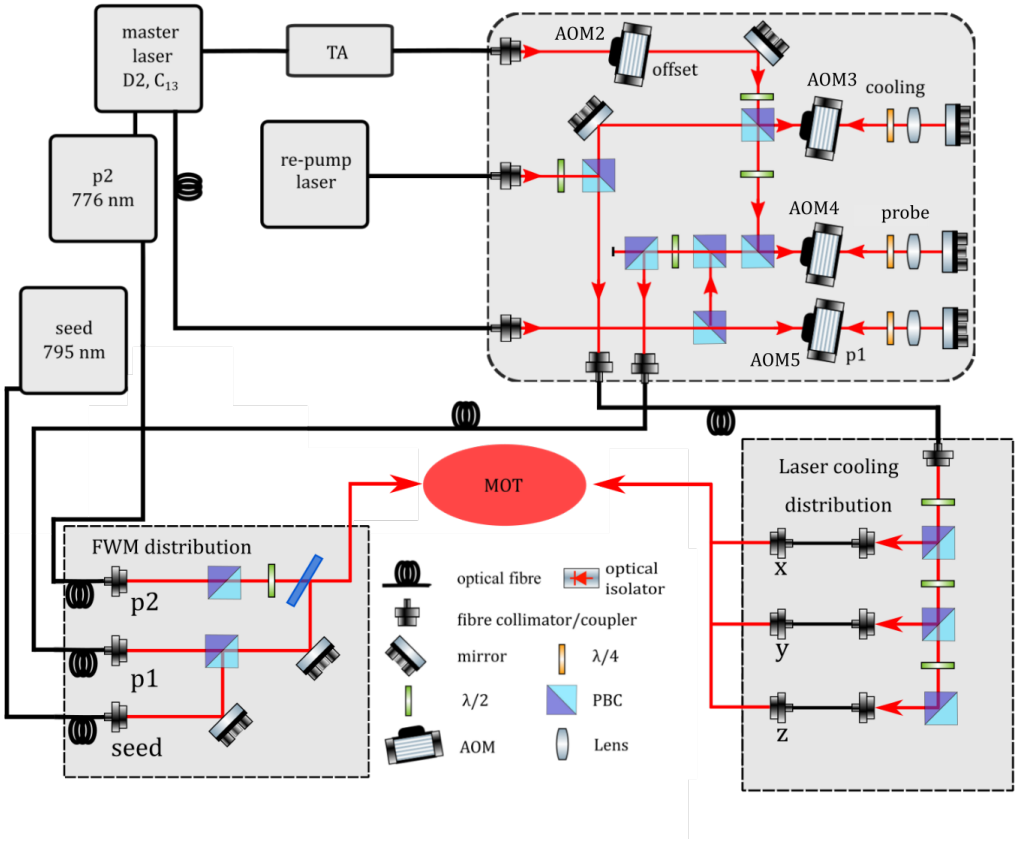

Figure 3.3: Block diagram of light distribution from the preparation boards to the science chamber. Blocks with dashed borders represent the fine-tuning and distribution arrays and straight-line borders.

Figure 3.3 shows a schematics of our laser system. Frequency preparation boards are represented by gray boxes with straight borders and the light distribution arrays are displayed with dotted borders. Our laser system is arranged in modules with specific functions that are communicated by single-mode optical fibers. The power that we lose on those fibers depends on the origin of the light: for the light emitted by the tapered

amplifier, we could couple around 50% and for the light which comes from another fiber, we could reach 90%. This is because the more Gaussian-like of the input mode, the better coupling we can reach.

From the *master* laser we send 15 mW of light into a tapered amplifier (MOGLABS MOA002) obtaining around 1.25 W of optical power. We couple the output beam to a fiber to filter it into a Gaussian mode, achieving about 50% of efficiency, and send it to the fine-tuning board. It is composed of an array of various AOMs that tune with sub-MHz precision the frequency of the laser beams: the *cooling*, the $p1$, the *probe* and the *repump*. First, the beam from the tapered amplifier passes through AOM2 which drives a 60 MHz frequency, leaving it at a -151.8 detuning from the $5S_{1/2}, F = 2 \rightarrow 5P_{3/2}, F' = 3$ transition. This beam is then split into the cooling and probe beams.

The *cooling* beam passes through AOM3 in a double-pass configuration of 2×70 MHz. This changes its frequency to -11.8 MHz, which is suitable for optimizing the laser cooling. After that we incorporate the *repump* laser beam, coming from a fiber, into the same optical path and send them through a fiber into the laser cooling distribution board, see Figure 3.3. There we separate the beam into three equal parts, using a system of three polarizing beam splitters (PBS) and three $\lambda/2$. Those 3 parts provide the light for laser cooling in the x, y, and z direction of our MOT.

The *probe* beam passes through AOM4 in a double pass configuration of 75 MHz, so the frequency of this beam will end -1.8 MHz off-resonance. This allows us to variate its frequency from -20 MHz to 20 MHz around the $5S_{1/2}F = 2 \rightarrow 5P_{3/2}F' = 3$. This beam is sent to the FWM distribution board through an optical fibre. It is used to measure the optical density of the atomic cloud as mentioned in section 3.3.1

The $p1$ beam comes directly from the master laser. We send it through an AOM in double-pass configuration of 70 MHz leaving it at -60 MHz from resonance. In this way

we set the detuning Δ of the FWM process, described in Figure 3.2. We couple that into the same optical fiber as the *probe* beam and send them into the FWM distribution board. Since we do either the OD measurements or the FWM process at the same time, one of these optical paths would be blocked for each measurements.

3.2.1 Stabilization of $p2$

Our spectroscopy setup for the $p2$ light is based on [47]. Laser light at 776 nm is generated by a ECDL with a Cateye configuration (CEL002). To tune its frequency to the $5P_{3/2} \rightarrow 5D_{3/2}$ transition, we use a two-photon saturated absorption spectroscopy setup described, illustrated in the Figure 3.4 a) There we send about 3 mW of light from the master laser into a spectroscopy cell. We use the AOM to shift its frequency by 2×70 MHz, driving it to -71.8 MHz off-resonance from the $5S_{1/2}F = 2 \rightarrow 5P_{3/2}F' = 3$ transition and, at the same time, modulate it with 250 kHz.

In the opposite direction, we send the light emitted from the 776 nm laser to the cell. This counterpropagating configuration reduces the Doppler effect because only atoms with zero velocity in the transverse direction interact with both beams. After this beam passes through the spectroscopy cell, we send it to a detector connected to the Moglabs laser controller (DLC202) in charge of the locking process. When the modulated frequency $p1$ and $p2$ are on-resonance with the two-photon transition, the atoms inside the cell will absorb light from both probe beams, causing a modulation of intensity. We detect the intensity of the output beam $p2$ and obtain the saturation signal by de-modulating it.

Figure 3.4 b) shows the error signal obtained from the spectroscopy used for laser locking. A characterization made with frequency rule determines that the stronger signal correspond to the transition $5P_{3/2}, F' = 3 \rightarrow 5D_{3/2}, F'' = 3$, the next to the $5P_{3/2}, F' = 3 \rightarrow 5D_{3/2}, F'' = 2$ and $5P_{3/2}, F' = 3 \rightarrow 5D_{3/2}, F'' = 1$ is the smallest signal.

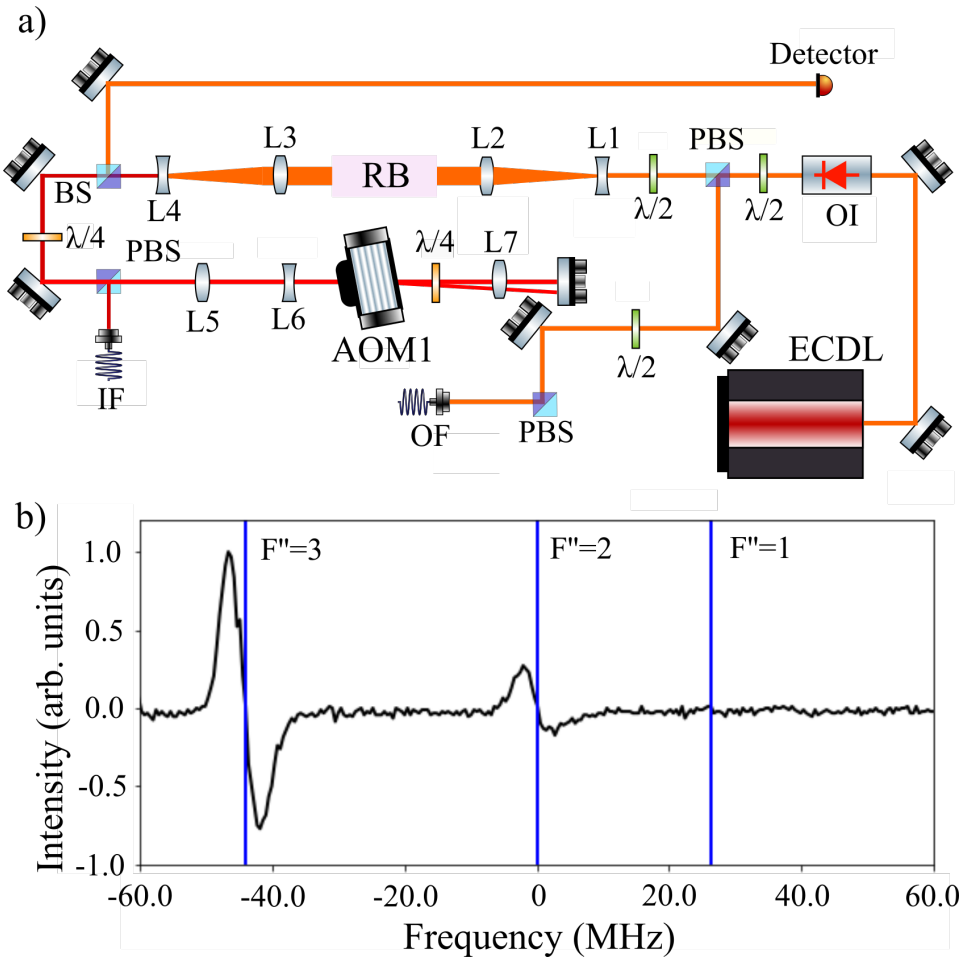

Figure 3.4: Two photon spectroscopy for the tuning of the $p2$ pump laser to the transition $5P_{3/2} \rightarrow 5D_{3/2}$. a) Optical array of two photon spectroscopy. The red line represents 780 nm light and the orange one, 776 nm. b) Typical error signal of the spectroscopy obtained from this array and used for the laser locking.

It has been previously reported that this two-photon spectroscopy requires a more sophisticated configuration due to a small saturation signal: using a PMT to detect blue fluorescence which is another possible decay path from the state $5D_{3/2}$ [48]. We found that one can simply heat the spectroscopy cell to increase the partial pressure of Rubidium by evaporating the atoms deposited on its walls to enhance the saturated absorption signal. Two 25 W resistors (10 Ω, with a 2A current) attached to the base of the cell its enough to reach about 70° C after an hour of heating. This results in a

20 mV peak-to-peak signal for the $5P_{3/2}F' = 3 \rightarrow 5D_{3/2}F'' = 3$ transition, see Figure 3.4 b). This signal is suitable for the locking with a standard PID circuit. Raising the temperature more, we can lock the laser the other hyperfine transitions $5P_{3/2}F' = 3 \rightarrow 5D_{3/2}F'' = 2$ and $5P_{3/2}F' = 3 \rightarrow 5D_{3/2}F'' = 1$. This laser provides about 25 mW of usable power and we can modify the two-photon detuning δ between -15 to 15 MHz with the AOM in this array.

3.3 Magneto-optical trap and vacuum system

To create a MOT we need high vacuum (10^{-9} Torr) and a source of Rubidium atoms. We achieve these with the compact vacuum system depicted in Figure 3.5. It contains a Hybrid pump (model NEXTORR D 100-5) that is composed of an ionic pump and a NEG (Non-evaporable getter), capable of reaching ultra-high vacuum ($< 10^{-10}$ Torr). Our science chamber Figure 3.6 is a quartz cell made of a single piece, custom made by Precision Glassblowing [49]. It has an octagonal configuration, with 1-inch lateral windows and broadband antireflection coating (550-900 nm). For a complete description of this system and its implementation, please consult reference [46].

The MOT is setup in a retroreflection configuration as shown in Figure 3.6. The collimation tubes labeled C1 and C2, consist of a telescope that amplifies the diameter of the beam from 1.1 mm to around 20 mm and a $\lambda/4$ that changes the polarization of the beam from linear to circular. Two of the beams have circular polarization in one direction, while the third beam also has circular polarization, but in the opposing direction. When the beams retroreflect the polarization direction is reversed according to Maxwells equations in a dielectric; the electric field direction remains equal after the reflection but the propagation vector reverses.

Our Rubidium source is a SAES dispenser with 1.2 cm of length (model RB/NF/3.4/12 FT10+10). Two dispensers are located in the vacuum system as shown in Figure 3.6,

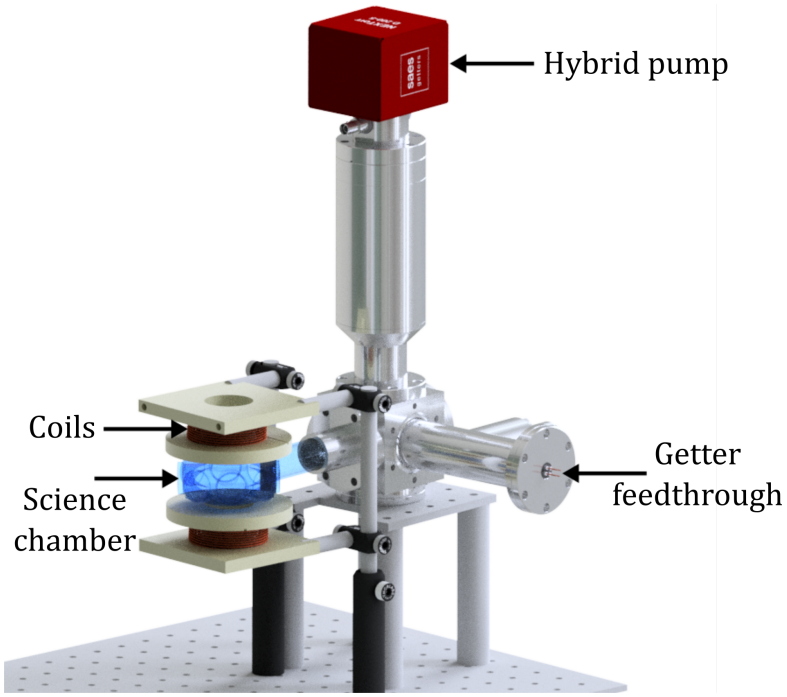

Figure 3.5: 3D render of the vaccum system used in the experiment, where the science chamber, hybrid pump, getter feedtrough and the coils are presented.

making sure that the side where the Rubidium is emitted goes towards the science chamber. They are power supplied by the shown feedthroughs.

The process of activation of the dispenser was the following: we slowly raised the current by increments of around 0.1 A each while watching the pressure inside the chamber and avoiding raises two orders of magnitud. Then, we let the system stabilize for about 30 minutes, and continue rising. The final operation current that we found was 3 A. With this current, we can create a MOT with OD up to around 20.

3.3.1 Optical density

When we have many atoms confined in a small space compared to their emission wavelength there can be modifications to the emitted light. These are known as collective effects [50], and to know how relevant they are it is important to know the number of

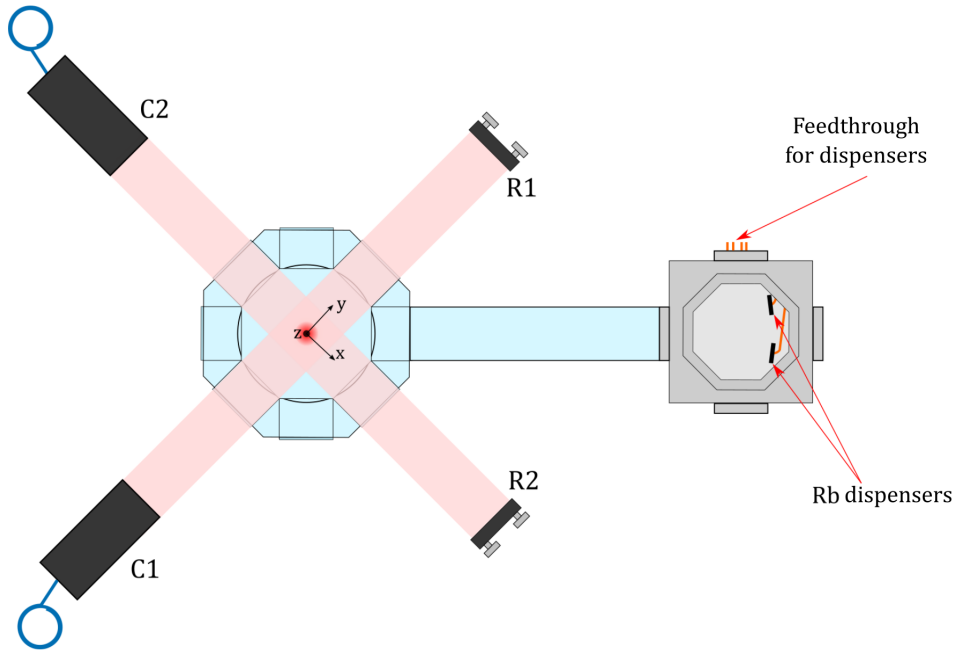

Figure 3.6: Top view of the science chamber and its connection with the vacuum system (not to scale). The coordinate system is indicated at the center of the MOT.

atoms in our trap. This section focuses on optical density (OD), a parameter that we can experimentally measure and by which we can estimate the number of atoms interacting with the FWM light. In chapter 4 we discuss a possible measurements of this effects and in section 5.1 we calculate the mean distance between atoms.

The optical density is proportional to the number of atoms interacting with the beam. Suppose that we have an atomic gas crossed by a laser beam with frequency ω near resonance to an excitable atomic transition with frequency ω_0. That beam will suffer an intensity reduction because the atoms will absorb some light, given by the Beer's Law

$$\frac{dI}{dz} = -\hbar\omega\gamma_t n = -\sigma I n, \tag{3.1}$$

where n is the atomic density, σ is the absorption cross section and γ_t is the total scattering rate, that depends on the laser detuning from the atomic transition. For a two level atom [51]

$$\gamma_t = \frac{s_0\gamma/2}{1 + s_0 + (2\underline{\Delta}/\gamma)^2}, \tag{3.2}$$

with γ being the transition natural decay rate, $\underline{\Delta} = \omega - \omega_0$, $s_0 = I/I_{sat}$ and I_{sat} is the on-resonance saturation intensity

$$I_{sat} = \frac{c\epsilon_0\gamma^2\hbar^2}{|\hat{\epsilon}\cdot\vec{d}|}, \tag{3.3}$$

which depends on the polarization of the incident light $\hat{\epsilon}$ and the direction of the atomic dipole moment operator. In the low intensity limit $I << I_{sat}$ ($s_0 < 1$) equation (3.3) is

$$\gamma_p = \frac{I\gamma}{2I_{sat}}\frac{\gamma^2}{\gamma^2 + 4\underline{\Delta}^2}. \tag{3.4}$$

Using this approximation and substituting in the equation (3.1), we have

$$I_{out} = I_0 \exp\left\{-OD\frac{\gamma^2}{\gamma^2 + 4\underline{\Delta}^2}\right\}, \tag{3.5}$$

which is an exponential of a Lorentzian. For measuring OD we use about 10 μW, yielding an intensity of $I = 1.05$ mW cm^{-2}, less than the saturation intensity of the Rubidium for this transition, $I_{sat} = 2.50$ mW cm^{-2} for linear polarization. Although the probe beam is less than the saturation intensity, both still are comparable so we are not deep in the low intensity limit.

For OD measurements in our experiment: we send the *probe* laser across the center of the MOT. Using the AOM4 in the distribution board, described in the Figure 3.3, we drive the frequency of this beam from -20 MHz to 30 MHz around resonance of the $5S_{1/2}F = 2 \rightarrow 5P_{3/2}F' = 3$ and take 3 series of data; one with the MOT turned on and

the *probe* beam present (I_{at}), the second with the MOT on and without the *probe* beam (I_{Dark}), and the last one with the MOT turned off and with the *probe* beam turned on (I_0). Then we compute absorption

$$I_{exp} = \frac{I_{at} - I_{dark}}{I_0 - I_{dark}}, \tag{3.6}$$

by substracting the background noise of the detector. A typical I_{exp} data set is depicted by the black dots in the Figure 3.7. Using equation (3.5) we fit the experimental points with a Lorentzian function with the Optical Density(OD) as the only free parameter.

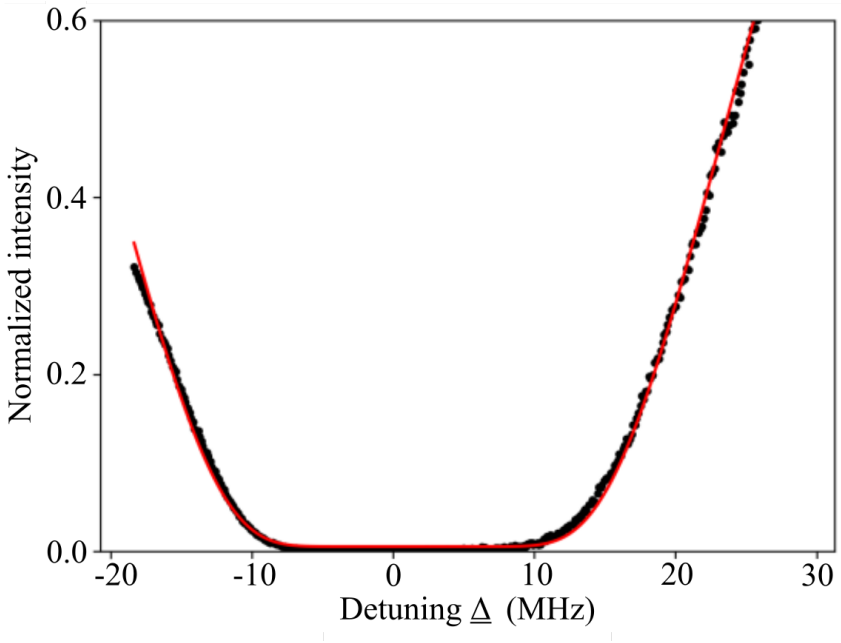

Figure 3.7: Typical data set (black dots) and fit (red curve) for the optical density of our MOT. For this case we measure a OD of 20.3 ± 0.1. The experimental parameters were: detuning ϵ of -25 MHz, Pressure 10^{-9} Torr, magnetic gradient of 23 Gauss cm^{-1} and *repump* power of 5 mW.

Figures 3.8 and 3.9 show an OD characterization of the MOT as a function of: the detuning of the cooling beam, the pressure inside the vacuum chamber, (proportional to the atoms emitted by the dispenser), the gradient from our quadrupole magnetic

field and the power of the re-pump beam (measured at the input of the laser cooling distribution board, Figure 3.3). This caracterization was done following this order: (i) detuning ϵ, (ii) pressure, (iii) magnetic gradient, and (iv) repump power. After the series of data was taken, we choose the parameter that yields larger OD. Those parameters were: $\epsilon = -23$ MHz, pressure of 10^{-9} Torr, a magnetic gradient of 22 Gauss cm^{-1} and 9 mW of repump power.

Figure 3.8 shows the OD dependency on the detuning of the ϵ cooling beam (blue) and the pressure inside the vacuum chamber (black). As a function of ϵ, OD displays a linear behavior up to a maximum, around 23 MHz. From the observed behavior one can conclude that the cooling detuning ϵ is a suitable parameter to variate OD from 8 to about 19. To get the black experimental dots in Figure 3.8 we worked with a base pressure of 10^{-10} Torr and gradually increased it by raising the current through one of the Rubidium dispensers. From these data we can see that the OD behaves like a logarithmic function, reaching a saturation point around 4×10^{-9} Torr. We usually do not change this parameter because the changes in pressure are slow, so we would have to wait longer between experiments. Also this could make it hard to reproduce the same experimental conditions.

The variation of OD as a function of the re-pump power and the quadrupole magnetic field are plotted in Figure 3.9. Both have similar behavior raising at the start and reaching a maximum of 23 and 20 respectively. For higher values, the OD decreases in both cases. Both of these parameters can be considered when we want to make small adjustments in the OD.

From this characterization we can conclude that our experimental control of OD goes from 8 to 24. The detuning ϵ is the better parameter to variate OD because it behaves linearly. For small adjustments we can change either the *repump* power or the magnetic

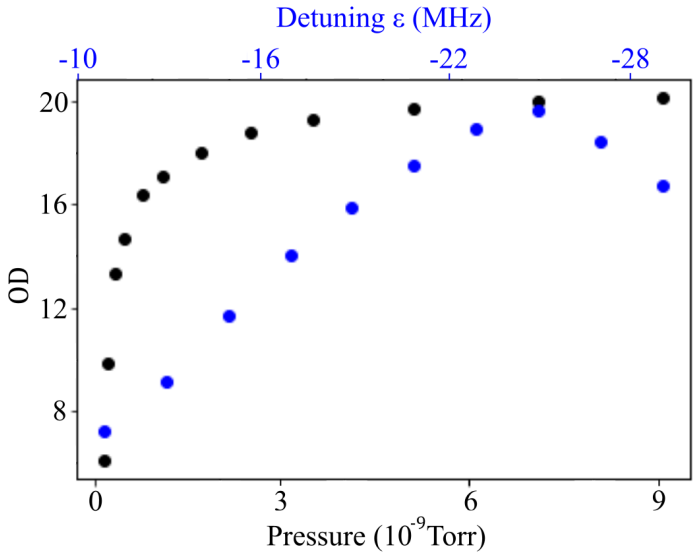

Figure 3.8: Variation of OD with respect to the detuning ϵ of the cooling laser (Figure 3.1) in blue and the pressure inside the vacuum chamber in black. For the black points the experimental parameters were: a detuning ϵ of -25 MHz, a magnetic gradient of 20 Gauss cm^{-1} and a repump power of 3 mW. For data in blue: a repump power of 3 mW, a pressure of 10^{-9} Torr and a magnetic gradient of 20 Gauss cm^{-1}.

gradient. However the change in the magnetic gradient also modifies the size of the MOT. So the best parameters for control OD are the *repump* power and the cooling detuning ϵ.

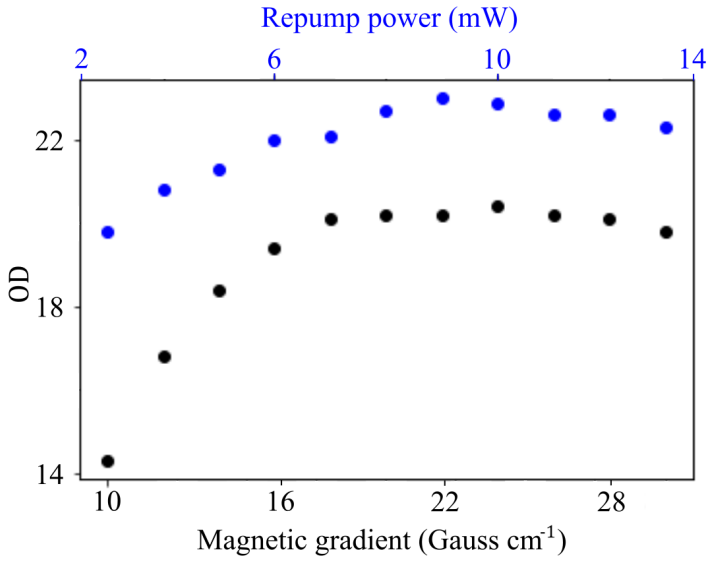

Figure 3.9: Variation of OD with respect to the re-pump power (in blue) and the quadrupole magnetic field (in black). For the black points the experimental parameters were: a detuning ϵ of -25 MHz, a pressure of 10^{-9} Torr and a repump power of 3 mW. For data in blue: a detuning ϵ of -25 MHz, a pressure of 10^{-9} Torr, a magnetic gradient of 22 Gauss cm^{-1}.

3.4 FWM pumping and photon-pair collection

The left side of Figure 3.10 shows the experimental setup for the FWM pumping. It has three inputs for preparing the polarization and send the $p1$, $p2$ and *seed* beams to the experiment. We chose a collinear configuration for the FWM pumping because in this way we facilitate the photon collection. Using a PBS, we match the *seed* and $p1$ beams optical paths, and finally, we use an interference filter (IF1) to combine them with the $p2$ beam, making the three of them collinear. In this case the phase matching condition of equation (2.41) is fulfilled trivially: all of the waves involved in the FWM process travel in the same direction.

The detection system is presented on the right-hand side of Figure 3.10. It filters the signal and idler photos and guide them into the avalanche photodetectors (APD). Given

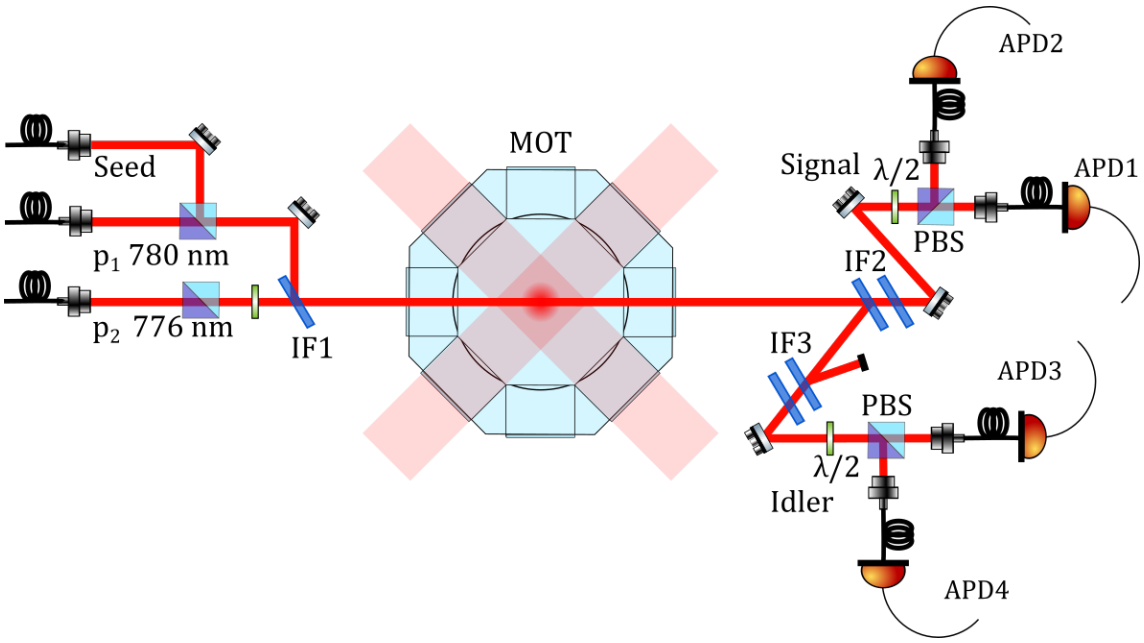

Figure 3.10: Schematics of the optical pumping (left) and the photon collection system. The later consists of a separation of frequency using two Interference filters, followed by a separation of polarization, using a $\lambda/2$ and a PBS. We can monitor each component of the polarization state of the photons simultaneously.

our collineal configuration the strong pump beams and the low-power signal and idler photons exit from the atomic gas in the same direction. To our advantage these frequencies are all separated by at least 4 nm, which gives us the option of using interference narrowband filters to separate them. The filters we use have a 2 nm linewidth and it is possible to tune their center frequency by changing the angle between the filter and the incident beam. So we can choose the transmission frequency for each optical path. To further reduce the noise, we use two filters at the same angle for each photon path, two filters centered in 780 nm for the signal photon (762 nm) and two filters centered in 808 nm for the idler photon (795 nm).

After the filtering we send the signal and idler photons through a half-waveplate ($\lambda/2$), a polarization beamsplitter (PBS), and we couple each exit component of the

PBS into an optical fiber. Finally we connect each of those four fibers into an avalanche photodiode (ID120). These APDs can detect single photons with a quantum efficiency $> 70\%$ for near infrared photons. They have an active area of 500 μm, a dark count rate of around 300 counts/s, and a typical time resolution of 400 ps.

The alignment process of the detection modules is the following: we first send the $p1$, the $p2$ and the *seed* beams into the MOT with the APDs turned off. Then we use a CMOS camera (DCC1545M) and put it in front of the beam after the first filter IF2 is in place. Then we rotate it making sure that only the 762 nm light is passing through (we do that by blocking each pump beam separately and noticing that every time we lose all the signal detected by the camera). We perform the same process for the second filter IF2. After that, we guide the generated 762 nm light into the optical fiber and then couple it. For us, this was the trickiest part because we do not have a laser source with 762 nm, so we cannot align the signal part of the array by sending a laser beam with 762 nm.

The optical path of the idler photons is less complicated because we have a laser source with 795 nm. We can align the filters IF3 and the corresponding optical fiber with the seed beam. After that, we turn it off and connect the fibers to the APDs looking for counts. The goal is to detect even a little signal at the APD because then it can be optimized. We use the coincidences between APD channels as an optimization parameter because if we optimize using the individual counts we usually couple photons coming from the spontaneous emission and not from the parametric process.

We do the alignment process with both transmitted and reflected components of the PBS. We use the coincidences detected in pairs of channels in order to align each optical path. This allows us to monitor each of the two outputs of the PBS for the two different

photons. This setup is intended for polarization correlations experiments and density matrix reconstruction via quantum tomography, which we will explore in the near future.

3.4.1 A note regarding noise in detectors

The avalanche photo-detectors not only read the signal sourced by the photon pairs, but they can also detect noise with diverse origin. For example the *dark count noise* is the current present an APD circuit even with no light arriving at the detector. Thermal noise is another example, it arises in the (load) resistor that transforms the current into the signal voltage. In this note we analyze the most fundamental one: the *quantum shot noise*.

Photons arriving at an APDs active area generate electrons that, using a bias voltage, produce a current called *photocurrent*. Not every photon contributes to this photocurrent. The probability of having n free electrons contributing to the photocurrent is given by the *distribution of Poisson* [52]

$$p(n) = \frac{N^n e^{-N}}{n!}, \tag{3.7}$$

where N is the average number of detected photons in an interval δt. By using the Stirling's formula it can be proved that for the limit $N \to \infty$ this probability turns into a Gaussian distribution [52]

$$p(x) = \frac{e^{-(x-\sigma)^2/(2\sigma)}}{\sqrt{2\pi\sigma}}, \tag{3.8}$$

where σ is its variance. Thus if we consider each of the noise sources (thermal noise, dark count noise) as an independent random variable, and apply the central limit theorem to each distribution, we can assume that the noise of our detectors follows a Gaussian distribution [53]. This will become important in the section 2.3, where we add a noise Gaussian distribution and the theorical $g^{(2)}_{SI}(\Delta t)$ distribution by performing a convolution between them.

To reduce the dark counts present in our APDs we turn them on without input signal and check how many counts they are detecting. We can modify their nominal operation temperature -40°C and bias current 30 V to reduce the dark counts. We set each of them to around 100 counts per second.

3.5 Experimental sequence

A schematics of the duty cycle in our photon pair experiments can be found in Figure 3.11. We have a loading time of 500 μs, where the atoms are trapped in the MOT. This is followed by 200 μs where the MOT is turned off. At this stage we trigger the APD1 and APD2 gate for the photon count to start and turn on the $p1$ beam. It is worth noticing that the coils, the re-pump, and the $p2$ beam are always turned on. Given the size of the pumping beams and the gradient (20 Gauss cm^{-1}), we conclude that the magnetic fields effects could have in the trapped atoms via Zeeman effect are neglectable because they only produce an energy shift of about 1 MHz on atoms at the border of the beam.

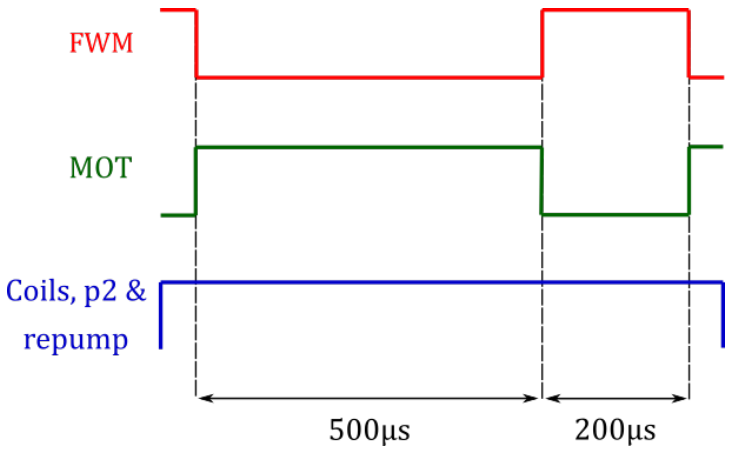

Figure 3.11: Schematics of a typical duty cycle in our FWM experiments. In green we have the MOT loading stage of 500 μs, with the cooling, re-pump, and coils present. This is followed by a 200 μs FWM pulse, in red. At this stage we turn off the cooling beams, turn on $p1$ and turn on the gating for the APD acquisition. The coils, repump and $p2$ always are turned on (blue).

For controlling the pulses of this sequence and the OD measurements, we use a low-cost data acquisition DAQ card, brand Labjack and model T7. It has 23 digital input/output channels, 2 analog outputs, and a 32 KB RAM memory card. This card is capable of providing us with the necessary response time in both of these applications. More details are discussed in [54, 55].

Chapter 4

Temporal statistics and correlations of the generated photons

In this chapter, I show an analysis of the temporal statistics measurements and coherence of the photon pairs generated in our system. Considering the time evolution of a consecutive cascade-decay given by the Schrödinger equation, an expression for the second-order coherence is reached. It is used to fit our experimental data for the cross-correlation function between signal and idler photons. Measurements of the auto-correlation functions are also analyzed. Using those measurements we found a strong violation of the Cauchy-Schwarz inequality, indicating that the temporal coherence of our photon pairs has a non-classical nature.

4.1 Theory of cascade-decay

Let us consider a double decay configuration, where an atom is initialy in an excited level $|a\rangle$, later it decays to a level $|b\rangle$ and then to a ground state $|c\rangle$, as described in Figure 4.1. The decay generates two consecutive photons k and q, with frequencies ω_k and ω_q respectively, which passes first through a state $|b\rangle$ and ends at a ground state $|c\rangle$. The interaction Hamiltonian of this three-level atom and the emmited radiation field is, after using the RWA in equation (2.64)

$$H_I = \hbar \sum_k \left(g_{ak} \sigma_+^{(1)} \hat{a}_k e^{i(\omega_{ab} - \omega_k)t} + h.c. \right) + \hbar \sum_q \left(g_{bq} \sigma_+^{(2)} \hat{a}_q e^{i(\omega_{bc} - \omega_q)t} + h.c. \right), \tag{4.1}$$

where we sum over modes labeled with k and q for each decay, g_{ij} are the coupling constants for $|a\rangle \rightarrow |b\rangle$ and $|b\rangle \rightarrow |c\rangle$ respectively and $\sigma_+^{(1)} = |a\rangle\langle b|$ and $\sigma_+^{(2)} = |b\rangle\langle c|$ are the corresponding raising atomic operators for each decay.

The state of the system at time t can be written as

$$|\psi(t)\rangle = c_a(t)|a, 0_k, 0_q\rangle + \sum_k c_{bk}(t)|b, 1_k, 0_q\rangle + \sum_{k,q} c_{c,k,q}(t)|c, 1_k, 1_q\rangle, \tag{4.2}$$

where the first entry in each ket correspond to the atomic states, the second and third entry are the number of photons emitted in the modes k and q respectively. Finally $c_a, c_{b,k}$ and $c_{c,k,q}$ are time-dependent probability amplitudes to be determined. From the Schrödinger equation in the interaction picture given by

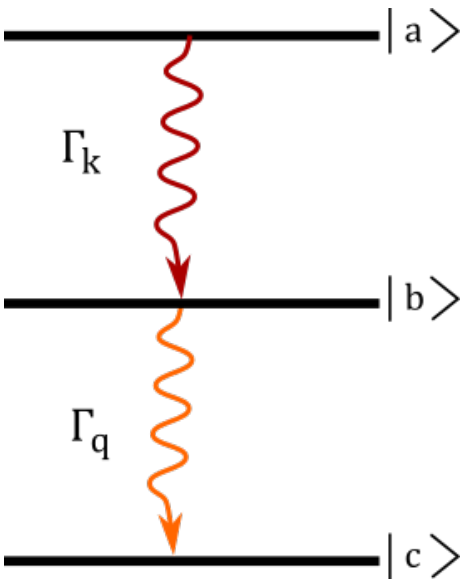

Figure 4.1: Energy diagram of a double decay in a three level atom. The excited states $|a\rangle$ and $|b\rangle$ have the correspondant decay rates Γ_a, Γ_b and emmit two photons, labeled k, q respectively.

$$\frac{d}{dt}|\psi(t)\rangle = -\frac{i}{\hbar}H_I|\psi\rangle, \tag{4.3}$$

we have in the left side term

$$\frac{d}{dt}|\psi(t)\rangle = \dot{c}_a(t)|a,0_k,0_q\rangle + \sum_k \dot{c}_{bk}(t)|b,1_k,0_q\rangle + \sum_{k,q}\dot{c}_{c,k,q}(t)|c,1_k,1_q\rangle, \tag{4.4}$$

while for the right side:

$$\begin{aligned} H_I|\psi(t)\rangle = \hbar\{\sum_k\left(\Omega_{ak}\sigma_+^{(1)}\hat{a}_k e^{i(\omega_{ab}-\omega_k)t}+h.c.\right)+\sum_q\left(\Omega_{bq}\sigma_+^{(2)}\hat{a}_q e^{i(\omega_{bc}-\omega_q)t}+h.c.\right)\}c_a(t)|a,0_k,0_q\rangle \\ +\hbar\{\sum_k\left(\Omega_{ak}\sigma_+^{(1)}\hat{a}_k e^{i(\omega_{ab}-\omega_k)t}+h.c.\right)+\sum_q\left(\Omega_{bq}\sigma_+^{(2)}\hat{a}_q e^{i(\omega_{bc}-\omega_q)t}+h.c.\right)\}\sum_k c_{bk}(t)|b,1_k,0_q\rangle \\ +\hbar\{\sum_k\left(\Omega_{ak}\sigma_+^{(1)}\hat{a}_k e^{i(\omega_{ab}-\omega_k)t}+h.c.\right)+\sum_q\left(\Omega_{bq}\sigma_+^{(2)}\hat{a}_q e^{i(\omega_{bc}-\omega_q)t}+h.c.\right)\}\sum_{k,q} c_{c,k,q}(t)|c,1_k,1_q\rangle. \end{aligned} \tag{4.5}$$

Simplifying the last equation by applying the definition of the atomic and radiation operators σ_+, σ_- and $a, a^\dagger$, the only non-zero terms are

$$\begin{aligned} H_I|\psi\rangle = \hbar\sum_k \Omega_{ak}e^{i(\omega_{ab}-\omega_k)t}c_{bk}(t)|a,0_k,0_q\rangle + \hbar\sum_{kq}\Omega_{bq}e^{-1(\omega_{bc}-\omega_q)t}c_{c,k,q}|b,1_k,0_q\rangle \\ +\hbar\left(\sum_k\Omega_{ak}e^{i(\omega_{ab}-\omega_k)t}c_a+\sum_k\Omega_{bq}e^{-i(\omega_{bc}-\omega_q)t}c_{c,k,q}\right)|c,1_k,1_q\rangle. \end{aligned} \tag{4.6}$$

On both sides of equation (4.3) we have terms multiplying ket states. Those coefficients have to be equal in each case, leading to a system of differential equations

$$\begin{aligned} \dot{c}_a(t) &= -i\sum_k\Omega_{ak}e^{i(\omega_{ab}-\omega_k)t}c_{bk}, \\ \dot{c}_{bk}(t) &= -ic_a\Omega_{ak}e^{-i(\omega_{ab}-\omega_k)t} - i\sum_q\Omega_{bq}c_{c,k,q}e^{i(\omega_{bc}-\omega_q)t}, \\ \dot{c}_{c,k,q}(t) &= -i\Omega_{bq}c_{b,k}e^{-i(\omega_{bc}-\omega_q)t}. \end{aligned} \tag{4.7}$$

We consider now the Weisskopf-Wigner approximation [39], which reads

$$\begin{aligned} -i\sum_k\Omega_{ak}c_{b,k}e^{i(\omega_{ab}-\omega_k)t} &\simeq -\frac{\Gamma_a}{2}c_a, \\ -i\sum_{k,q}\Omega_{bk}c_{c,k,q}e^{i(\omega_{bc}-\omega_q)t} &\simeq -\frac{\Gamma_b}{2}c_{b,k}, \end{aligned} \tag{4.8}$$

where Γ_a and Γ_b are the decay rates of each level. This approximation considers that we are interested in time scales much larger than the transition frequencies i.e, $t >>$

$1/\omega_{ab}, 1/\omega_{bc}$. So, when we integrate formally the system of equations (4.7), we can change the sum of modes k to an integral and change the upper time integration limit to infinity, which gives us the Einstein A coefficient [39]. Substituting equation (4.8) into (4.7), we get:

$$\begin{aligned}
\dot{c}_a(t) &= -\frac{\Gamma_a}{2}c_a, \\
\dot{c}_{bk}(t) &= -ic_a\Omega_{ak}e^{-i(\omega_{ab}-\omega_k)t} - \frac{\Gamma_b}{2}c_{b,k}, \\
\dot{c}_{c,k,q}(t) &= -i\Omega_{bq}c_{b,k}e^{-i(\omega_{bc}-\omega_q)t}.
\end{aligned} \tag{4.9}$$

The solution for the first coefficient is straightforward: $\dot{c}_a(t) = e^{-\Gamma_a t/2}$. Substituting that in the equation of $\dot{c_{b,k}}$ and integrating

$$\begin{aligned}
c_{bk}(t) &= -i\Omega_{ak}\int_0^{t_f} dt' e^{-i(\omega_{ab}-\omega_k)t-\Gamma_a(t-t')/2}e^{-\Gamma_b t/2}, \\
&= -i\Omega_{ak}\frac{e^{(i(\omega_k-\omega_{ab})-\Gamma_a/2)t'-\Gamma_b/2(t-t')}}{-i(\omega_{ab}-\omega_k)-\frac{1}{2}(\Gamma_a-\Gamma_b)}\Bigg|_0^{t_f}, \\
&= -i\Omega_{ak}\frac{e^{(i(\omega_k-\omega_{ab})-\Gamma_a/2)t} - e^{-\Gamma_b t/2}}{i(\omega_k-\omega_{ab})-\frac{1}{2}(\Gamma_a-\Gamma_b)}.
\end{aligned} \tag{4.10}$$

To find $c_{c,k,q}$, we use the last expression and plug it into equation (4.9)

$$\begin{aligned}
\dot{c}_{c,k,q}(t) &= -i\Omega_{bq}e^{-i(\omega_{bc}-\omega_q)t}\left(-i\Omega_{ak}\frac{e^{(i(\omega_k-\omega_{ab})-\Gamma_a/2)t} - e^{-\Gamma_b t/2}}{i(\omega_k-\omega_{ab})-\frac{1}{2}(\Gamma_a-\Gamma_b)}\right), \\
&= \Omega_{bq}\Omega_{ak}e^{-i(\omega_{bc}-\omega_q)t}\left(\frac{e^{(i(\omega_k-\omega_{ab})-\Gamma_a/2)t} - e^{-\Gamma_b t/2}}{i(\omega_k-\omega_{ab})-\frac{1}{2}(\Gamma_a-\Gamma_b)}\right), \\
&= \Omega_{bq}\Omega_{ak}\left(\frac{e^{(i(\omega_k-\omega_{ab})-\Gamma_a/2)t-i(\omega_{bc}-\omega_q)t} - e^{-\Gamma_b t/2-i(\omega_{bc}-\omega_q)t}}{i(\omega_k-\omega_{ab})-\frac{1}{2}(\Gamma_a-\Gamma_b)}\right).
\end{aligned} \tag{4.11}$$

Integrating

$$\begin{aligned}
c_{c,k,q}(t) &= \frac{\Omega_{bq}\Omega_{ak}}{i(\omega_k-\omega_{ab})-\frac{1}{2}(\Gamma_a-\Gamma_b)}\int_0^t dt'\left(e^{(i(\omega_k-\omega_{ab})-\Gamma_a/2)t'-i(\omega_{bc}-\omega_q)t'} - e^{-\Gamma_b t'/2-i(\omega_{bc}-\omega_q)t'}\right), \\
&= \frac{\Omega_{bq}\Omega_{ak}}{i(\omega_k-\omega_{ab})-\frac{1}{2}(\Gamma_a-\Gamma_b)}\left[\frac{e^{(i(\omega_k+\omega_q-\omega_{ac})-\Gamma_a/2)t}}{i(\omega_k+\omega_q-\omega_{ac})-\Gamma_a/2} - \frac{e^{(i(\omega_q-\omega_{bc})-\Gamma_b/2)t}}{i(\omega_q-\omega_{bc})-\Gamma_b/2}\right],
\end{aligned} \tag{4.12}$$

and taking the limit for $t >> 0$

$$\begin{aligned} c_{c,k,q}(\infty) &= \frac{\Omega_{bq}\Omega_{ak}e^{-i(k+q)r}}{i(\omega_k-\omega_{ab})-\frac{1}{2}(\Gamma_a-\Gamma_b)}\left[\frac{1}{i(\omega_k+\omega_q-\omega_{ac})-\Gamma_a/2}-\frac{1}{i(\omega_q-\omega_{bc})-\Gamma_b/2}\right], \\ &= \frac{\Omega_{bq}\Omega_{ak}e^{-i(k+q)r}}{i(\omega_k-\omega_{ab})-\frac{1}{2}(\Gamma_a-\Gamma_b)}\left[\frac{i(\omega_k-\omega_{ab}-(\frac{\Gamma_a+\Gamma_b}{2}))}{(i(\omega_k+\omega_q-\omega_{ac})-\Gamma_a/2)(i(\omega_q-\omega_{bc})-\Gamma_b/2)}\right], \\ &= \frac{\Omega_{bq}\Omega_{ak}e^{-i(k+q)r}}{(i(\omega_k+\omega_q-\omega_{ac})-\Gamma_a/2)(i(\omega_q-\omega_{bc})-\Gamma_b/2)}. \end{aligned} \tag{4.13}$$

We consider the steady-state limit, from equation (4.2) we can conclude that $c_a(\infty) = c_{b,k}(\infty) = 0$ because for a long time the atom would be in the ground state $|c\rangle$. Therefore, for the steady-state limit the state of the atomic system is

$$|\psi\rangle = \sum_{k,q}\frac{\Omega_{bq}\Omega_{ak}e^{-i(k+q)\cdot r}}{(i(\omega_k+\omega_q-\omega_{ac})-\Gamma_a/2)(i(\omega_q-\omega_{bc})-\Gamma_b/2)}|c,1_k,1_q\rangle. \tag{4.14}$$

Now, recall that the two-photon correlation function in equation (2.29) can be written as

$$G^{(2)}_{DD}(\mathbf{r}_1,t_1;\mathbf{r}_2,t_2) = \langle 0|\hat{\mathbf{E}}^{(+)}(\mathbf{r}_2,t_2)\hat{\mathbf{E}}^{(+)}(\mathbf{r}_1,t_1)|\psi\rangle, \tag{4.15}$$

where the subscript DD means double decay and $|0\rangle$ is the initial state and then calculate it using the quantized electric fields of equation (2.35)

$$
\begin{aligned}
G^{(2)}_{DD}(t_1,t_2) &= \sum_{k,q}\sum_{i,s}\langle 0|a_i a_s e^{-i(\omega_i t_1+\mathbf{i}\cdot\mathbf{r}_1)}e^{-i(\omega_s t_2+\mathbf{s}\cdot\mathbf{r}_2)} \\
&\quad \frac{-\Omega_{bq}\Omega_{ak}e^{-i(k+q)\cdot r}}{(i(\omega_k+\omega_q-\omega_{ac})-\Gamma_a/2)(i(\omega_q-\omega_{bc})-\Gamma_b/2)}|c,1_k,1_q\rangle, \\
&= \sum_{k,q}\sum_{i,s}\langle 0|\delta_{k,i}\delta_{q,s}e^{-i(\omega_i t_1+\mathbf{i}\cdot\mathbf{r}_1)}e^{-i(\omega_s t_2+\mathbf{s}\cdot\mathbf{r}_2)} \\
&\quad \frac{-\Omega_{bq}\Omega_{ak}e^{-i(k+q)\cdot r}}{(i(\omega_k+\omega_q-\omega_{ac})-\Gamma_a/2)(i(\omega_q-\omega_{bc})-\Gamma_b/2)}|0\rangle, \\
&= \sum_{k,q} e^{-i(\omega_k t_1+\mathbf{k}\cdot\mathbf{r}_1)}e^{-i(\omega_q t_2+\mathbf{q}\cdot\mathbf{r}_2)}e^{-i(\omega_k t_2+\mathbf{k}\cdot\mathbf{r}_2)}e^{-i(\omega_q t_1+\mathbf{q}\cdot\mathbf{r}_1)} \\
&\quad \frac{-\Omega_{bq}\Omega_{ak}e^{-i(k+q)\cdot r}}{(i(\omega_k+\omega_q-\omega_{ac})-\Gamma_a/2)(i(\omega_q-\omega_{bc})-\Gamma_b/2)}.
\end{aligned}
\tag{4.16}
$$

For making the sum over all the k and q modes we consider the continuous limit, asuming the emission spectrum are sharply peaked Lorentzians [39]

$$
\begin{aligned}
G^{(2)}_{DD}(t_1,t_2) &= -\int_k d\mathbf{k}\int_q d\mathbf{q} e^{-i(\omega_k t_1+\mathbf{k}\cdot\mathbf{r}_1)}e^{-i(\omega_q t_2+\mathbf{q}\cdot\mathbf{r}_2)}e^{-i(\omega_k t_2+\mathbf{k}\cdot\mathbf{r}_2)}e^{-i(\omega_q t_1+\mathbf{q}\cdot\mathbf{r}_1)} \\
&\quad \frac{\Omega_{bq}\Omega_{ak}e^{-i(k+q)\cdot r}}{(i(\omega_k+\omega_q-\omega_{ac})-\Gamma_a/2)(i(\omega_q-\omega_{bc})-\Gamma_b/2)}.
\end{aligned}
\tag{4.17}
$$

Now, simplifying and splitting the integrals into angular and radial factors, we get

$$
\begin{aligned}
G^{(2)}_{DD}(t_1,t_2) &= -\int_0^\infty k^2 dk\int_0^\pi \sin\theta_k{}^2 d\theta_k\int_0^{2\pi} d\phi_k\int_0^\infty q^2 dq\int_0^\pi \sin\theta_q{}^2 d\theta_q\int_0^{2\pi} d\phi_q \\
&\quad \times e^{-i(\omega_k t_1+k\Delta r_1\cos\theta_k)}e^{-i(\omega_q t_2+q\Delta r_2)\cos\theta_q}e^{-i(\omega_k t_2+k\Delta r_2\cos\theta_k)}e^{-i(\omega_q t_1+q\Delta r_1)\cos\theta_q} \\
&\quad \times \frac{\Omega_{bq}\Omega_{ak}}{(i(ck+cq-\omega_{ac})-\Gamma_a/2)(i(cq-\omega_{bc})-\Gamma_b/2)}, \\
&= \frac{(2\pi)^2}{\Delta r_1\Delta r_2}k_0 q_0\Omega_{bq}\Omega_{ak} \\
&\quad \times \int_0^\infty\int_0^\infty dkdq\frac{e^{-ickt_1}(e^{-ik\Delta r_1}-e^{ik\Delta r_1})e^{-ickt_1}(e^{-iq\Delta r_2}-e^{iq\Delta r_2})}{(i(ck+cq-\omega_{ac})-\Gamma_a/2)(i(cq-\omega_{bc})-\Gamma_b/2)}.
\end{aligned}
\tag{4.18}
$$

For the integral of k and q we consider extending the lower limit to $-\infty$. This leads us to a complex integral for k and q. Each one of them has a pole in $q=(\Gamma_b/2+\omega_{bc})/c$ and $k=(\omega_{ac}-i\Gamma_a/2)/c-q$. By applying the Cauchy integral theorem [56]

$$
\frac{1}{2\pi i}\int_{-\infty}^{\infty} e^{i\chi t}\frac{1}{\chi-i\epsilon}d\chi=\Theta(t),
\tag{4.19}
$$

where the $\Theta(t)$ is the Heaviside step function. Equation (4.18) is

$$\begin{aligned} G^{(2)}_{DD}(t_1,t_2) &= \frac{-(2\pi)^4 k_0 q_0 \Omega_{bq}\Omega_{ak}}{\Delta r_1 \Delta r_2} e^{-(i\omega_{bc}+\Gamma_a/2)(t_1-\Delta r_1/c)}\Theta(t_1-\Delta r_1/c) \\ &\times e^{-(i\omega_{bc}+\Gamma_{b/2})[(t_2-\Delta r_2/c)-(t_1-\Delta r_1/c)]}\Theta[(t_2-\Delta r_2/c)-(t_1-\Delta r_1/c)], \\ &= \frac{-(2\pi)^4 k_0 q_0 \Omega_{bq}\Omega_{ak}}{\Delta r_1 \Delta r_2} e^{-(i\omega_{bc}+\Gamma_a/2)(t_2-\Delta r_2/c)}\Theta(t_2-\Delta r_2/c) \\ &\times e^{-(i\omega_{bc}+\Gamma_{b/2})[(t_1-\Delta r_1/c)-(t_2-\Delta r_2/c)]}\Theta[(t_1-\Delta r_1/c)-(t_2-\Delta r_2/c)], \end{aligned} \tag{4.20}$$

if we define $\Delta\tau = (t_1 - \Delta r_1/c) - (t_2 - \Delta r_2/c)$, this equation can be written as [39]

$$G^{(2)}_{DD}(\Delta\tau) = A_0 e^{-\Gamma_b/2\Delta\tau}\Theta(\Delta\tau), \tag{4.21}$$

where A_0 is a constant and for $\Delta\tau << \Gamma_a^{-1}$; it can be shown [39] that the decaying term $\exp\{-\Gamma_a/2(t_2 - \Delta r_2/c)\}$ goes also to a constant, assuming $\Gamma_k < \Gamma_q$. Our system fulfills it given: $\Gamma_k = 0.6$ MHz corresponding to the $5D_{3/2}$ and $\Gamma_q = 36$ MHz. Equation (4.21) is the same result that was deduced in the 70s [57] by using *Green's function formalism*. It tells us that the cross-correlation function of photon pairs produced in a consecutive decay as a function of $\Delta\tau$ would behave as a decaying exponential with a constant $\Gamma_b/2$ multiplied by a Heaviside step function. This is an asymmetric function because of the well-ordered decays of this system. Equation (4.21) tells us also that if we measure the cross correlation fuction $G^{(2)}_{DD}(\Delta\tau)$ we can determine the decay constant Γ_b of the intermediate level.

4.2 Experimental measurements

In this section, I present the analysis of the experimental data and the measurements of the autocorrelation and cross-correlation functions. This constitutes a first characterization of our photon source properties and time coherence.

4.2.1 Coincidence measurements

If we consider two detectors at positions $\mathbf{r}_1$ and $\mathbf{r}_1$, we can measure the statistical correlation of the optical field at these two locations. With the help of an AND gate we can measure coincidences with our detectors. An AND gate is an electronic circuit with two inputs that can only send a pulse if it receives a signal in both of them. We use an AND gate to measure coincidences from photons arriving within the duration of a set time T_R, see Figure 4.2.

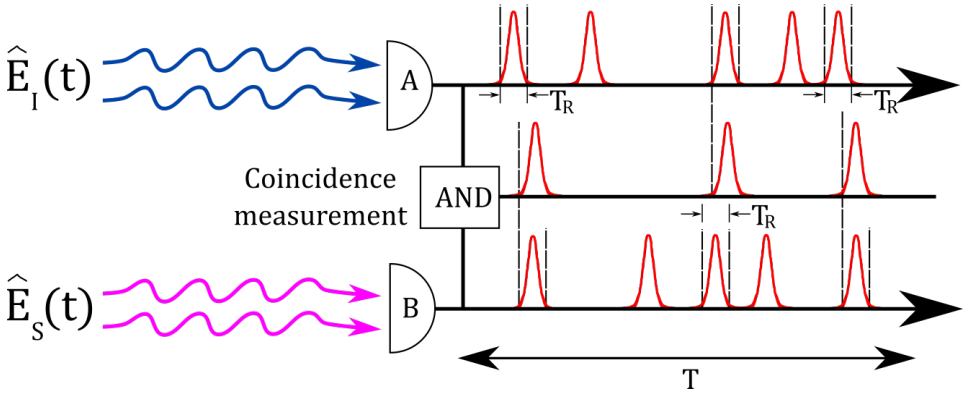

Figure 4.2: Coincidence measurements between fields $\hat{E}_s(t)$ and $\hat{E}_I(t)$ arriving to detector A and B respectively. When two pulses overlap within a time T_R we detect one coincidence. The time T is the total integration time. Figure adapted from [58].

According to detection theory, the joint probability of detecting an arriving photon in detector A during a time interval t' to $t'+dt'$ and another photon by detector B during the interval t'' to $t''+dt''$ is

$$p_{SI}(t',t'')dt'dt'' = \alpha'\alpha''\langle\hat{E}_I^{(-)}(t'')\hat{E}_S^{(-)}(t')\hat{E}_S^{(+)}(t')\hat{E}_I^{(+)}(t'')\rangle dt'dt'', \tag{4.22}$$

where α' and α'' are the efficiency of each detector A, and B. The brackets means the expectation value. Integrating over time we obtain the coincidence rate of two photons in a finite time integral T

$$C_{SI} = \int_T p_{SI}(t', t'')dt'dt'' = \frac{\alpha'\alpha'}{T}\int_{-T/2}^{T/2}\int_{-T/2}^{T/2}\langle \hat{E}_I^{(-)}(t'')\hat{E}_S^{(-)}(t')\hat{E}_S^{(+)}(t')\hat{E}_I^{(+)}(t'')\rangle dt'dt''. \tag{4.23}$$

Recalling the definition of the general correlation function in equation (2.30) for N=2, given that we have two detectors

$$G^{(2)}(t_1, t_2) = \langle \hat{E}^{(-)}(t_2)\hat{E}^{(-)}(t_1)\hat{E}^{(+)}(t_1)\hat{E}^{(+)}(t_2)\rangle. \tag{4.24}$$

Equation 4.24 states that the coincidence rate of two photons its proportional to their second-order cross-correlation function. In other words, when we make a coincindence detection between the signal and idler phtons, we are measuring $G^{(2)}_{SI}(t_1, t_2)$. If we normalize equation (4.24) by the product of the intensities we have the second-order degree of coherence function

$$g^2(\mathbf{x}_1, \mathbf{x}_1) = \overline{C_{SI}} = \frac{\langle \hat{E}^{(-)}(\mathbf{x}_2)\hat{E}^{(-)}(\mathbf{x}_1)\hat{E}^{(+)}(\mathbf{x}_1)\hat{E}^{(+)}(\mathbf{x}_2)\rangle}{\langle \hat{E}^{(-)}(\mathbf{x}_2)\hat{E}^{(+)}(\mathbf{x}_2)\rangle\langle \hat{E}^{(-)}(\mathbf{x}_1)\hat{E}^{(+)}(\mathbf{x}_1)\rangle}, \tag{4.25}$$

where $\overline{C_{SI}}$ means the normalized coincidence rate.

4.2.2 Cross-correlation measurements

It has been shown that the second-order coherence $g^{(2)}_{SI}(\Delta t)$ decays as the Fourier transform of single heralded photons [59]; meaning that by measuring the cross-correlation function we will directly measure the coherence time.

We measure the cross-correlation function of our photon-pairs by using the detection setup of Figure 3.10. We detect counts of the signal and idler photons using the APD1 and APD4 respectively. The data is acquired, organized and sent to the procesing

computer by a time tagger with ps resolution. Then with a program written in Phyton we analyze the data and set the coincidence time T_R mentioned in Figure 4.2. Usually we consider $T_R = 1.2$ ns with an integration time of $T = 17$ seconds. We achieve the maximum pair generation with perpendicular linear polarization of the $p1$ and $p2$ beams. The photon-pair coincidence rate between the signal and idler that we can achieve is about 10^4 counts per second. The non-normalized histogram of coherence detected and the experimental conditions are shown in Figure 4.3.

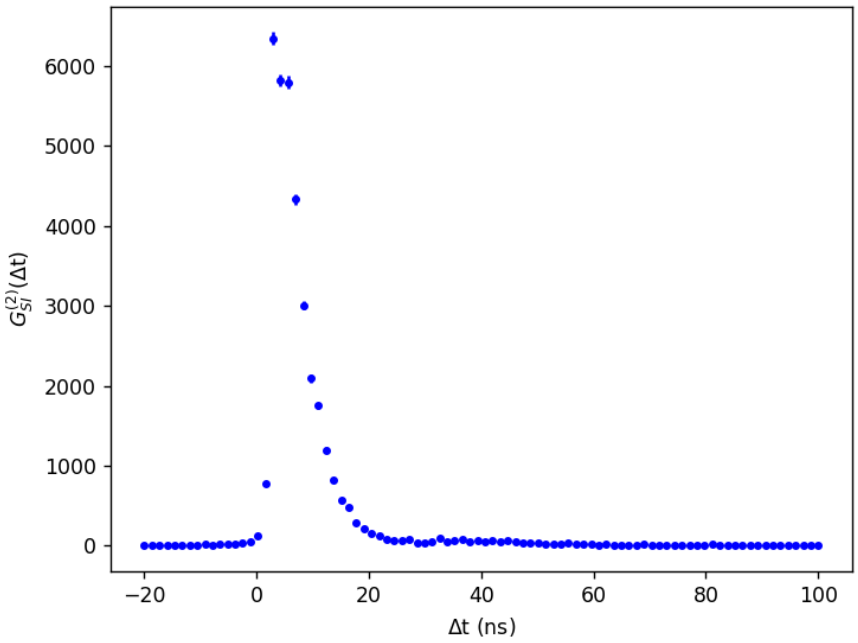

Figure 4.3: Histogram of cross-correlation function $G^{(2)}_{SI}(\Delta t)$ detected between the signal and idler photons. Δt is the delay between the signal of a photon arriving at the detector APD1 and the idler photon arriving at APD4. The experimental parameters were: $\Delta = -70$ MHz, $\delta = 6$ MHz, OD=20 and the power of the pump beams $p1 = 500$ μW, $p2 = 7$ mW.

Equation 4.21 from section 4.1 states that the experimental data follows a time dependece in the form

$$G_{ij}^{(2)}(\Delta t) = G_0 \exp\{(-(\Delta t)/\tau_0)\}\Theta(\Delta t) + \beta, \tag{4.26}$$

where G_0 is the maximum coincidence rate, τ_0 is the coherence time and β is the value of $G_{ij}^{(2)}(\Delta t)$ for $\Delta t >> 1$. As discussed in section 4.2.1, we need to normalize $G_{SI}^{(2)}(\Delta t)$ to obtain the second order degree of coherence

$$g_{ij}^{(2)}(\Delta t) = \frac{G_{ij}^{(2)}(\Delta t)}{acc} = \frac{\beta}{acc} + \frac{G_0}{acc} \exp\{(-(\Delta t)/\tau_0)\}\Theta(\Delta t). \tag{4.27}$$

The normalization term in equation 4.27 are the *accidental coincidences*. For a sufficiently large time, our fields are totally uncorrelated, so the expectation value in the denominator of eq (4.25) would be the product of two totally uncorrelated intensities of each field, hence $g_{ij}^{(2)}(\Delta t) = 1$ meaning $\beta/acc = 1$. These two intensities are

$$acc = R_i R_j T_R T, \tag{4.28}$$

where R_i and R_j are the total number of individual photon detections corresponding to the i and j channel, T_R the coincidence window time, T is the total integration time. Such intensities are the number of arriving photons, so we consider count rates R_i and R_j of each channel. Using this normalization, we can show that for $\tau >> 1$, it happens that $g_{ij}^{(2)}(\tau) = 1$.

Another way where we can find *acc* is directly from the non-normalized data presented in Figure 4.3. We can fit the equation (4.26) and determine the value *acc* because for a long time $\tau >> 1$ implies both $g_{ij}^{(2)}(\tau) = 1$ and the exponential term goes to zero.

Of course, both ways of finding the accidental coincidence value should be equivalent. We found $acc = 6.24 \pm 1.21$ by fitting equation 4.26 to the experimental data and $acc = 5.97 \pm 1.25$ calculated with equation (4.28). Those two values do agree within the error bars. Its worth noticing that the fit of the equation (4.26) depends largely on the

number of experimental points we consider. To get a better β value, we should include the most possible points from the plateau. For our case, that fitting interval was from -20 to 100 ns. The fact that the fitted *acc* is greater than the calculated parameter is expected because equation (4.28) does not consider suplementary photons generated by spontaneous emission.

As discussed in section 3.4.1, we can model the noise of our detectors like a random variable with the Gaussian distribution given by equation (3.8) where σ is the width of the Gaussian distribution. Thus the photon detection is the double stochastic process, which is described by the convolution between the distributions given by equations (4.27) and (3.8), i. e.,

$$g^{(2)}_{fit}(\Delta t) = (f * g^{(2)}_{ii})(\Delta t) = \frac{1}{2}\frac{G_0}{acc} e^{\left(\frac{\sigma^2 - 2\Delta t\tau_0}{2\tau_0^2}\right)} \left[\text{erf}\left(\frac{\Delta t\tau_0/\sigma - \sigma}{\sqrt{2}\tau_0}\right) + 1\right], \tag{4.29}$$

Equation (4.29) is the fitting function for the experimental data. It smoothens the Heaviside step function. Figure 4.4 plots the normalized experimental data fitted by a curve with the form of equation (4.30). Both follow the same qualitative behavior and agree qualitatively up to a certain extent. Using that fit, we can estimate that the maximum value for the cross-correlation function is $g^{(2)}_{SI}(\Delta t_{max}) = 1146 \pm 53$.

The parameter σ from the fit results of Figure 4.4 gave us a value of $\sigma = 0.61 \pm 0.04$ ns, which agree with the nominal time response of the detector according to the manufacturer $t_{res} = 400$ ps. The difference between values could be due to different time responses depending on the wavelength of incoming light.

We have some good agreement between the model of the second-order time-coherence and the experimental data because both follow the same general behavior: it has a fast rise after $\Delta t = 0$ and then a slow decay after reaching a maximum. We are detecting a large number of coincidences for positive values of Δt. This is modeled with the

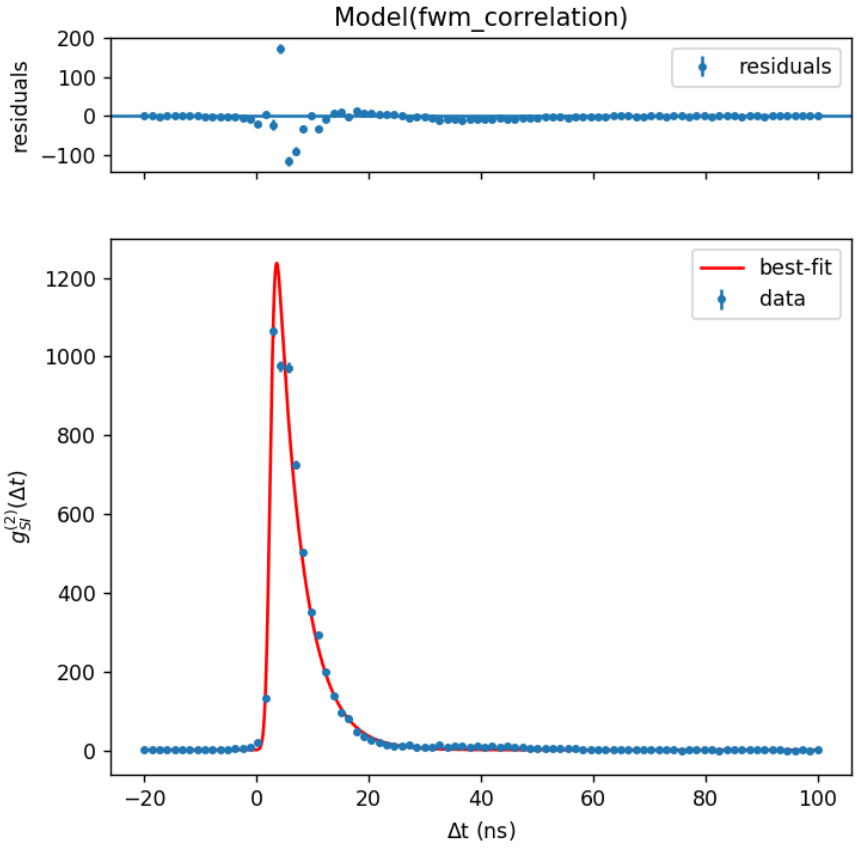

Figure 4.4: Normalized cross-correlation function $g^{(2)}_{SI}(\Delta t)$ of the signal and idler photons. The blue points are the experimental data and the red line is the fitted equation (4.29). From the fit: $g_0 = 424 \pm 12$, $\sigma = 0.61 \pm 0.04$ ns and $\tau_0 = 4.4 \pm 0.1$ ns. The residuals, which are the value of the model minus the experimental value, are plotted in the upper part of the figure. The experimental conditions were: $\Delta = -70$ MHz, $\delta = 6$ MHz, OD=20 and the power of the pump beams $p1 = 500$ μW, $p2 = 7$ mW.

Heaviside function in equation (4.26). Our atomic structure in diamond configuration assures us that after detecting a signal photon, we will detect an idler because the well time-ordered events described in Figure 4.21.This condition is called Heralded photons.

After reaching the maximum, the behavior of $g^{(2)}_{SI}(\Delta t)$ would give us information about the decay lifetime of the intermediate level $5P_{1/2}$. At $\Delta t = 0$ when we detect a signal photon, we know that the excited atom is in the level $5P_{1/2}$. We measure a decay

time of $\tau_0 = 4.4 \pm 0.1$ ns, which do not agree with the $5P_{1/2}$ level lifetime $\tau_{nat} = 27$ ns. We think this reduction of the decay time it is due to collective effects present in the atomic cloud that modify the output photons properties.

We can determine the idler photons bandwidth from the fit of the data in Figure 4.4, with the expression

$$\Gamma = \frac{1}{2\pi\tau_0}. \tag{4.30}$$

Substituting the measured value of τ_0 our heralded photons have bandwidth of $\Gamma = 36.2 \pm 0.8$ MHz. This factor is ten times smaller than the bandwidth measured in experiments of hot atoms [60]. The photon badwidth from this kind of sources can be reduced down to 20 MHz by modifying the experimental parameters [61]; by using a low-loss cavity [59] it can be reduced to 8 MHz.

With the bandwith of our idler photons and the coincidence rate r_c we can calculate the spectral brightness for our source of photon pairs. This parameter is defined as

$$\mathcal{B} = 2\pi\tau_0 r_c = \frac{r_c}{\Gamma}. \tag{4.31}$$

High value of $\mathcal{B}$ means either a high coincidence rate r_c and/or low bandwidth Γ, which is necessary for quantum information applications because with these two parameters we can promote the interaction between photons and atoms.

In our case the coincidence rate r_c is obtained from the unnormalized histogram $G^{(2)}_{SI}$ plotted in Figure 4.3. The maximum coincidence rate achieved was done at $\delta = 0.5$ MHz, giving a value of $r_c = (10.15 \pm 0.14) \times 10^3$ s^{-1}. So, the maximum brightness of our source is $\mathcal{B} = 280$ coincidences (s MHz)$^{-1}$. This value is consistent with observations in similar sources [62], and two orders of magnitude larger than the value reported for hot atomic ensembles [60].

4.2.3 Autocorrelation function

The autocorrelation function of the signal and idler photons can be found by first considering the power spectrum of a thermal source $S(\Delta\omega)$, which is a Lorentzian distribution [42] and then making a Fourier transform [63]

$$\begin{aligned} G^{(1)}(\Delta t) &= \int_{-\infty}^{\infty} d\tau e^{i\omega\Delta t} S(\Delta\omega), \\ &= \int_{-\infty}^{\infty} d\tau e^{i\omega\Delta t} \left(\frac{1}{\pi} \frac{\gamma/2}{(\omega-\omega_0)^2 + (\gamma/2)^2} \right), \\ &= \exp(-i\omega_0\Delta t - \gamma\Delta t), \end{aligned} \tag{4.32}$$

then using the property

$$G^{(1)}(-\Delta t) = G^{(1)}(\Delta t)^*, \tag{4.33}$$

together with

$$G^{(2)}(\Delta t) = 1 + G^{(1)}(\Delta t), \tag{4.34}$$

the expected distribution of the second-order autocorrelation function is

$$G^2_{ii}(\Delta t) = G_0 \exp(-|\Delta t|/\tau) + 1, \tag{4.35}$$

where G_0 is the maximum number of coincidences and τ the coherence time. In a similar manner as in the cross-correlation function calculation we can model the detector noise as a random variable following a Gaussian distribution with width σ. This is a double-stochastical process, described by a convolution between the distributions f and g

$$\begin{aligned} (f * g^{(2)}_{ii})(x) &= \int_{-\infty}^{\infty} f(t-x)g(t)dt = \int_{-\infty}^{\infty} G_0 \exp\{-|t|/\tau\} \frac{1}{\sigma 2\pi} \exp\left\{ -\frac{(t-x)^2}{2\sigma^2} \right\}, \\ &= \frac{G_0}{\sigma 2\pi} \left[\int_0^{\infty} \exp\left\{ -\frac{(t-x)^2}{2\sigma^2} - \frac{t}{\tau} \right\} + \int_{-\infty}^{0} \exp\left\{ -\frac{(t-x)^2}{2\sigma^2} + \frac{t}{\tau} \right\} \right]. \end{aligned} \tag{4.36}$$

In equation (4.36) the integral is split in two sections to separate the absolute value of equation (4.35). Manipulating both polynomial of the exponents

$$\begin{aligned} -\frac{(t-x)^2}{2\sigma^2} \mp \frac{t}{\tau} &= -\frac{\tau(t^2-2tx+x^2) \pm t2\sigma^2}{2\sigma^2\tau}, \\ &= -\frac{t^2-2t(x\mp\frac{\sigma^2}{\tau})+(x\mp\frac{\sigma^2}{\tau})^2-(x\mp\frac{\sigma^2}{\tau})^2+x^2\pm t2\sigma^2\tau^{-1}}{2\sigma^2}, \\ &= -\frac{(t-x\pm\frac{\sigma^2}{\tau})^2}{2\sigma^2}+\frac{1}{2\sigma^2}\left(2x\frac{\sigma^2}{\tau}\mp\frac{\sigma^2}{\tau^2}\right), \end{aligned} \tag{4.37}$$

the second term in the last line of equation (4.37) comes out of the integral because it does not depend on t. The integral of the first term can be solved with the change of variable $\chi = (t-x\pm\frac{\sigma^2}{\tau})/\sqrt{2}\sigma$ and using

$$\mathrm{erfc}(x) = \frac{2}{\sqrt{\pi}}\int_x^\infty e^{-\chi^2}d\chi. \tag{4.38}$$

Substituting equation (4.37) in both integrals, re-arraging terms, and returning to our variable $x \to \Delta t$ we have the fitting function

$$g^{(2)}_{fit}(\Delta t) = \frac{1}{2}G_0 e^{\left(\frac{\sigma^2-2\Delta t\tau_0}{2\tau_0^2}\right)}\left[\mathrm{erfc}\left(\frac{\sigma^2-\Delta t\tau_0}{\sqrt{2}\sigma\tau_0}\right)+e^{\frac{2\Delta t}{\tau_0}}\,\mathrm{erfc}\left(\frac{\sigma^2+\Delta t\tau_0}{\sqrt{2}\sigma\tau_0}\right)\right], \tag{4.39}$$

where G_0 and τ are the same constants of equation (4.35) and σ the width of the Gaussian.

To measure the autocorrelations, we use the experimental setup described in Figure 3.10. Each signal separately detected using a Hanbury-Brown and Twiss interferometer coupling the four beams into single-mode fibers, and then send them into the APDs 1 to 4. We balance the number of counts in each APD to divide the signal by 50/50. Measuring coincidences between APD1 and APD2 gives us the autocorrelation of the signal photons, and for the idler photons, APD3 and APD4.

We have approximately $\sim$ 100 coincidences per second. To collect data for the analysis, we integrate each signal for about $\sim$ 20 minutes. Figures 4.5 and 4.6 present the experimental data of each case and the corresponding fitted curves. We need to normalize the experimental data using the accidental coincidences *acc* defined in equation (4.28) to fit the normalized autocorrelation function $g^{(2)}_{ii}$ from equation (4.39).

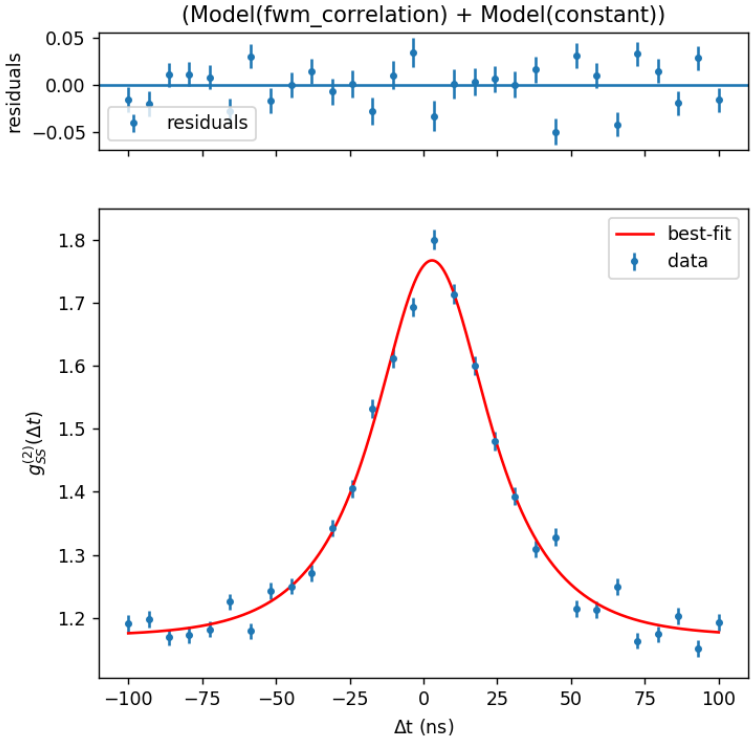

Figure 4.5: Normalized time autocorrelation function of the signal photons. The blue dots are the experimental data and the red line is the fit of equation (4.29). The parameters of the fit are: $g_0 = 0.22 \pm 0.03$, $\sigma = 9.77 \pm 2.12$ ns and $\tau_0 = 18.92 \pm 2.65$ ns. The residuals, which are the value of the model minus the experimental value, are plotted in the upper part of the figure. The experimental conditions were: $\Delta = -70$ MHz, $\delta = 6$ MHz, OD=20 and the power of the pump beams $p1 = 500$ μW, $p2 = 7$ mW.

Using those fits, we found that for $\Delta t = 0$, $g^{(2)}_{II}(0) = 1.59 \pm 0.02$ and $g^{(2)}_{SS}(0) = 1.84 \pm 0.02$. The corresponding value for the signal photons is larger than the idler

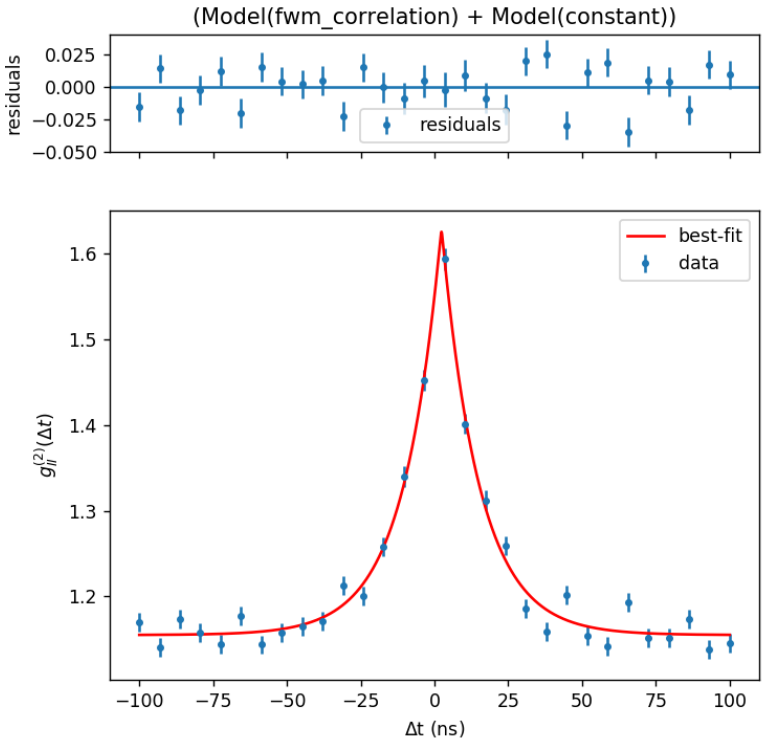

Figure 4.6: Normalized time autocorrelation function of the idler photons. The blue dots are the experimental data and the red line is the fit of eq. (4.29). The parameters of the fit are: $g_0 = 0.12 \pm 0.03$, $\sigma = 0.17 \pm 0.04$ ns and $\tau_0 = 12.80 \pm 0.90$ ns. The residuals, which are the value of the model minus the experimental value, are plotted in the upper part of the figure. The experimental conditions were: $\Delta = -70$ MHz, $\delta = 6$ MHz, OD=20 and the power of the pump beams $p1 = 500$ μW, $p2 = 7$ mW.

because the APDs have different quantum efficiency depending on the wavelengths. We can also see that the idler photon distribution is sharper than the signal. That means the Gaussian distribution of our detector noise is wider for the signal photon wavelength and less for the idler.

We identify the behavior of the autocorrelation of both photons as a thermal source. That is because during the experiment, we have around 5×10^7 atoms emitting, creating a bunching effect of the emmited photons.

We note that the distribution functions that we fit to the autocorrelation in equation (4.35) and the cross-correlation (4.26) are similar. The principal differences are an absolute value of the time difference Δt for the first case and the Heaviside step function in the second case. This difference is associated with the nature of the source: the cross-correlation measure heralded photon pairs while the autocorrelation data comes from a thermal source.

4.3 Cauchy-Schwarz inequality

The results from time-correlation measurements from section 4.2.2 and 4.2.3 contain all the information required to evaluate the Cauchy-Schwarz inequality, which evaluates the classicallty of the photon pair statistics.

Let $\mathbf{u}$ and $\mathbf{v}$ be two non-zero complex vector fields fulfilling the Maxwell equations, and define the complex number $\lambda \neq 0$

$$\lambda = \frac{\langle \mathbf{u}, \mathbf{v} \rangle}{||\mathbf{v}||^2}, \tag{4.40}$$

where $\langle \cdot, \cdot \rangle$ denotes the interior product. If we consider the term

$$\begin{aligned}
0 &\leq ||\mathbf{u} - \lambda \mathbf{v}||^2, \\
&= \langle \mathbf{u}, \mathbf{u} \rangle - \langle \lambda \mathbf{v}, \mathbf{u} \rangle - \langle \mathbf{u}, \lambda \mathbf{v} \rangle + \langle \lambda \mathbf{v}, \lambda \mathbf{v} \rangle, \\
&= \langle \mathbf{u}, \mathbf{u} \rangle - \lambda \langle \mathbf{v}, \mathbf{u} \rangle - \overline{\lambda} \langle \mathbf{u}, \mathbf{v} \rangle + \lambda \overline{\lambda} \langle \mathbf{v}, \mathbf{v} \rangle, \\
&= ||\mathbf{u}||^2 - \frac{\langle \mathbf{v}, \mathbf{u} \rangle}{||\mathbf{v}||^2} \langle \mathbf{u}, \mathbf{v} \rangle - \frac{\langle \mathbf{v}, \mathbf{u} \rangle}{||\mathbf{v}||^2} \langle \mathbf{u}, \mathbf{v} \rangle + \frac{\langle \mathbf{v}, \mathbf{u} \rangle}{||\mathbf{v}||^2} \frac{\langle \mathbf{u}, \mathbf{v} \rangle}{||\mathbf{v}||^2} ||\mathbf{v}||^2, \\
&= ||\mathbf{u}||^2 - \frac{|\langle \mathbf{u}, \mathbf{v} \rangle|^2}{||\mathbf{v}||^2}, \\
|\langle \mathbf{u}, \mathbf{v} \rangle|^2 &\leq ||\mathbf{u}||^2 ||\mathbf{v}||^2,
\end{aligned} \tag{4.41}$$

finally, we have

$$\frac{|\langle \mathbf{u}, \mathbf{v} \rangle|^2}{||\mathbf{u}||^2 ||\mathbf{v}||^2} \leq 1. \tag{4.42}$$

The Cauchy-Schawartz inequality (4.42) is valid for any pair of vectors describing a classical field. The coefficient R evaluated for classical fields must satisfy [58]:

$$R = \frac{[g^{(2)}_{SI}(\Delta t)]^2}{g^{(2)}_{S}(0)g^{(2)}_{I}(0)} \leq 1, \tag{4.43}$$

for every Δt. In our photon case, considering the results of the autocorrelation measurements $g^{(2)}_{SS}(0)$ and $g^{(2)}_{II}(0)$ from the signal and idler photons respectively, and the maximum of the cross-correlation $g^{(2)}_{SI}(\Delta t_{max}) = 1146 \pm 53$, we can evaluate the coefficient R

$$R = (4.49 \pm 0.43) \times 10^5 > 1. \tag{4.44}$$

This is a strong violation of the inequality by five order of magnitude. Larger than the $\sim 10^2$ reported by FWM in hot atoms or SPDC [60, 64]. We think that one of the reasons why we can reach such values is because the thermal noise suppression of our system, by trapping the atoms in a MOT. Comparable values are reported by similar experimental setups [65, 61].

This violation warranties that the statistics of the light produced in our experiment cannot be described using the classical theory of light.

Chapter 5

Numerical calculations

In this chapter, I describe numerical calculations solving the master equation (2.83) that describes our system. Based on a program written by our collaborator Dr. Ricardo Gutiérrez-Jáuregui, I wrote a version myself in Python, the language that we use in the lab. This was an opportunity to learn about numerical calculations of atomic systems and also to compare between the numerical solutions and the experimental data. We are interested in this formalism because we can directly include collective effects in the equations by modifying the decay constants.

5.1 Collective effects in photon pair generation: a first approach

In fluorescence experiments a dilute atomic gas is driven by a laser from the ground state to a excited state. In some cases one can consider that each atom is interacting independently with the radiation field. Here the emission is isotropic, obeying an exponential law with a characteristic time τ, which is the inverse of the decay rate Γ of the given atomic transition. If the atomic gas is more dense, we would have modifications in these photon properties. These modifications in general are called *collective effects* [66] and they are discussed in the next subsection.

To apply the theory of collective effects, our system should be in the high atomic density regime, defined by the condition [67]

$$\lambda < \langle r \rangle, \tag{5.1}$$

where λ is the wavelength of the interacting light and $\langle r \rangle$ is the average distance between atoms. To estimate the inter-particle distance a first approximation can be to consider all atoms inside a volume V equidistant between them, expressed as

$$\langle r \rangle \sim \frac{1}{n^{1/3}}, \tag{5.2}$$

where n is the particle density $n = N/V$ for a number N of particles inside a volume V. This is not our case because center of the atomic cloud is more dense than the outer part. However this approximation can give us an upper bound.

The laser interacting with the atomic cloud has a diameter of 1.1 mm, and the diameter of our MOT is about 5 mm. Lets recall the experiment setup with Figure (5.1)

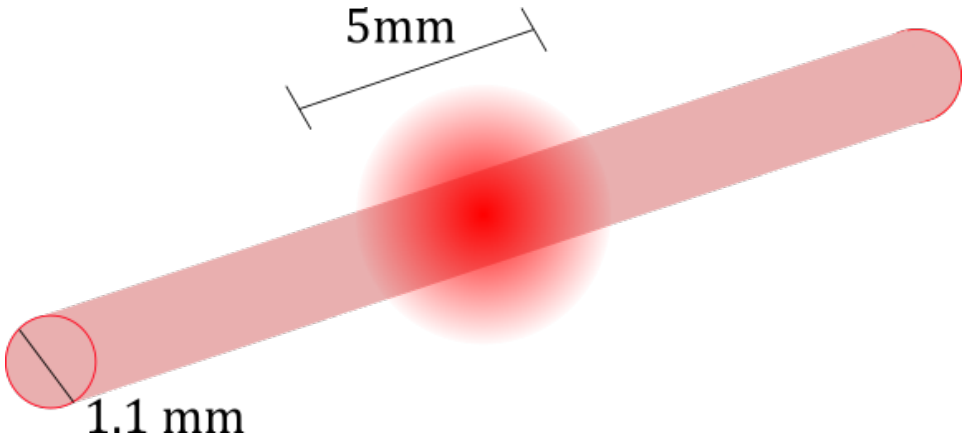

Figure 5.1: Schematics of the interaction area between the pumping laser and the atomic cloud.

According to the OD measurements in Chapter 3 we have an estimated number of 5×10^7 atoms interacting with the pumping beams. Supposing our atoms inside the

cloud are evenly distributed and calculating the density n, we can estimate the distance between atoms

$$\langle r \rangle = 4.5 \times 10^{-6} \text{ m}, \tag{5.3}$$

which is larger compared to the emission wavelength $\lambda = 0.8 \times 10^{-6}$ m, but comparable. So, we are not yet in the high atomic density regime. That means we cannot apply directly the theory of collective effects, but it can give us a first approximation for describing our experimental results. Equation (2.72) includes atom collective effects with one Lindblad term for each decay under consideration in the form of

$$\hat{L}_i(\rho) = \frac{\gamma^{eff}}{2}(2\sigma_{ji}\rho\sigma_{ij} - \sigma_{ij}\sigma_{ji}\rho - \rho\sigma_{ij}\sigma_{ji}). \tag{5.4}$$

In a first approach we consider that the collective effects can be modeled as an effective decay constant γ^{eff}, which will modify the decay time $\tau_0 = \frac{1}{\gamma^{eff}}$ of a particular transition, according to [66]

$$\tau_0 = \frac{\tau_{nat}}{1 + \mu \text{OD}}, \tag{5.5}$$

where τ_{nat} is the single-atom decay time, μ is a geometrical factor and OD is the optical density. The validity of this model for our system has yet to be shown. However the fact that we can modify the coherence time τ_0 by changing the number of atoms add control to our photon-pair source, and it will be important for the design of experiments in quantum information

5.2 Four-level solution

Using the method described in section 2.6.1 we solved numerically the master equation for the four-level atomic system mentioned in Figure 2.2. It solves equation (2.72) to obtain the time evolution of each component of the density matrix. Figure 5.2 shows

the experimental data for the cross-correlation in red dots. The blue curve depicts the fitted numerical calculation for the density matrix terms of equation (2.92). As we can see both curves have very similar behavior, with a quick rise at the beginning followed by a slow exponential-type decay. Although we indeed see a clear similarity between both behaviours, we can also see a difference in the slopes of the rising and decay parts, particularly for the points near $\Delta t = 0$ ns and $\Delta t = 15$ ns.

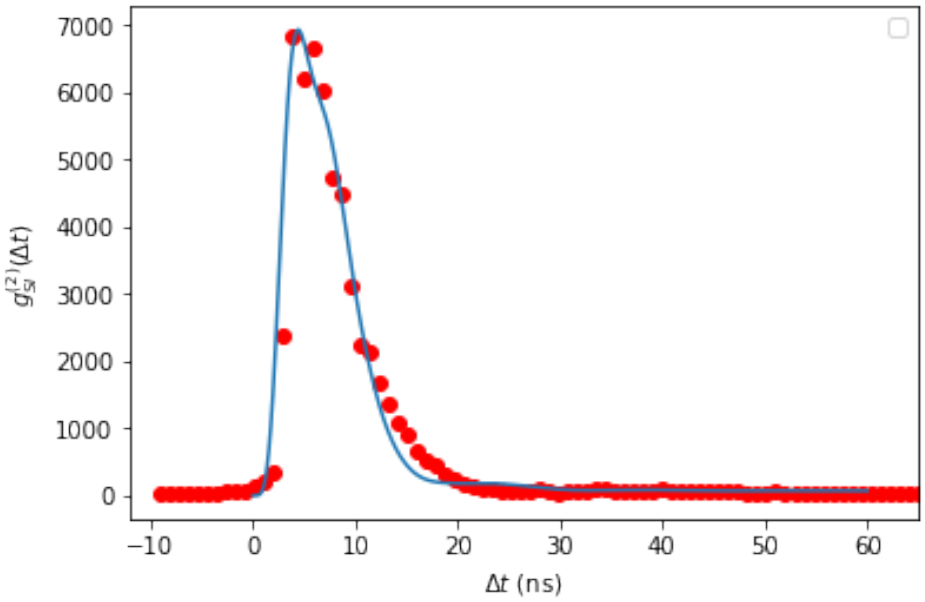

Figure 5.2: Cross-correlation function resulting from the four-level atomic calculation (blue continuous line) and experimental data (red dots). The experimental conditions in both systems were: $\Delta = -70$ MHz, $\delta = -2$ MHz, OD=20 and the power of the pump beams $p1 = 500$ μW, $p2 = 7$ mW.

There are some oscillations in the experimental data, as shown in Figure 5.3 that are not found in the numerical calculation. Those oscillations could be explained as interference between photons produced in different decay paths, called quantum beats [68]. This behavior can not be explained with this model because we are only considering

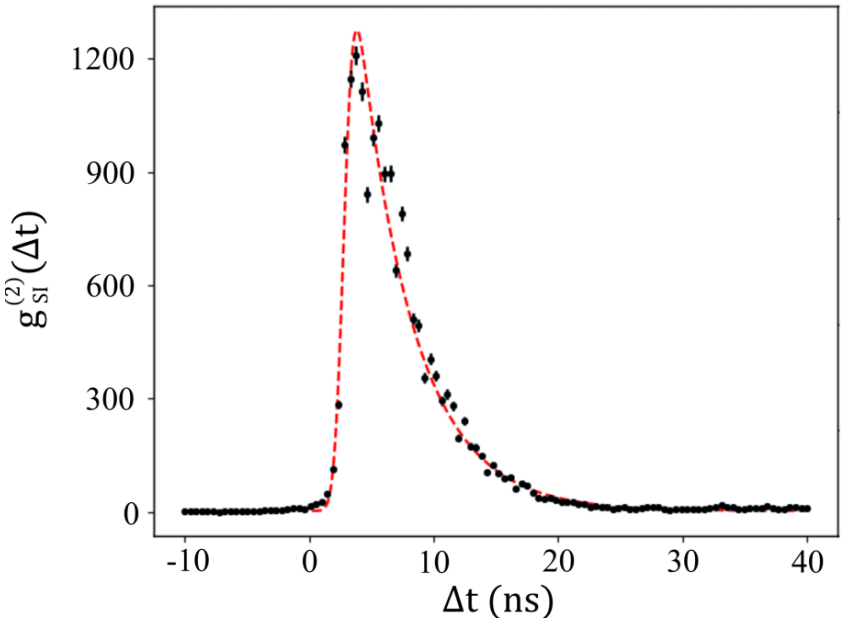

Figure 5.3: Normalized cross-correlation function $g^{(2)}_{SI}(\Delta t)$ of the signal and idler photons. The black points are the experimental data and the red line is the fitted equation (4.29). The experimental conditions were the same that in Figure 4.4 but this is a plot focusing on the time interval Δt from -10 to 40

a four-level atom. Adding more atomic levels could describe the data better, as we will see in the next section.

5.3 Nine-level solution

By using the program of Ricardo we solve the master equation for our experimental conditions with nine energy levels. Considering the relevant hyperfine structure in our FWM process, we label the following nine Rubidium levels as described in Figure 5.4.

We introduce our experimental conditions to the program through the Rabi frequencies exciting atomic levels, as shown in Figure 5.4, and the single-atom decay constants for Rubidium. With this numerical calculations we can take a qualitative insight to the possible collective efects, by changing the decay constants γ for example. To compare between simulation results and experimental data we use the term in equation (2.92).

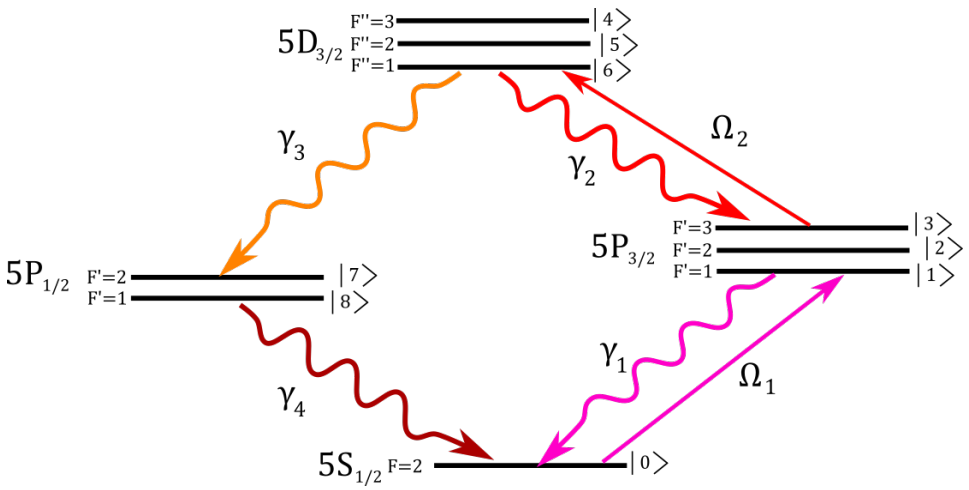

Figure 5.4: Atomic levels are considered for the master equation calculations. Here we show the labels of the levels as used in the program's code.

As a first approach, we consider all the decay constants modified by the same amount, which means

$$\gamma_i^{eff} = \alpha\gamma_i, \tag{5.6}$$

where α is a multiplicative constant. In that case, the cross-correlation function will have the behavior showed in Figure 5.5. As we can see, when we increase the value of α, the width of the distribution decreases. Qualitatively this corresponds to the behavior of equation (5.5). This behavior could give us an insight into how much the collective effects are present in our system through the value of α: We can measure the width of our experimental data and fit a value of α to the atomic calculation that results in a comparable width of both distributions. We can also manipulate the number of atoms experimentally to modify α so we can control the coherence time τ.

Another case to consider is that the effective decay constant γ^{eff} does not change by the same amount for each level. That represent a complex case, because in principle we do not know how the γ^{eff} change for each decay. To get some idea, we can analyze

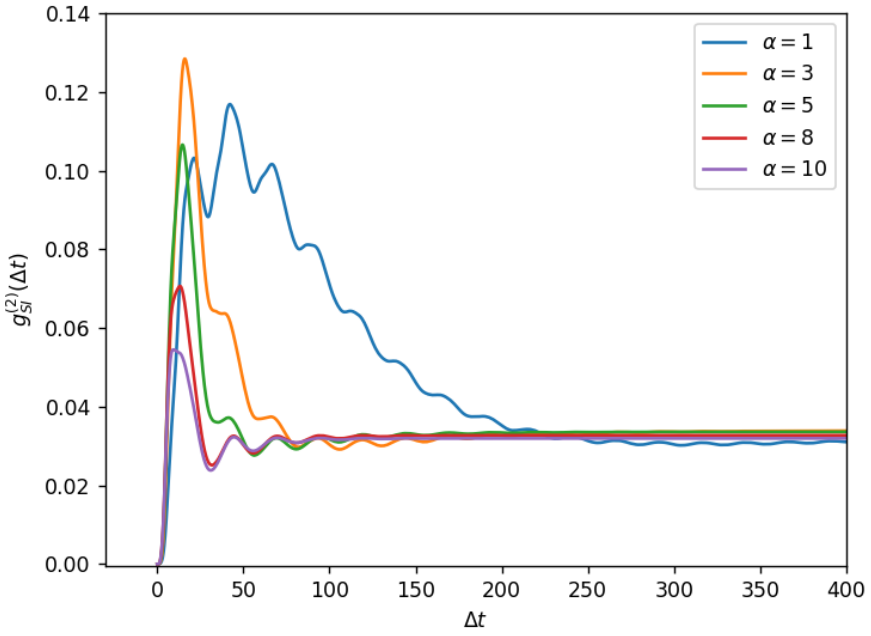

Figure 5.5: Cross-correlation function of the photon pairs with a variation of the multiplicative constant α of every γ_i decay term. The width of the distribution grows as α change. The experimental conditions considered were: $\Delta = -70$ MHz, $\delta = -2$ MHz, OD=20 and the power of the pump beams $p1 = 500$ μW, $p2 = 7$ mW.

the behavior when one of the four decays between fine levels is significantly bigger than the others. For simplicity, we consider the case where for a set of four effective constant, one of the four constants α_i, described in Figure 5.4, are set to a value ten times bigger than the others. In Figure 5.6 is the results of the numerical calculation for each case.

From these cases, we can conclude the following: The stationary value of $g^{(2)}_{SI}(\Delta t)$ for long times $\Delta t >> 1$ changes drastically for each case. When the γ_4^{eff} is the one with a multiplication factor of 10, we have the smallest value of the cross-correlation function for $\Delta t >> 1$. On the contrary, when γ_3^{eff} is 10 times greater, we have the biggest $g^{(2)}_{SI}(\Delta t)$ value in the limit. This information also could help us to shape the values of γ^{eff}, because we can extract from our experimental data the limit value of

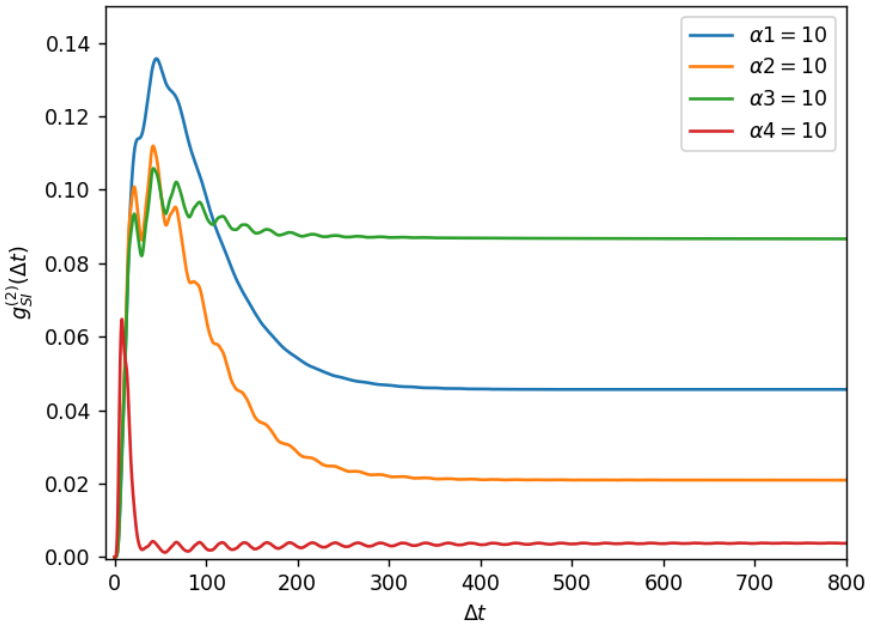

Figure 5.6: Cross-correlation function of the photon pairs with a variation of the multiplicative constant α of each γ_i decay term, i runs from 1 to 4 see Figure (5.4). The principal changes are the limiting value when $\Delta t >> 1$ and the maximum of the distribution. The experimental conditions considered were: $\Delta = -70$ MHz, $\delta = -2$ MHz, OD=20 and the power of the pump beams $p1 = 500$ μW, $p2 = 7$ mW.

the cross-correlation function, and consider it for adjusting the value of each γ^{eff} in the atomic calculation.

We can also get from our experimental data the ratio between the maximum of the $g^{(2)}_{SI}(\Delta t)$ distribution and the stationary value when $\Delta t >> 1$, and compare them to that same ratio from the experimental data to find the best suitable α_i values. In Figure 5.6 we can note the variations in that quotient for each case. In both Figure 5.5 and Figure 5.6 we can see quantum beats probably produced by interference between photons decaying from the level $|7\rangle$ and $|8\rangle$ into $|0\rangle$ (see Figure 5.4).

The qualitative analysis of Figure 5.5 and Figure 5.6 gave us an insight about the possible control of the temporal coherence that we can achieve in our system. We can

modulate its form, changing the amplitude and the coherence time τ by modifying the number of atoms. These effects can be used to enhance the control of our photon pair source.

Chapter 6

Conclusions and outlook

This thesis presented our first studies on the coherence time of photon pairs generated by FWM in a cold atomic Rubidium cloud. By solving the Schrödinger equation of consecutive cascade decays we obtain a model that reproduces the behavior of our experimental data. By fitting them we measure a coherence time of $\tau_0 = 4.4 \pm 0.1$ ns and a bandwidth of $\Gamma = 36.2 \pm 0.8$ MHz. Our system can achieve rates of about 10^4 photon pairs per second and brightness $\mathcal{B}$ of 280 coincidences (s MHz)$^{-1}$. Table 6.1 presents a comparation of parameters between our source and typical values of hot atoms and SPDC.

Source type	R	Γ (MHz)	$\mathcal{B}$ (MHz s)$^{-1}$
Cold atoms	4.49×10^5	36	280
Hot atoms	280	350	0.34
SPDC	100	THz	3940*

Table 6.1: Comparison of typical values of R coefficient, bandwidth Γ and spectral brightness $\mathcal{B}$ from different photon sources. Parameters taken from [60, 64].

The spectral brightness found in sources for SPDC is reported in the units (MHz s mW)$^{-1}$, and the spectral brightness from atomic sources in (MHz s)$^{-1}$. SPDC sources consider in their $\mathcal{B}$ definition how many photons are generated as a function of the

pumping beam, while the atomic sources do not. This means the comparison between them can not be done directly.

We measured the Cauchy coefficient R of the time coherence of our photon pairs. Using the measured values of cross-correlation and autocorrelation functions. We found a value of $R = (4.49 \pm 0.43) \times 10^5$, strongly violating the Cauchy-Schwarz inequality, which indicates that the coherence time of our photon pairs is non-classical.

6.1 Limit of studies and future work

While the model used here describes the general behavior of the experiment, the model do not describe the oscilation of our data. By considering only three levels in our model, it limits the description of phenomena like collective effects or quantum beats. In Chapter 5 we apply the Jaynes-Cummings formalism and solve numerically the master equations of the system for four and nine energy levels respectively, and also compare them with the experimental data. With four levels, we obtain similar results compared with the solution of the Schrödinger equation. When we solve the system for nine levels, there are oscillations in the cross-correlation function due to interference between levels, being quantum beats. We can observe those same oscilations in the experimental data.

6.2 Polarization entanglement

One of the variables that we can easily modify and detect in our experiment is the polarization of the produced photons. It has been shown that the photon pairs generated present quantum correlations in polarization and can form Bell states [68, 60].

We have measured polarization correlations in our system, finding that the polarization of the generated photons depends on the pumping polarization. Using the atomic degrees of freedom in our system and the experimental parameters can give our system

versatility to produce and control these entangled states. The next step in our experiment would be to measure and control the polarization entanglement of the emitted photons. By controlling the polarization states of the generated photons we can use them to imprint and manage information with them, useful for security protocols like quantum key distribution [69].

6.3 Application: Quantum memory

In a future experiment we plan to use our generated photon pairs to write on a quantum memory. The work done in this thesis shows that we can produce photon pairs resonant to the $5S_{1/2} \rightarrow 5P_{1/2}$ transition, with a bandwidth of $\Gamma = 36.2$ MHz. In principle, they can transfer information imprinted in them by interacting with atoms. Future work is needed in order to demostrate if this interaction is possible, and to identify the important parameters to promote it. Recently it has been shown that a quantum memory protocol is possible by atoms interacting with few photons [70]. The modulation of the time coherence and the polarization entanglement would be useful to control the properties of the photons that we will send to the memory, to store the polarization state.

Appendices

Appendix A

Program for a four-level atom

In this appendix there is a brief description of a program that I wrote in Python. It is based on a program written by Dr. Ricardo Gutiérrez-Jáuregui in FORTRAN to solve the dynamics of the master equation for an arbitrary number of atomic states. This program was mainly intended to connect our experimental results with a first simple atomic description. We find similarities and discrepancies with a system with more levels.

This program solves the system of differential equations that we obtain from the master equation for a four-level atom interacting with two near-resonance lasers and including a decay for each level via Lindblad terms. Recalling the master equation (2.83), we calculate the matrix elements

$$\begin{aligned}\langle i|\dot{\rho}|j\rangle = &\frac{1}{i\hbar}\langle i|(H\rho-\rho H)|j\rangle + \frac{\gamma_1}{2}\langle i|(2\sigma_{10}\rho\sigma_{01}-\sigma_{10}\sigma_{01}\rho+\rho\sigma_{10}\sigma_{01})|j\rangle \\ &+ \frac{\gamma_2}{2}\langle i|(2\sigma_{21}\rho\sigma_{12}-\sigma_{21}\sigma_{12}\rho+\rho\sigma_{21}\sigma_{12})|j\rangle + \frac{\gamma_3}{2}\langle i|(2\sigma_{32}\rho\sigma_{23}-\sigma_{32}\sigma_{23}\rho+\rho\sigma_{32}\sigma_{23})|j\rangle \\ &+ \frac{\gamma_4}{2}\langle i|(2\sigma_{03}\rho\sigma_{30}-\sigma_{03}\sigma_{30}\rho+\rho\sigma_{03}\sigma_{30})|j\rangle,\end{aligned} \tag{A.1}$$

where γ_i is the decay rate of each level i, the atomic operators $\sigma_{ij} = |j\rangle\langle i|$ and H the four level Hamiltonian in equation (2.82). We can reduce this equation using the properties

$$\sigma_{ij}|k\rangle = |j\rangle\langle i|k\rangle = |j\rangle\delta_{ik}. \tag{A.2}$$

If we do that and apply the hermiticity of the density matrix as discussed in section 2.6 , we end with a system of 16 linear differential equations. We can express this system of differential equations in a matrix form $\dot{\mathbf{V}} = \mathcal{M}\mathbf{V}$ where $\mathbf{V}$ is a vector with 16 entries, each one of them being an element of the density matrix and $\mathcal{M}$ is a 16×16 matrix of coefficients. In the program we re-arrange the terms of the density matrix so we only have a real system of equations with this nomenclature for the density matrix elements

$$\mathbf{V} = \begin{bmatrix} \rho_{00} \\ \rho_{11} \\ \rho_{22} \\ \rho_{33} \\ Re(\rho_{01}) \\ Im(\rho_{01}) \\ Re(\rho_{02}) \\ Im(\rho_{02}) \\ Re(\rho_{03}) \\ Im(\rho_{03}) \\ Re(\rho_{12}) \\ Im(\rho_{12}) \\ Re(\rho_{13}) \\ Im(\rho_{13}) \\ Re(\rho_{23}) \\ Im(\rho_{23}) \end{bmatrix}. \tag{A.3}$$

The code used for the atomic calculations uses a function named *odeint* from the package *scipy* that solves the system of differential equations using a library in the FORTRAN language called *Isoda*.

The basic structure of the program is the following:

- We first declare a series of vectors with 4 components and 4×4 matrices. Here we will introduce the experimental parameters and the initial conditions.
- Define the 16 component vector containing the element of the density matrix, the interval of time, and the 16×16 $\mathcal{M}$ matrix, that contains the master equation (A.1).

- Build the function *deriv(,)* which would take as inputs a matrix, a number, and a vector, and it performs a matrix multiplication between the vector and the matrix
- We use the package odeint to solve the differential equation corresponding to the vector and matrix system. It returns a series of strings with the time evolution of each component of the vector.

```
import numpy as np
from scipy.integrate import odeint
%matplotlib inline


#Declare arrays of each variable
R=np.ones((4,4))
I=np.ones((4,4))
R1=np.zeros((4,4))
I1=np.zeros((4,4))
dR=np.zeros((4,4))
dI=np.zeros((4,4))
dR1=np.zeros((4,4))
dI1=np.zeros((4,4))
g=np.zeros((4,4))
gdth=np.zeros(4)
rab=np.zeros((4,4))
detdt=np.zeros(4)
```

```
d=np.zeros(4)


#    Detuning from level 1
detdt[1] = -60
d[1]= -60
#    Detuning from level 2
detdt[2] = -7
d[2]= -7
#     Decay rate from 5P 3/2 to 5S 1/2
g[0,1] = 26.285


#     Decay rate from 5D 3/2 to 5P 3/2
g[1,2] = 0.3664


#     Decay rate from 5D 3/2 to 5P 1/2
g[2,3] = 2.436
```

```
#     Decay rate from 5P 1/2 to 5S 1/2
g[0,3] = 17.96


#    Helping variables for the calculus
gdth[0] =0
gdth[1] = 0.5*(g[0,1])
gdth[2] = 0.5*(g[1,2]+g[2,3])
gdth[3] = 0.5*(g[0,3])


# Defining Rabi frequencies
rab=np.zeros((4,4))
rab[0,1]=15.1368/2
rab[1,2]=16.9108/2


# Nomenclature for Vector V=(R00,R11,R22,R33,R01,I01,R02,I02,R03,I03,R12,I12,R13,I13,R23,I23)
# Matrix A of the system
A=np.array([[0,g[0,1],0,g[0,3],0,-rab[0,1],0,0,0,0,0,0,0,0,0,0],
```

```
[0,-g[0,1],g[1,2],0,0,rab[0,1],0,0,0,0,0,-rab[1,2]/2,0,0,0,0],
[0,0,-g[1,2]-g[2,3],0,0,0,0,0,0,0,0,rab[1,2]/2,0,0,0,0],
[0,0,g[2,3],-g[0,3],0,0,0,0,0,0,0,0,0,0,0,0],
[0,0,0,0,-gdth[0]-gdth[1],d[0]-d[1],0,-rab[1,2]/2,0,0,0,0,0,0,0,0],
[rab[0,1]/2,-rab[0,1]/2,0,0,-d[0]+d[1],-gdth[0]-gdth[1],rab[1,2]/2,0,0,0,0,0,0,0,0,0],
[0,0,0,0,0,-rab[1,2]/2,-gdth[0]-gdth[2],d[0]-d[2],0,0,0,rab[0,1]/2,0,0,0,0],
[0,0,0,0,rab[1,2]/2,0,-d[0]+d[2],-gdth[0]-gdth[2],0,0,-rab[0,1]/2,0,0,0,0,0],
[0,0,0,0,0,0,0,-rab[2,3]/2,-gdth[0]-gdth[3],d[0]-d[3],0,0,0,rab[0,1]/2,0,0],
[0,0,0,0,0,0,0,0,-d[0]+d[3],-gdth[0]-gdth[3],0,0,-rab[0,1]/2,0,0,0],
[0,0,0,0,0,0,0,0,0,0,-gdth[1]-gdth[2],rab[0,1]/2+d[1]-d[2],0,0,0,0],
[0,rab[1,2]/2,-rab[1,2]/2,0,0,0,0,0,0,0,-rab[0,1]/2-d[1]+d[2],-gdth[1]-gdth[2],0,0,0,0],
[0,0,0,0,0,0,0,0,0,rab[0,3],0,0,-gdth[1]-gdth[3],d[1]-d[3],0,rab[1,2]/2],
[0,0,0,0,0,0,0,0,-rab[0,3],0,0,0,-d[1]+d[3],-gdth[1]-gdth[3],-rab[1,2]/2,0],
[0,0,0,0,0,0,0,0,0,0,0,0,rab[1,2]/2,-gdth[2]-gdth[3],d[2]-d[3]],
[0,0,0,0,0,0,0,0,0,0,0,0,-rab[1,2]/2,0,-d[2]+d[3],-gdth[2]-gdth[3]]])
```

```
# Initial conditions
```

```
b_0=np.array([0,0,0,1,0,0,0,0,0,0,0,0,0,0,0,0])



# Define the function deriv(), which will make a product between the matrix and the vector and help to solve the system
def deriv(A, t, Ab):
    return np.dot(Ab, A)
time = np.linspace(0, 1, 900000)



# Solve differential equation system using package scipy.integrate
Sol = odeint(deriv,b_0, time, args=(A,))
Sol
```

Appendix B

Calculation of Rabi frequencies

In this appendix I present the results of the calculation of the geometrical part $\mathcal{G}$ of equation (2.97), which is the transition Rabi frequency between two levels

$$\mathcal{G} = (-1)^{F-m} \sum_{q=-1}^{1} \begin{pmatrix} F & 1 & F' \\ -m & q & m' \end{pmatrix} (-1)^{J+I+F'+1} \sqrt{(2F+1)(2F'+1)} \begin{Bmatrix} J & I & F \\ F' & 1 & J' \end{Bmatrix}, \tag{B.1}$$

where F, m denote the quantum numbers of the initial state and F', m' the numbers of the final state, and the 3-j *Wigner symbols* are denoted by circular parentheses and 6-j *symbols* denoted by curly brackets.

The $p1$ beam that connects the transition $5S_{1/2}, F = 2 \rightarrow 5P_{3/2}, F'$ have horizontal polarization in the $\hat{x}$ direction, according to our quantization axis selection of Figure 2.3. This means $q = -1, +1$ for the spherical basis that translate into $\sigma^+ + \sigma^-$ polarization. The geometrical factors $\mathcal{G}$ are

$F = 2 \rightarrow F' = 3$					
σ^+			σ^-		
m	m'	$\mathcal{G}$	m	m'	$\mathcal{G}$
-2	-1	$1/(2\sqrt{15})$	-2	-3	$1/2$
-1	0	$1/(2\sqrt{5})$	-1	-2	$1/\sqrt{6}$
0	1	$1/\sqrt{10}$	0	-1	$1/\sqrt{10}$
1	2	$1/\sqrt{6}$	1	0	$1/(2\sqrt{5})$
2	3	$1/2$	2	1	$1/(2\sqrt{10})$

$F = 2 \rightarrow F' = 2$					
σ^+			σ^-		
m	m'	$\mathcal{G}$	m	m'	$\mathcal{G}$
-2	-1	$1/(2\sqrt{6})$	-1	-2	$-1/(2\sqrt{6})$
-1	0	$1/4$	0	-1	$-1/4$
0	1	$1/4$	1	0	$-1/4$
1	2	$1/(2\sqrt{6})$	2	1	$1/(2\sqrt{10})$

$F = 2 \rightarrow F' = 1$					
σ^+			σ^-		
m	m'	$\mathcal{G}$	m	m'	$\mathcal{G}$
-2	-1	$1/(2\sqrt{10})$	0	-1	$1/(4\sqrt{15})$
-1	0	$1/(4\sqrt{5})$	1	0	$1/(4\sqrt{5})$
0	1	$1/(4\sqrt{15})$	2	1	$1/(2\sqrt{10})$

The $p2$ beam that connects the transition $5P_{3/2}F' = 3 \rightarrow 5D_{3/2}, F''$ have horizontal polarization in the $\hat{y}$ direction, according to our quantization axis selection of Figure 2.3. This means $q = 0$ for the spherical basis that translate into π polarization. The geometrical factors $\mathcal{G}$ are

$F' = 3 \rightarrow F'' = 3$		
π		
m	m'	$\mathcal{G}$
-3	-3	$-(\sqrt{\frac{3}{5}}/2)$
-2	-2	$-1/(\sqrt{15})$
1	1	$-1/(2\sqrt{15})$
0	0	0
1	1	$1/(2\sqrt{15})$
2	2	$1/(\sqrt{15})$
3	3	$(\sqrt{\frac{3}{5}}/2)$

$F' = 3 \rightarrow F'' = 2$		
π		
m	m'	$\mathcal{G}$
-2	-2	$1/(2\sqrt{15})$
1	1	$\sqrt{\frac{2}{3}}/5$
0	0	$\sqrt{3}/10$
1	1	$\sqrt{\frac{2}{3}}/5$
2	2	$1/(2\sqrt{15})$

$F' = 2 \rightarrow F'' = 3$		
π		
m	m'	$\mathcal{G}$
-2	-2	$1/(2\sqrt{15})$
1	1	$\sqrt{\frac{2}{3}}/5$
0	0	$\sqrt{3}/10$
1	1	$\sqrt{\frac{2}{3}}/5$
2	2	$1/(2\sqrt{15})$

$F' = 2 \rightarrow F'' = 2$		
π		
m	m'	$\mathcal{G}$
-2	-2	$-1/(\sqrt{15})$
1	1	$-1/(2\sqrt{15})$
0	0	0
1	1	$1/(2\sqrt{15})$
2	2	$1/(\sqrt{15})$

$F' = 2 \rightarrow F'' = 1$		
π		
m	m'	$\mathcal{G}$
1	1	$1/5$
0	0	$2/(5\sqrt{3})$
1	1	$1/5$

$F' = 1 \rightarrow F'' = 2$		
π		
m	m'	$\mathcal{G}$
1	1	$1/5$
0	0	$2/(5\sqrt{3})$
1	1	$1/(2\sqrt{15})$

$F' = 1 \rightarrow F'' = 1$		
π		
m	m'	$\mathcal{G}$
1	1	$-1/(2\sqrt{15})$
0	0	0
1	1	$1/(2\sqrt{15})$

Bibliography

[1] M. Planck. "On the law of distribution of energy in the normal spectrum." In: *Annalen Der Physik* 4.553 (1901), p. 1.

[2] A. Einstein. "On a heuristic point of view concerning the production and transformation of light." In: *Annalen Der Physik* (1905), pp. 1–18.

[3] P. A. M. Dirac. "The fundamental equations of quantum mechanics." In: *Proceedings of the Royal Society of London. Series A, Containing Papers of a Mathematical and Physical Character* 109.752 (1925), pp. 642–653.

[4] R. H. Brown and R. Twiss. "A test of a new type of stellar interferometer on Sirius." In: *Nature* 178.4541 (1956), pp. 1046–1048.

[5] T. Maiman. "Stimulated Optical Radiation in Ruby." In: *Nature* 187 (1960), pp. 493–494.

[6] L. Mandel and E. Wolf. "Coherence properties of optical fields." In: *Reviews of Modern Physics* 37.2 (1965), p. 231.

[7] L. Mandel and E. Wolf. *Optical coherence and quantum optics*. Cambridge university press, 1995.

[8] R. J. Glauber. "The quantum theory of optical coherence." In: *Physical Review* 130.6 (1963), p. 2529.

[9] D. C. Burnham and D. L. Weinberg. "Observation of simultaneity in parametric production of optical photon pairs." In: *Physical Review Letters* 25.2 (1970), p. 84.

[10] J. F. Clauser. "Experimental distinction between the quantum and classical field-theoretic predictions for the photoelectric effect." In: *Physical Review D* 9.4 (1974), p. 853.

[11] S. J. Freedman and J. F. Clauser. "Experimental test of local hidden-variable theories." In: *Physical Review Letters* 28.14 (1972), p. 938.

[12] N. R. Council et al. *Controlling the quantum world: the science of atoms, molecules, and photons*. Vol. 2. National Academies Press, 2007.

[13] L. M. Duan et al. "Long-distance quantum communication with atomic ensembles and linear optics." In: *Nature* 414.6862 (2001), pp. 413–418.

[14] T. Chaneliere et al. "Quantum telecommunication based on atomic cascade transitions." In: *Physical Review Letters* 96.9 (2006), p. 093604.

[15] K. Niizeki et al. "Ultrabright narrow-band telecom two-photon source for long-distance quantum communication." In: *Applied Physics Express* 11.4 (2018), p. 042801.

[16] N. Horiuchi. "Scalable sources." In: *Nature Photonics* 14.9 (2020), pp. 530–530.

[17] J. Yin et al. "Satellite-based entanglement distribution over 1200 kilometers." In: *Science* 356.6343 (2017), pp. 1140–1144.

[18] V. Scarani et al. "The security of practical quantum key distribution." In: *Reviews of Modern Physics* 81.3 (2009), p. 1301.

[19] *Quantum-Safe Security Solutions*. May 2021. URL: https://www.idquantique.com/quantum-safe-security/overview/.

[20] A. Kozhekin, K. Mølmer, and E. Polzik. "Quantum memory for light." In: *Physical Review A* 62.3 (2000), p. 033809.

[21] W. J. Munro et al. "Inside quantum repeaters." In: *IEEE Journal of Selected Topics in Quantum Electronics* 21.3 (2015), pp. 78–90.

[22] D.-S. Ding et al. "Single-photon-level quantum image memory based on cold atomic ensembles." In: *Nature Communications* 4.1 (2013), pp. 1–7.

[23] M. Parniak et al. "Wavevector multiplexed atomic quantum memory via spatially-resolved single-photon detection." In: *Nature Communications* 8.1 (2017), pp. 1–9.

[24] H. P. Specht et al. "A single-atom quantum memory." In: *Nature* 473.7346 (2011), pp. 190–193.

[25] S. Chen et al. "Deterministic and storable single-photon source based on a quantum memory." In: *Physical Review Letters* 97.17 (2006), p. 173004.

[26] D. Du et al. "An elementary 158 km long quantum network connecting room temperature quantum memories." In: *arXiv preprint arXiv:2101.12742* (2021).

[27] H. J. Metcalf and P. Van der Straten. "Laser cooling and trapping of neutral atoms." In: *The Optics Encyclopedia: Basic Foundations and Practical Applications* (2007).

[28] A. L. Migdall et al. "First observation of magnetically trapped neutral atoms." In: *Physical Review Letters* 54.24 (1985), p. 2596.

[29] K. B. Davis et al. "Bose-Einstein condensation in a gas of sodium atoms." In: *Physical Review Letters* 75.22 (1995), p. 3969.

[30] M. A. Seidler et al. "Upper bound on the duration of quantum jumps." In: *CLEO: Science and Innovations*. Optical Society of America. 2019, JTu2A–24.

[31] V. Leong et al. "Time-resolved scattering of a single photon by a single atom." In: *Nature Communications* 7.1 (2016), pp. 1–5.

[32] J. Huang et al. "Quantum metrology with cold atoms." In: *Annual Review of Cold Atoms and Molecules* (2014), pp. 365–415.

[33] A. D. Ludlow et al. "Optical atomic clocks." In: *Reviews of Modern Physics* 87.2 (2015), p. 637.

[34] Y. W. Cho et al. "Highly efficient optical quantum memory with long coherence time in cold atoms." In: *Optica* 3.1 (2016), pp. 100–107.

[35] C. Monroe. "Quantum information processing with atoms and photons." In: *Nature* 416.6877 (2002), pp. 238–246.

[36] J. D. Jackson. "Classical electrodynamics." In: American Association of Physics Teachers, 1999, pp. 237, 259.

[37] J. J. Sakurai. "Quantum mechanics." In: Addison-Wesley, Massachusetts, 1994, p. 66.

[38] R. W. Boyd. "Nonlinear optics." In: Academic Press, 2020, p. 314.

[39] M. O. Scully and M. S. Zubairy. "Quantum optics." In: American Association of Physics Teachers, 1999, pp. 194, 616–618.

[40] W. P. Schleich. *Quantum optics in phase space*. John Wiley & Sons, 2011.

[41] H. J. Carmichael. "Statistical methods in quantum optics 1: master equations and Fokker-Planck equations." In: vol. 1. Springer Science & Business Media, 1999, pp. 6–8, 32–34.

[42] H. J. Carmichael. *Statistical methods in quantum optics 1: master equations and Fokker-Planck equations*. Springer Science & Business Media. Pages 45-48, 2013.

[43] D. Steck. *Rubidium 87 D Line Data*. Dec. 2020. URL: http://steck.us/alkalidataS.

[44] L. A. Mendoza López. *Espectroscopía de dos fotones para experimentos con mezclado de cuatro ondas*. Tesis de Licenciatura, Universidad Nacional Autónoma de México, 2017.

[45] C. Hawthorn, K. Weber, and R. Scholten. "Littrow configuration tunable external cavity diode laser with fixed direction output beam." In: *Review of Scientific Instruments* 72.12 (2001), pp. 4477–4479.

[46] A. Martínez Vallejo. *Construcción de una trampa magneto-óptica*. Tesis de Maestría, Universidad Nacional Autónoma de México, 2019.

[47] T. T. Grove et al. "Two-photon two-color diode laser spectroscopy of the Rb 5D5/2 state." In: *Physica Scripta* 52.3 (1995), p. 271.

[48] P. K. Mandal et al. "Blue fluorescence as a frequency offset reference in the rubidium 5S-5P-5D transition." In: *Applied Optics* 57.13 (2018), pp. 3612–3617.

[49] *Optical Glassware: Precision Glassblowing*. Apr. 2020. URL: https://www.precisi%20onglassblowing.com/optical-glassware/.

[50] M. Gross and S. Haroche. "Superradiance: An essay on the theory of collective spontaneous emission." In: *Physics Reports* 93.5 (1982), pp. 301–396.

[51] H. J. Metcalf and P. van der Straten. "Laser cooling and trapping of atoms." In: *Journal of the Optics Society of America B* 20.5 (2003), pp. 887–908.

[52] J. Armstrong. "OFDM for optical communications." In: *Journal of Lightwave Technology* 27.3 (2009), pp. 189–204.

[53] J. W. Goodman. *Statistical optics*. John Wiley & Sons, 2015.

[54] D. Martínez Cara. *Estudios de correlaciones y polarización en pares de fotones generados por mezclado de cuatro ondas en una trampa magneto-óptica.* Tesis de Licenciatura, Universidad Nacional Autónoma de México, 2021.

[55] N. Arias-Téllez et al. "An experimental setup to generate narrowband bi-photons via four wave mixingin cold atoms." In: *To be submitted* (2021).

[56] J. W. Dettman. *Applied complex variables*. Courier Corporation, 1965.

[57] C. A. Kocher. "Time correlations in the detection of successively emitted photons." In: *Annals of Physics* 65.1 (1971), pp. 1–18.

[58] Z. J. Ou. "Quantum optics for experimentalists." In: World Scientific Publishing Company, 2017, pp. 14, 197.

[59] M. A. Seidler et al. "Spectral Compression of Narrowband Single Photons with a Resonant Cavity." In: *Physical Review Letters* 125.18 (Oct. 2020), p. 183603.

[60] R. Willis et al. "Four-wave mixing in the diamond configuration in an atomic vapor." In: *Physical Review A* 79.3 (2009), p. 033814.

[61] B. Srivathsan et al. "Narrow band source of transform-limited photon pairs via four-wave mixing in a cold atomic ensemble." In: *Physical Review Letters* 111.12 (2013), p. 123602.

[62] A. Cerè et al. "Characterization of a photon-pair source based on a cold atomic ensemble using a cascade-level scheme." In: *Physical Review A* 98.2 (2018), p. 023835.

[63] R. Loudon. *The quantum theory of light*. OUP Oxford, 2000.

[64] A. Seri et al. "Quantum correlations between single telecom photons and a multimode on-demand solid-state quantum memory." In: *Physical Review X* 7.2 (2017), p. 021028.

[65] S. Du et al. "Subnatural linewidth biphotons with controllable temporal length." In: *Physical Review Letters* 100.18 (2008), p. 183603.

[66] C. Stroud Jr et al. "Superradiant effects in systems of two-level atoms." In: *Physical Review A* 5.3 (1972), p. 1094.

[67] W. Guerin, M. Rouabah, and R. Kaiser. "Light interacting with atomic ensembles: collective, cooperative and mesoscopic effects." In: *Journal of Modern Optics* 64.9 (2017), pp. 895–907.

[68] G. K. Gulati et al. "Polarization entanglement and quantum beats of photon pairs from four-wave mixing in a cold 87Rb ensemble." In: *New Journal of Physics* 17.9 (2015), p. 093034.

[69] R. Renner. "Security of quantum key distribution." In: *International Journal of Quantum Information* 6.01 (2008), pp. 1–127.

[70] C. Kupchak et al. "Room-temperature single-photon level memory for polarization states." In: *Scientific reports* 5.1 (2015), pp. 1–5.